UNIVERSITÀ DEGLI STUDI DI PALERMO

Corso di Dottorato in Ingegneria dell'Innovazione Tecnologica
Dipartimento di Ingegneria
ING-IND/15 – Disegno e metodi dell'ingegneria industriale

TOPOLOGY OPTIMIZATION DESIGN OF MONOLITHIC 3D PRINTED COMPLIANT MECHANISMS FOR BIO-INSPIRED ACTUATION SYSTEMS OF FWMAVs

IL DOTTORE
ING. GIOVANNI CAROLLO

IL COORDINATORE
CHIA.MO PROF. SALVATORE GAGLIO

IL TUTOR
CHIA.MO PROF. TOMMASO INGRASSIA

CICLO XXXV

Table of contents

Table of contents 2

Acknowledgements 4

Abstract 5

List of abbreviations 6

1. Introduction 7

1.1 Design using flexibility: issues and opportunities 7

1.2 Dissertation arrangement 20

2. Compliant Mechanisms 26

2.1 Challenges and advantages in CMs' design 26

2.2 Modeling of CMs in intermediate and large displacement range 31

3. Topology Optimization 44

3.1 Comparison of the main structural optimization methods 45

3.2 CMs' design through TO: main methods overview 48

4. Bio-Inspired Designs: Flapping Wing Micro Air Vehicles 59

5. Additive Manufacturing Technologies: Fused Deposition Modeling 71

6. Design of CMs with low frequency of deformation: wiper case study 77

6.1 Reengineering approach and definition of a novel flexible monolithic wiper 78

6.2 FEA results and performance comparison 84

7. Actuation system for FWMAVs: bio-inspired CMs 93

8. Topology Optimization on CMs: Solid elements FEA modeling 114

9. Topology Optimization on CMs: Shell elements FEA modeling and multistep optimization 137

10. Conclusions: Outlook and future developments 161

References 165

Acknowledgements

This dissertation is the outcome of my research carried out during the PhD studies at the Department of Engineering of University of Palermo. I would like to express my most sincere and heartfelt thanks to my advisor, Prof. Tommaso Ingrassia, together with Prof. Antonio Pantano, who always supported me throughout my doctoral studies with their precious mentoring and guidance. Thanks to all my colleagues and co-workers from the Engineering Department that accompanied me in this journey. Finally, many thanks to my family and friends who always supported and encouraged me.

Abstract

The main focus of the present dissertation is to explore the capability of a combined design approach that exploits at once the advantages of FEM analysis, Compliant Mechanisms, Topology Optimization and 3D Printing Technologies. Nowadays the continuous pursuit of lighter and simpler products is widespread in any industrial company aiming to maintain competitivity. At the same time, while part-count reduction of an item is a desirable target, also the complexity of designs tends to be ever-growing.

In this context, the implementation of a design process suitable to combine different engineering tools becomes significant, in order to fulfill all the required product specifications and to develop innovative products with increased performances. In particular, this research aims to highlight the critical issues and the potentialities of implementing topology optimized Compliant Mechanisms in the development of monolithic 3D printable structures for the actuation of bio-inspired Flapping Wing Micro Air Vehicles (FWMAVs). Seeking a modern approach to design, the aforementioned engineering design tools were integrated with the effectiveness of solutions offered by nature, exploiting the idea of re-engineering the natural flexibility inherent in biological structures.

The opportunity of tailoring the design was taken into account too, in order to provide a potential source of inspiration for a different range of applications.

List of abbreviations

AM	Additive Manufacturing
CM	Compliant Mechanism
DOC	Degree of Constraint
DOF	Degree of Freedom
FDM	Fused Deposition Modeling
FEA	Finite Element Analysis
FEM	Finite Element Method
FWMAV	Flapping Wing Micro Air Vehicle
MAV	Micro Air Vehicle
TO	Topology Optimization
UAV	Unmanned Aerial Vehicles

1. Introduction

1.1 Design using flexibility: issues and opportunities

Commonly, when one think about a mechanical structure aimed to the transmission of motion and forces, it’s likely to imagine a multicomponent mechanism, usually made up of a series of rigid elements linked to each other through several kinds of joints. But if we examine the structures of living organisms, we can observe that they are made up by a perfect conjunction of flexibility and stiffness, since each part of the structure has a specialised mechanical behaviour according to his functionality. Indeed, in order to perform tasks required for their survival, the tendency of exploiting the flexibility of their structure rather than the stiffness is common both among plants and animals. For instance it could be mentioned the ability of organs such as the lungs and the heart that are able to handle pressure gradients by repeatedly expanding and contracting, the function carried out by cartilages, tendons and muscles enabling the movement of the limbs, or the adaptability of the octopuses' tentacles allowing the objects to be manipulated or the movement to be made.

In the last years, inspired by such considerations, many researchers focused their attention on the development of innovative designs which have resulted in bio-inspired structures. Within this context, Compliant Mechanisms represent a remarkable design tool since they are able to integrate stiff and flexible areas as part of the same monolithic structure.

Actually, unlike rigid-body mechanisms, which functioning is accomplished by rigid elements assembled in multi-component structures, the main distinguishing feature of CMs is their ability to trasmit motion and forces basically through their elastic deformation, without the involvement of internal joints. Among the major advantages concerning the use of Compliant Mechanisms, which will be properly detailed following, it's worth to mention their capability of reducing the part-count of a product and lightening the system where they are applied. One of the most relevant application areas of CMs concerns the micromanipulation for precise positioning of micrometer-size objects [1].

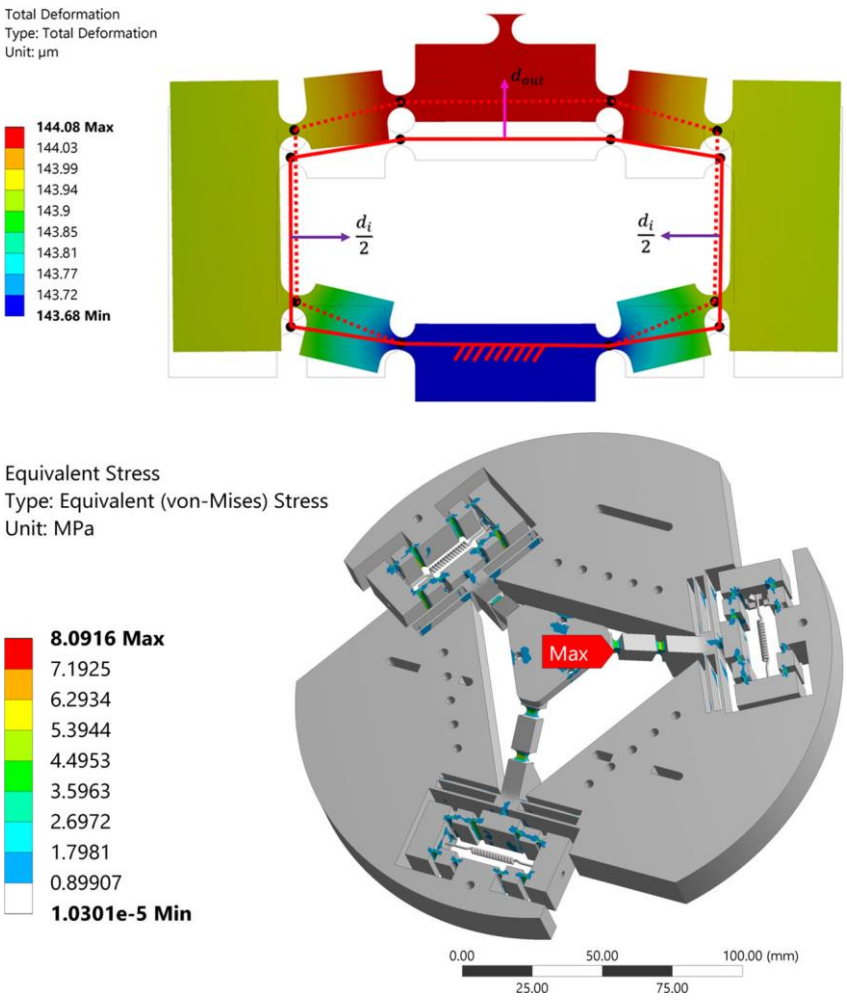

Figure 1.1. Compliant micromanipulator for precise positioning applications, FEA deformation and stress

This kind of applications particularly benefits from the capability of Compliant Mechanisms to be realized in a single-component structure, which represents a critical aspect considering otherwise the potential complexities of manufacturing and maintenance of an equivalent assembled rigid-body mechanism realized in micrometer size. Moreover, the aptitude of CMs to be miniaturized and especially the possibility to accurately predict their mechanical behaviour in terms of stresses and displacements makes them particularly useful to be exploited in automated highly-precision environments as microassembly manufacturing processes or biomedical field, as in the case of Compliant Nano-Pliers for nanoscale biomedical use [2].

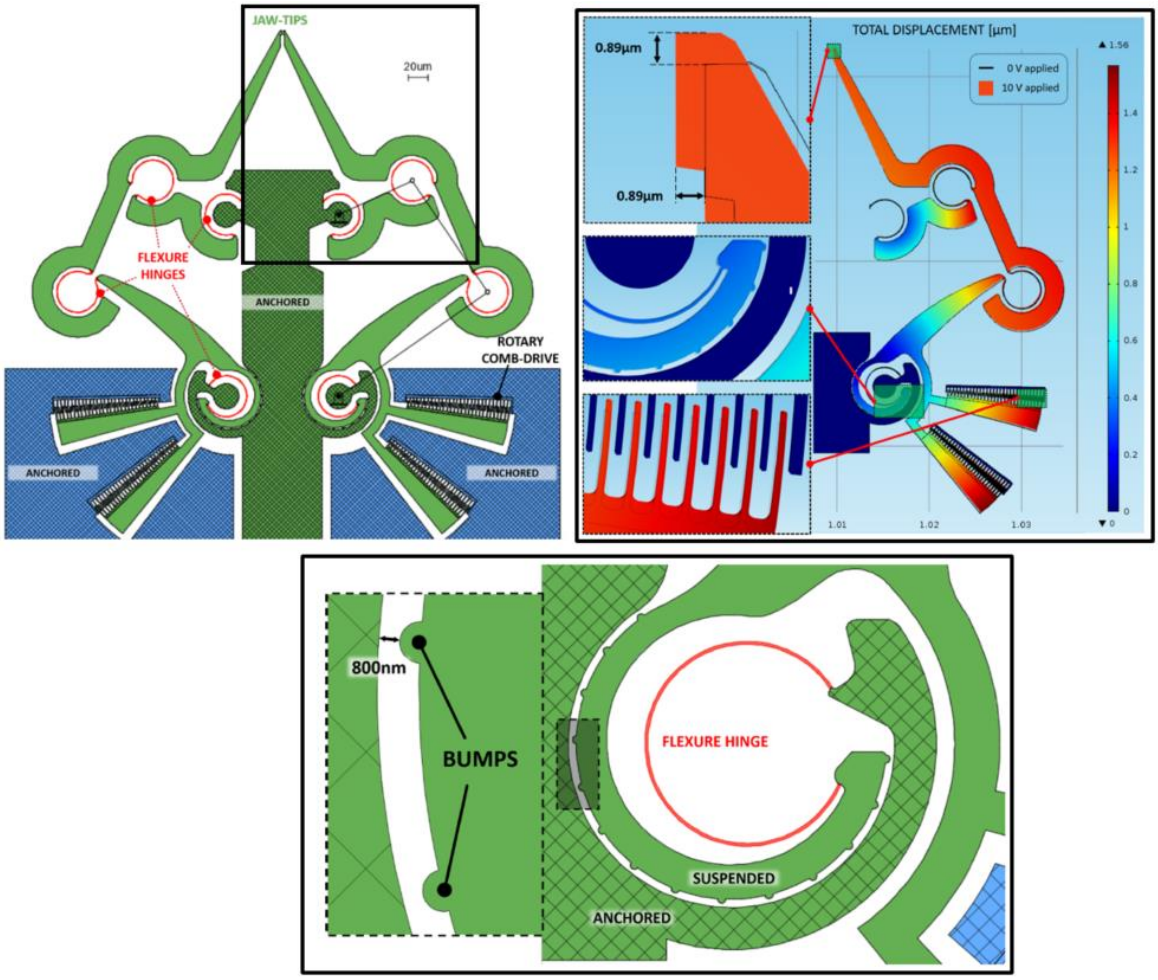

Figure 1.2 Compliant Nano-Pliers at nanoscale, detail of the nano-scale flexure hinge and FEA deformation

The great relevance that Compliant Mechanisms recently gained is also due to their manufacturability using biocompatible materials that furthermore could be produced through innovative Additive Manufacturing processes, such as Laser Powder Bed Fusion (PBF). Specifically, some researchers overcome the threeshold of the low elasticity offered by some of the main additive manufacturable metal alloys by using a bulk metallic glass forming alloy (i.e. $Zr_{59.3}Cu_{28.8}Al_{10.4}Nb_{1.5}$) which in addition could provide the designers the flexibility advantages peculiar of Compliant Mechanisms. Indeed, as can be seen from the diagram in Figure 1.3, the elasticity of a material dramatically affects the maximum rotational motion of CM, since high strength material properties are in most cases unsuitable to achieve great displacements, as required in this research [3].

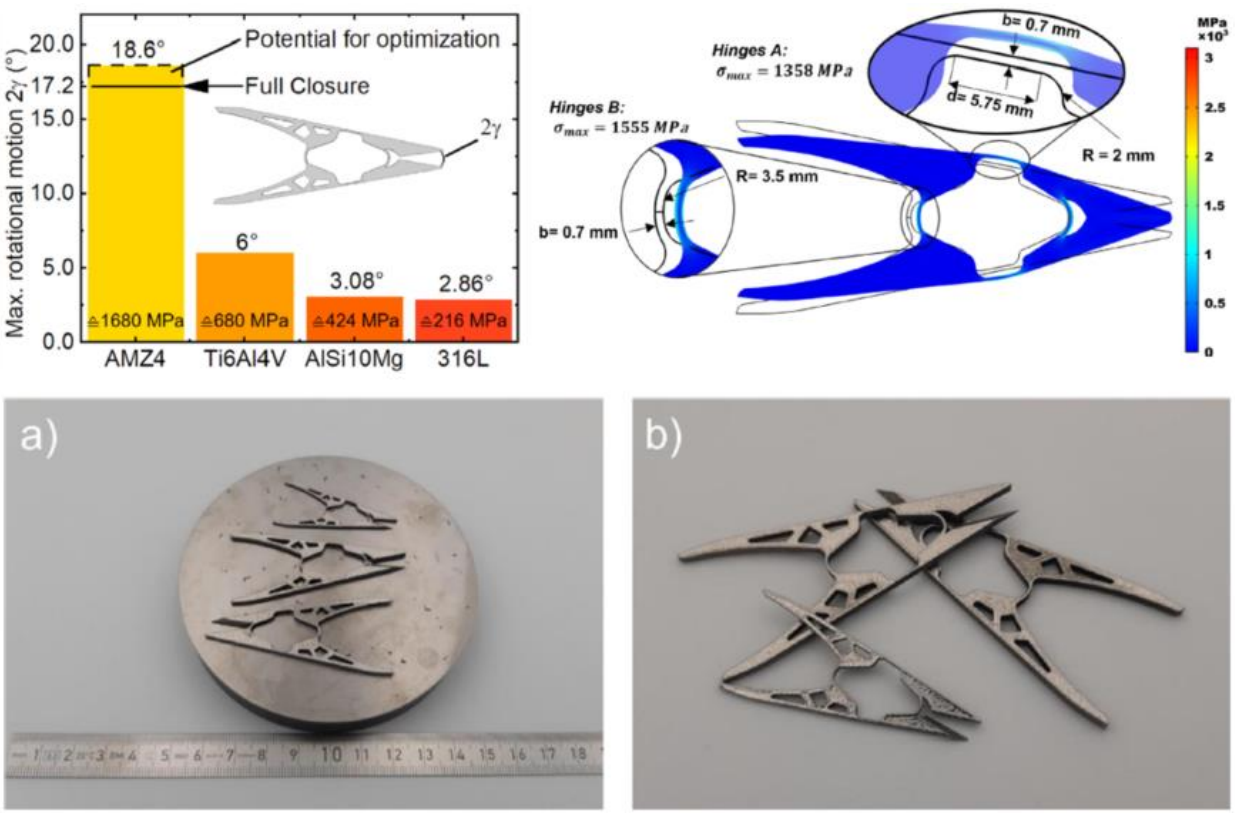

Figure 1.3 Additive Manufacturing of Compliant Mechanism using a bulk metallic glass forming alloy via Laser Powder Bed Fusion, detail of comparison with metallic alloys and relative maximum rotational motion

Concerning this last aspect, as will be adequately elaborated following, when designing a CM whose functioning necessarily implies the actuation of great displacements, a crucial issue is finding a compromise between flexibility and strength. This certainly represents a restrictive issue to be careful of, considering that each application requires a specific operational range of stresses and displacements but at the same time only a restricted geometrical design space is allowed. Regardless of this, the availability of tools such as FEA simplifies the designer's research of an appropriate tradeoff in such a way as to explore different layouts with several material disposition [4],[5]. Despite it's a widespread sentiment that the usage of metallic materials for reaching large displacements it's unrealistic, the FEA capability to try out a variety of configurations made also possible the application of a titanium alloy (Ti_6Al_4V) to realize a large-displacement monolithic compliant rotational hinge to be used in space application [6],[7].

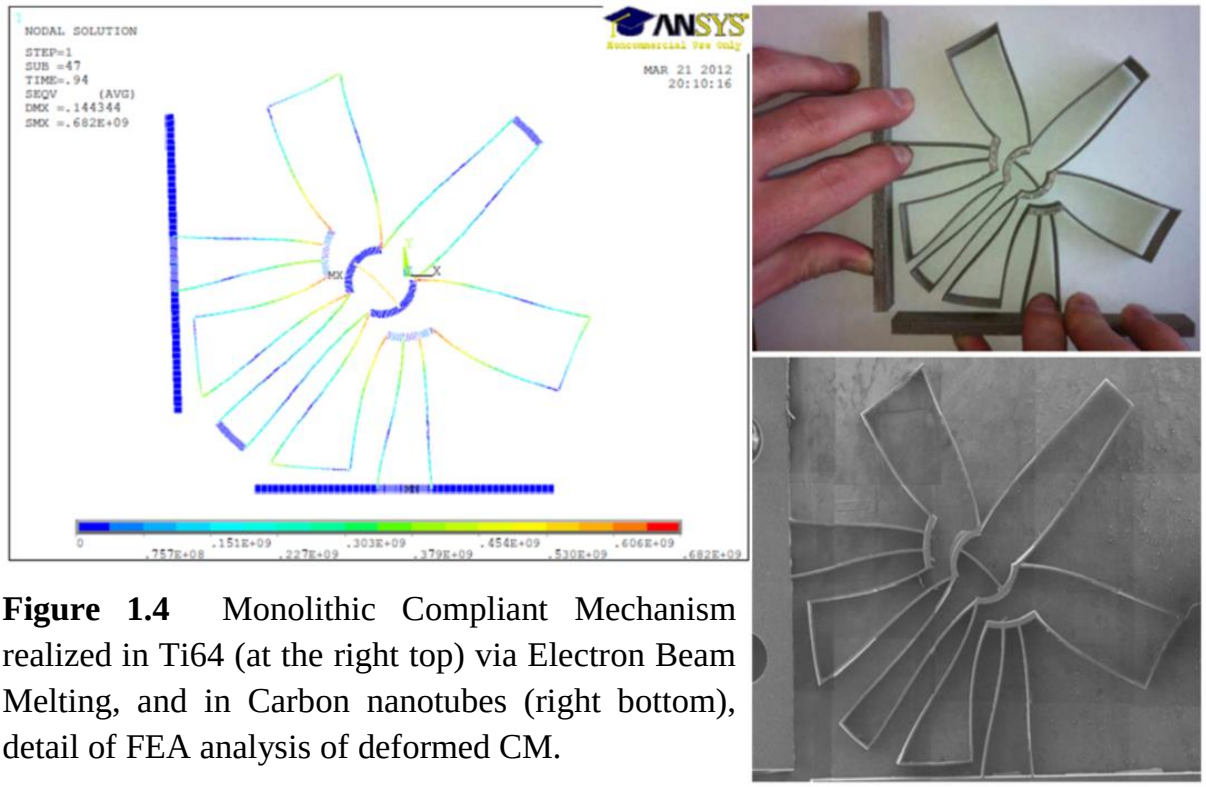

Figure 1.4 Monolithic Compliant Mechanism realized in Ti64 (at the right top) via Electron Beam Melting, and in Carbon nanotubes (right bottom), detail of FEA analysis of deformed CM.

This significant research shows how a smart exploitation of the design space, supported by FEA instruments and Additive Manufacturing, could allow also challenging designs. A remarkable technical detail is related to the absence of needs of lubrication, that enables the space application of such mechanisms and materials. Moreover, another distinctive characteristic of CMs is their manufacturing scalability, as shown above in Figure 1.4 where an identical mechanism with the same layout is made in a reduced aspect ratio using Carbon nanotubes (magnified through a scanning electron micrograph). The analysis of living organisms represents another profitable instrument for the conception of innovative CMs. Indeed, the need to get the best material arrangement within a limited design space could be combined with the examination of structures of living beings as a wide source of inspiration. In such direction, the development of in-depth studies on biomechanical principles have allowed, among other applications, the implementation of the the so-called Fin Ray Effect, learned from observing the structure of fishes' fins. This principle has resulted in several bio-inspired variants of soft fingers made up by a novel Compliant Mechanism's design [8], [9]. The possibility of grasping both fragile or pressure sensitive components and heavy duty items makes them a very adaptable tool especially in a dynamic production context, such as the one of industry 4.0, given the broad range of products to be handled [10], [11].

This kind of application in industrial environments benefits in addition from the CM's compactness, the reduced part-count, the lower maintenance and no-lubrication. On the other hand, FEM analysis of highly flexible

mechanisms becomes more complex and requires the implementation of non-linear analysis mainly for these reasons:

- Some areas of mechanism experience large deformations;
- Contact conditions on boudary surface change during operation;
- High overall displacements could lead to buckling situations or undesired vibrations with high operating frequencies;

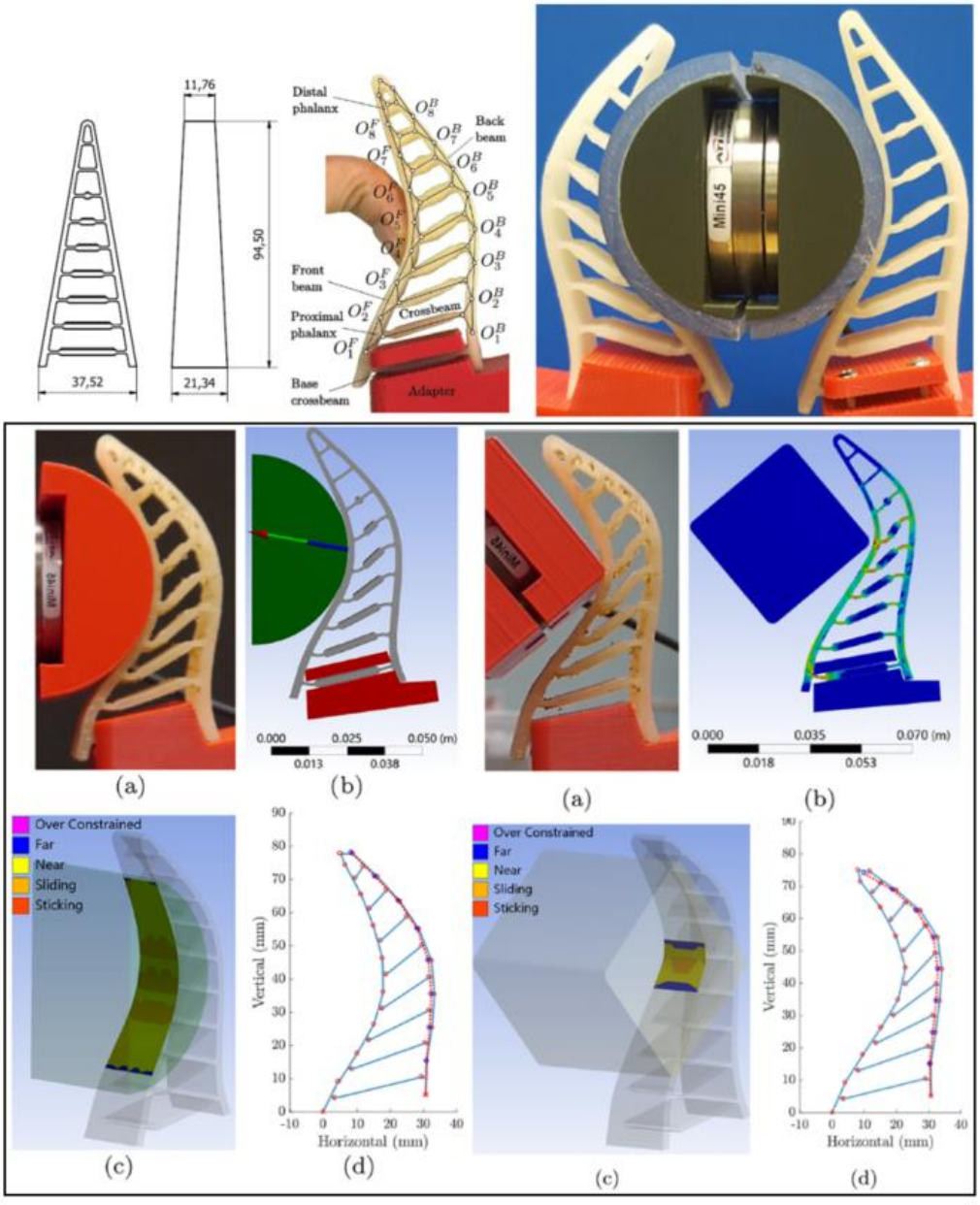

Figure 1.5 Soft compliant fingers bio-inspired from Fin-ray effect, details of prototype and contact conditions with different surfaces

In other instances, the observation of living beings as ladybird beetle has lead to the development of a deployable compliant origami mechanism, inspired by the geometry of the vein of the wing of this insect [12].

A particularly appreciable feature of this category of flexible mechanisms resides the opportunity to concentrate in a compact space a deployable structure. In this case, the elastic deformation energy stored in the not already deployed mechanism, is used as a reversible source of elastic energy during the opening phase. Such a deployment characteristic turns out to be even more valuable in applications where both the weight and the overall dimensions needs to be minimized, such as space industry, employing it as solar array support [13].

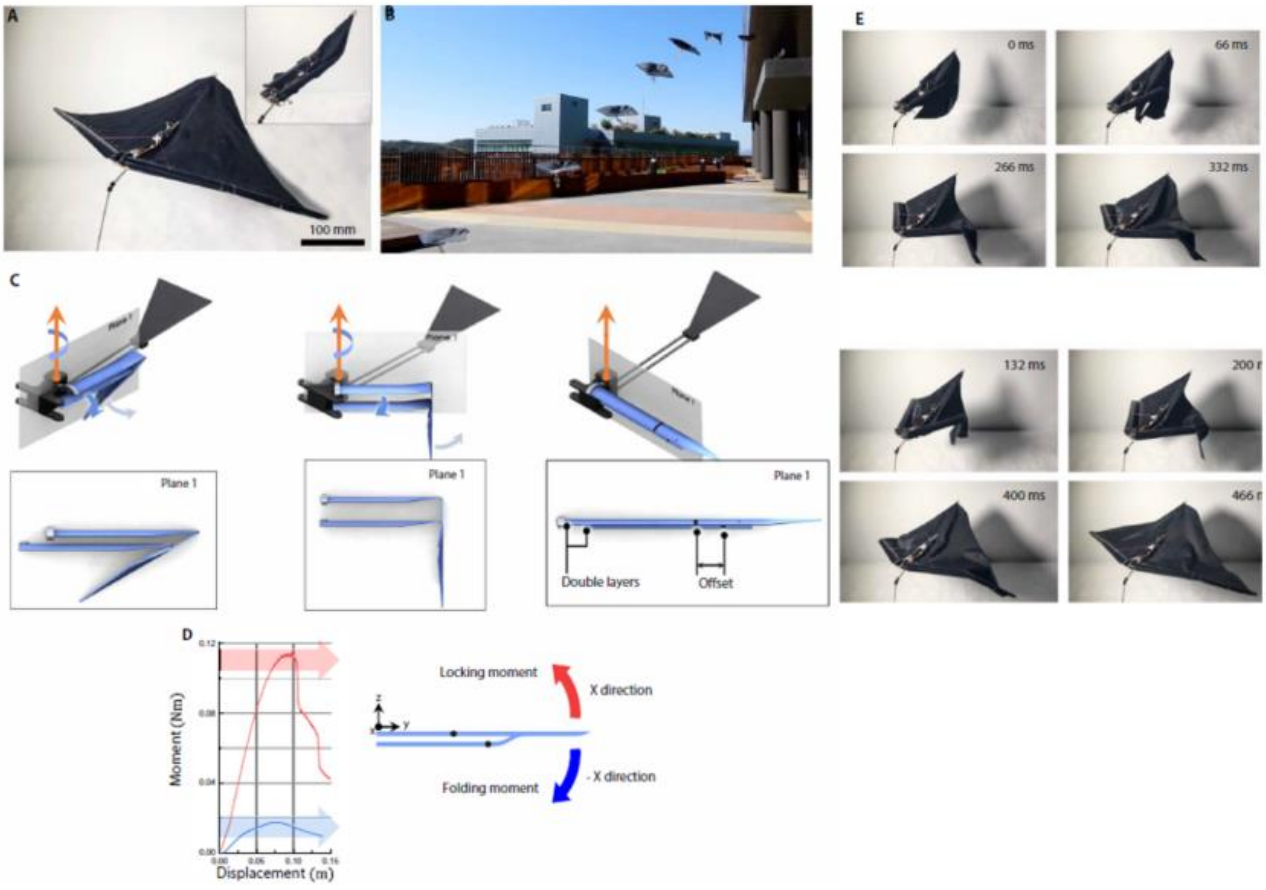

Figure 1.6 Origami self-deployable compliant structure, bio-inspired by ladybird beetle wing veins; details of progressive shapes during opening.

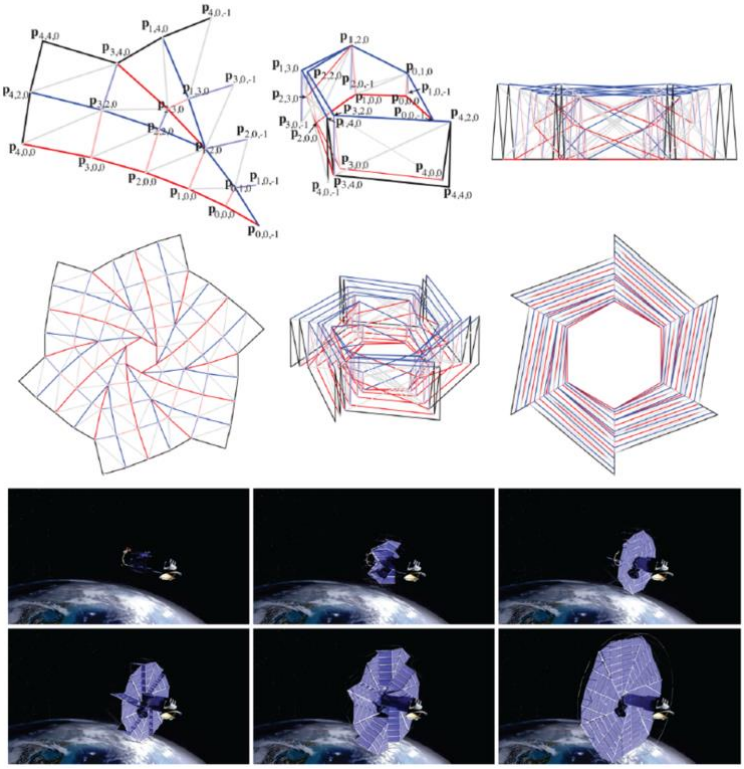

Figure 1.7 Origami self-deployable compliant solar array support, details of progressive shapes during opening.

Critical importance in similar applications has the coexistence between rigid and flexible areas within the same structure. Indeed, zones of the mechanism required to support the solar array should have enough stiffness, while the ones aimed at the deployment should be sufficiently flexible to allow the displacement without anyway let the structure collapse upon itself. Finding such a balance represents one of the major challenges on designing highly flexible structures and, as will be discussed following, a useful strategy is trying to differentiate the role of different areas belonging to the same layout through FEA and Topology Optimization. This just outlined approach allowed for example some interesting snakes bio-inspired applications, concerning among the others also the surgical field [14].

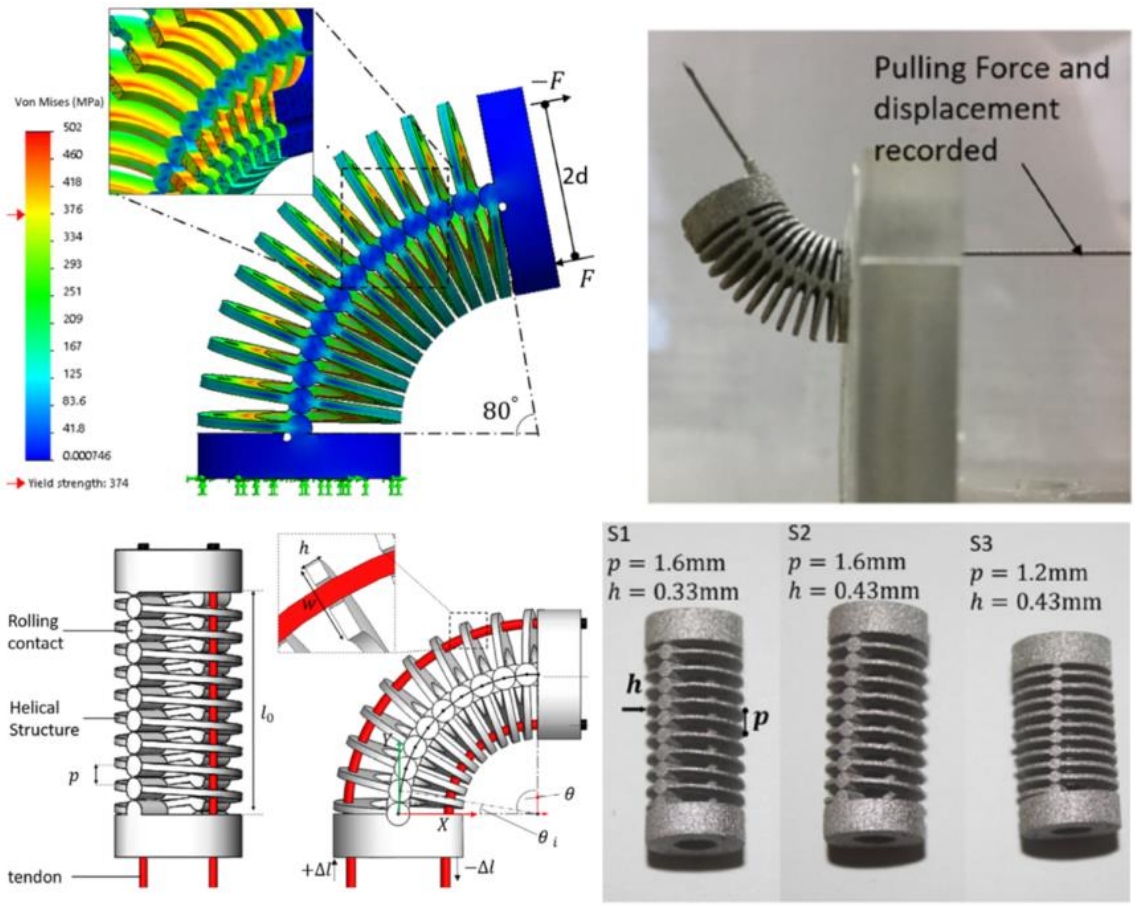

Figure 1.8 Stainless Steel Snake Bio-inspired surgical robot realized by Selective Laser Melting Additive Manufacturing

The surgical compliant instrument was realized in Stainless Steel with Selective Laser Melting (SLM), one of the metal powder bed AM processes which enables the manufacturing of metal monolithic CMs despite their shape complexity and thickness variations. The potential to withstand remarkable deformations in the elastic field makes the CMs suitable to cyclically store and release energy in a manageable manner. This ability is particularly significant in the field of unmanned vehicles, where lightening the overall weight and store energy in form of internal elastic deformation implies efficiency and battery-life improvements. In addition, flexible structures have a good behavior also in terms of introducing damping

effects, a relevant issue concerning vehicles' motion. A meaningful example of an efficient combined use of Compliant Mechanisms, FEM analysis, TO and bio-inspiration is the development of topology optimized compliant legs for bio-inspired quadruped robots [15]. Designed with the intention to overcome the issue of operating in demanding and liquid grounds, this robot deals with the challenging problem of balancing the structural stiffness and bending flexibility introducing a multi-objective optimization algorithm.

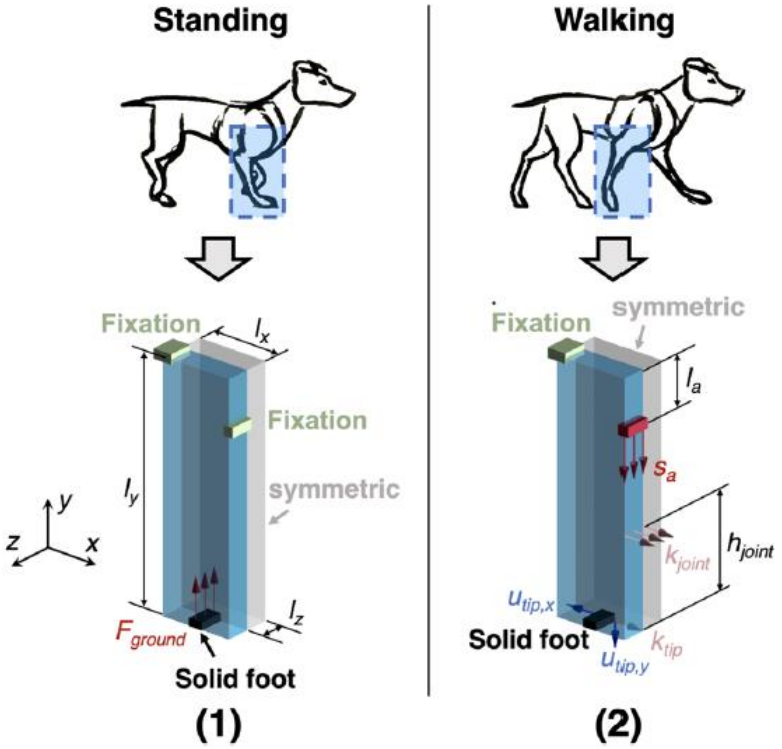

Figure 1.9 Design domain of multi-objective topology optimization where two loading conditions were imposed, standing (left) and walking (right)

Once the optimization domain, parameters and boundary conditions were set, the algorithm progressively suggests the combination of a rigid part and two flexible areas, withnessing the correct implementation of the optimization. Being a multi-objective optimization, the Pareto optimality

was correctly reached since the trend of minimum compliance and maximum displacement converges, as displayed below in Figure 1.10.

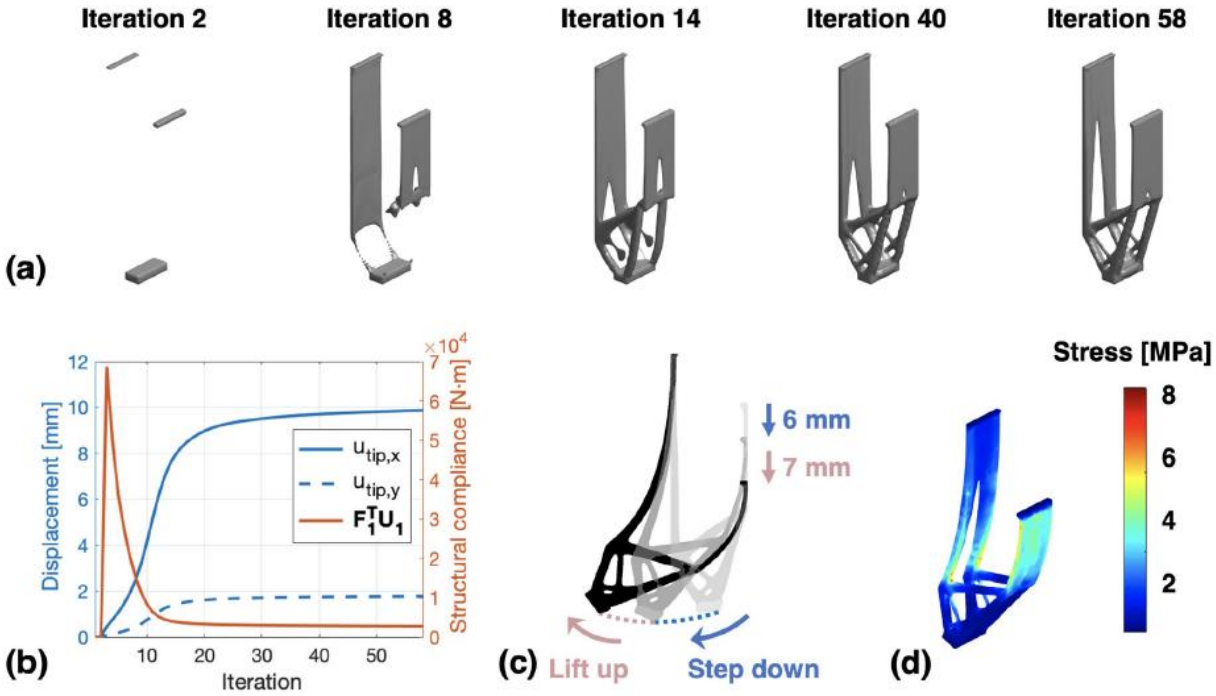

Figure 1.10 Progressive shaping of the compliant leg during the optimization process (a), trends of minimum compliance and maximum displacement (b), final shape of compliant leg and Nonlinear FEA stress map.

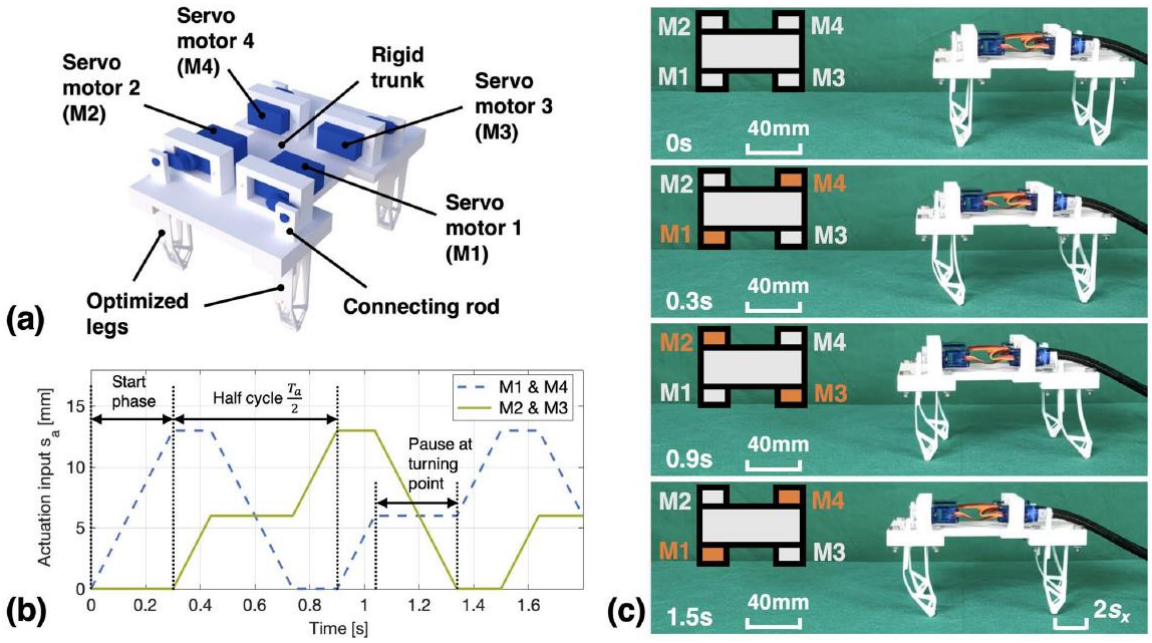

Figure 1.11. 3D printed prototype testing with a details of electronics positioning and actuation inputs during a complete walking cycle.

Even though an in-depth optimization model settlement and a following accurate nonlinear FEA are required, the development of such design strategy proves to be effective. Indeed, there are remarkable advantages such as energy storage through cyclic elastic deformation, lower friction due to monolithic layout, lower backlash, opportunity of implementing bio-inspired design and Additive Manufacturing and so on. It is also worth mentioning that, from a mechanical stress point of view, taking advantage of TO and FEA in designing flexible mechanisms is beneficial also since they provide flexible layouts where stress is distributed quite homogeneously throughout the available material (as also shown in Figure 1.10.d) consequently making the best of it, and consequently preventing the formation of localized stress concentration peaks. As following explained, this characteristic turns out to be particularly profitable when the mechanism is subjected to high frequency displacements, since inertial effects start to be onerous and make the material undergo localized stresses.

1.2 Dissertation arrangement

Considering the variety of covered topics and also the increasing complexity of design strategies presented, this paragraph provides the reader with a brief schematization of the issues following discussed. The development of Compliant Mechanisms suitable for FWMAVs actuation systems represents the main subject of the research, thus it's useful to describe them first of all. After providing an overview with the major advantages and challenges associated with CMs, a comprehensive introduction of their most common design methods is presented. For each method, the most appropriate application field were briefly described during their introduction, so as to better address the reasons for the choice of Topology Optimization over the other design methods.

As well as for other structural optimization methods, the TO essentially allows a better exploitation of material, but unlike the former, Topology Optimization enables also a smarter usage of the available design space. Indeed it has the possibility to configure several kinds of constraint conditions within a generical specified geometry, so as to customize the product exactly according to the design requirements. Moreover, in various applications the TO provides the designer with elaborate counter-intuitive layouts, which unlikely might have been conceived through a traditional design method. This just mentioned capability of TO proves to be very beneficial considering in particular the application under discussion in this

research, since the need to accommodate in a small design space a flexible mechanism has to be combined both with the large displacements and high frequency of motion requirements.

The considerations related to the choice of Flapping Wing Micro Air Vehicles as target for the compliant actuation system are outlined subsequently in a specific chapter. The interest gained by these vehicles is mainly favoured by their potential application in inspection and maintenance in hazardous areas, search and rescue in confined spaces or surveillance and military purposes. In addition to these reasons, the FWMAVs offer various technological advantages over conventional aircrafts such as better efficiency due to their lower weight, good agility in small environments and highest safety related to the lack of rotating blades, inherent to their different flight mechanism which will be deepened afterwards in the paragraph dedicated to them. Most of all, these vehicles could in particular profit from the implementation of flexible monolithic actuation systems considering the CMs' ability to cyclically store and release elastic deformation energy and therefore increasing the flight authonomy. Moreover, the absence of internal joints connecting the mechanism's parts avoids part of energy losses due to friction and also wear effects due to high frequency motion.

The usage of subractive technological processes in manufacturing complex designs such as compliant mechanisms, although still possible, proves to be less suitable than using Additive Manufacturing technologies. In this regard, just considering the coexistence of very thick and extremely thin geometrical features within the same flexible component makes it challenging the adapting of traditional manufacturing processes.

Besides, among the purposes of this research is also the design of cheaply manufacturable and customizable products, reason why low cost Fused Deposition Modeling technology has been selected among others AM processes. Below is reported a schematic representation of the connections between topics covered through this dissertation.

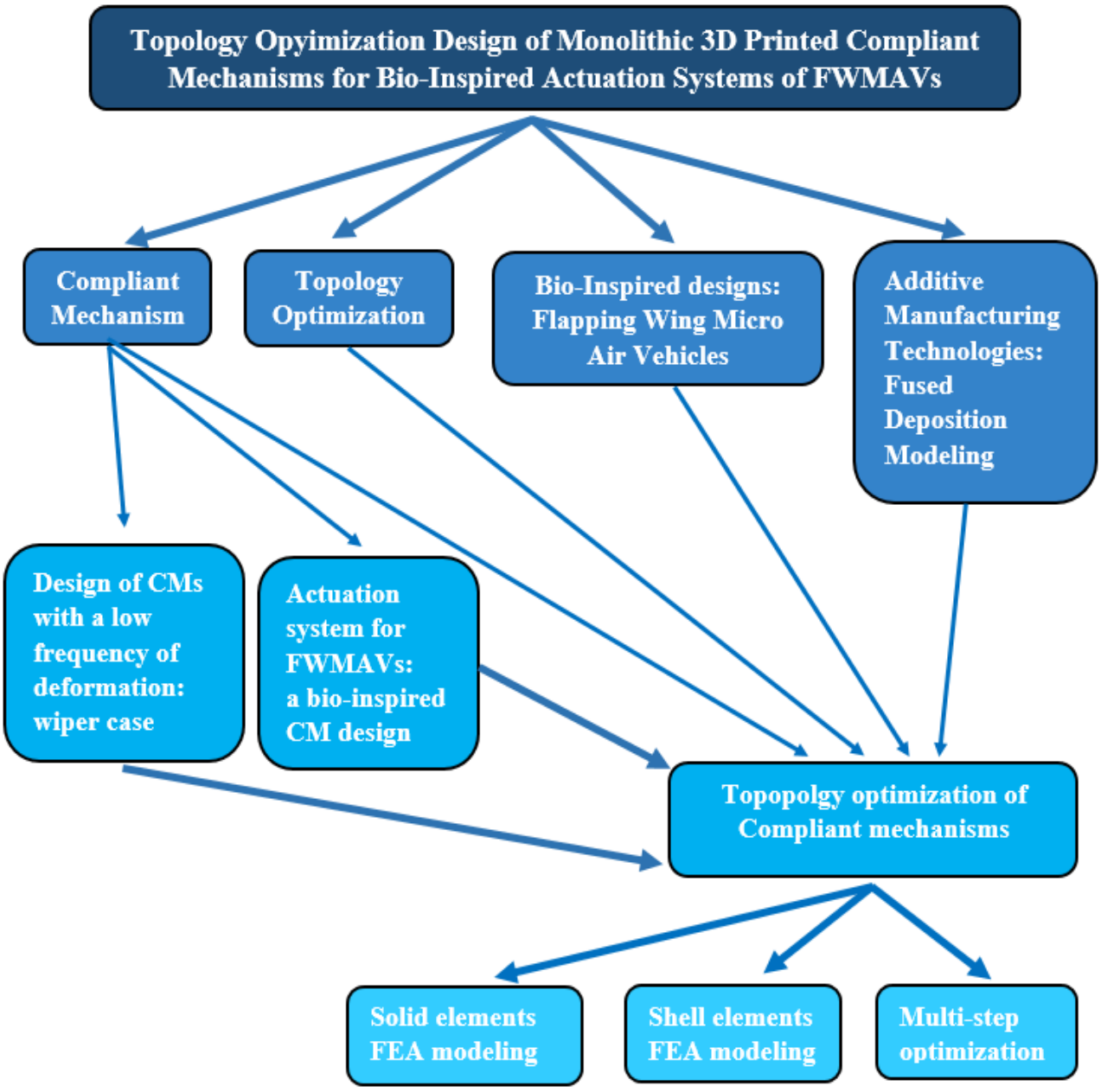

Figure 1.12. Schematic representation with dissertation's topics overview

Once introduced the background topics, some of the most relevant CMs' layouts are presented, each one developed using a different design approach, in order to explore their specific advantages and limitations in accordance with the mechanism requirements. As first application of CMs, an innovative design of a wiper with a monolithic layout was conceived exploiting FEM analysis, comparing his performances to the ones of a traditional assembled multi-component wiper realized with metal parts. Such study was initially useful to understand how to deal both with the different mechanical behaviour of flexible materials and also with AM processes, since this item was realized by FDM in a carbon reinforced nylon (Nylforce CF). Furthermore, gaining experience with this "low frequency motion" mechanism allows to show some of the main differences with the FWMAVs actuation systems, being also the wiper displacement range much more limited compared to the one required for a flapping wing vehicle, where the CM's flexible areas have to withstand more significant stresses and deformations.

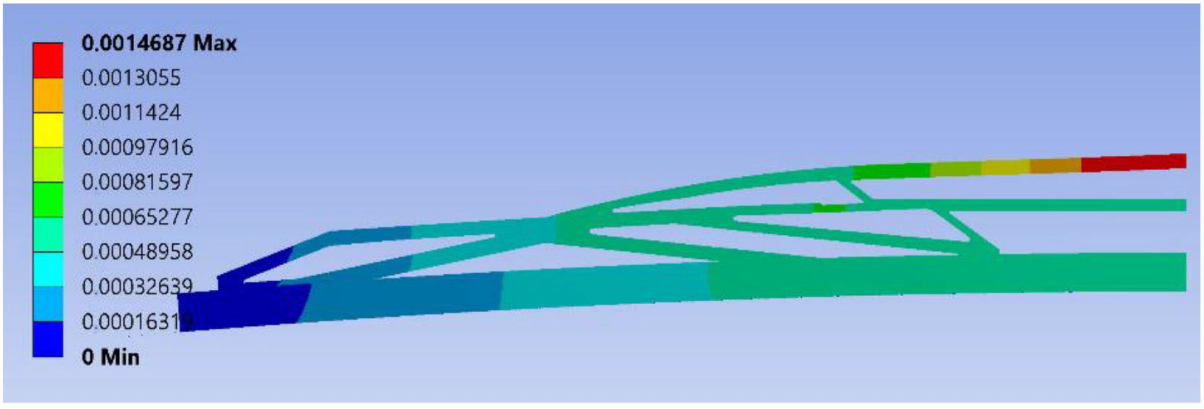

Figure 1.13. FEA detail of displacements [m] of the Nylforce CF compliant wiper

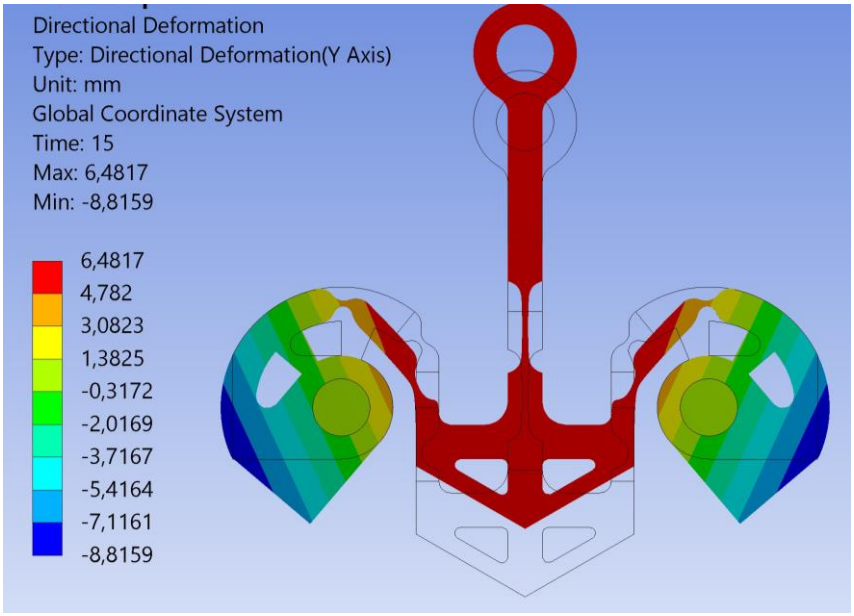

Figure 1.14. FEA vertical displacements [mm] of a conceived layout of a compliant actuation mechanism in FlexiFil.

From the images above stands out both the different amount of displacement generated in the compliant wiper and in a compliant actuation mechanism and also how the deformation dissimilarly ditributes along the two layouts.

Afterwards were described some of the bio-inspired layouts conceived by analyzing the insect's flapping mechanisms and their muscular structure.

The observation of the insects' internal structure of thorax from an engineering point of view has made it possible to redefine compliant mechanism layouts by separating the function of rigid and flexible areas.

The initial concepts were then subjected to non-linear FEA and their geometrical features were adjusted considering AM manufacturing, material's mechanical properties and the eventual space necessary for electric and electronical equipments. The performances of these designs were investigated in terms of stress, deformation, input displacement and output rotation.

Combining the experience coming from these bio-inspired concepts with a more accurate exploitation of the available design space through Topology Optimization, a progressive improvement of the FWMAVs' actuation system was reached, coupled with a better comprehension of the most critical design issues to be careful of. Although at the end of optimization process a geometrical remodeling it's necessary, the TO proves to be able to provide a material distribution unpredictable through the designer's experience or the conventional CMs' design methods. Indeed the positioning and the dimensioning of flexible and rigid areas within the design space becomes as much elaborate as more complex is the required output motion. The presented design approach is besides able to customize the flexible mechanism by adjusting the TO boundary conditions according to the design constraints.

2. Compliant Mechanisms

Conventionally when a designer is about to model a moving apparatus, it’s likely that he will employ rigid components interconnected through sliding joints or hinges (similar to a door hinge). However, a distinct approach is observed in nature where flexible elements, as opposed to rigid ones, are prevalent in most moving entities, in such a way that the movement predominantly arises from the bending of these pliable components [16] Take, for instance, the human heart, a remarkable compliant mechanism that initiates operation prior to birth and continues tirelessly throughout one's entire life, or the internal space-saving structure of a mosquito which supports at once flying, navigation and energy hasvesting systems [17].

2.1 Challenges and advantages in CMs’ design

The ever-growing availability novel materials and enhanced computational capacities made it possibile spreading the use of CMs, whose main advantages can be resumed in:

- Integrating different functions in fewer parts;
- Lower cost related to streamlined assembly process, stocking and managing a less quantity of components;

- Structural lightening useful for saving of expensive materials and weight-sensitive applications;
- Performance increase resulting from reduced wear and backlash;
- No need of lubrication and in turn less maintenance needed;
- Scalability and miniaturization of layouts;

On the other hand, while in assembled rigid mechanisms it's possible to split distinct functions among various parts, the CMs' part count reduction advantage involves a more intricate design process since all the tasks have to be achieved within the same structure [18].
Moreover, particular attention during their design is needed to deal with the following issues:

- Concurrent design addressing both motion and force aspects;
- Large deflections not manageable with linear equations;
- Limited motion compared to the full rotation of bearings;
- High deformations could lead to bistable mechanism's configurations;
- Undergoing to deformed shapes for much time could result in "stress relaxation" phenomenon;
- High motion frequencies could lead to substantial inertial effects;

A helpful consideration when going to use CMs in a design is that strenght and stiffness are basically different, since the former is related to the ability to withstand failure while the latter pertains to the ability to resist deflection. A meaningful example of how diversified use of the same material results in different product's requirements is displayed in Figure 2.1.

Figure 2.1. Topology optimized titanium bracket for aerospace (left) [19] and titanium monolithic compliant mechanism for space applications (right) [7]

While the TO titanium bracket in the left side requires both stiffness and strenght properties, minimizing any deformation, the CM in the right side necessarily needs to deflect itself, in a proper way, in order to meet his requirements. In this context, some fundamental features have to be kept in mind dealing with flexible mechanisms, which closely influence their behavior:

- Mechanical characteristics of materials;
- Shape and size of geometrical features;
- Boundary conditions, loading magnitude and frequency;

Since the desired outcome in designing CMs is a combination of flexibility and strenght, when selecting materials those with high strength and low Young's modulus are particularly valuable. A useful method for comparing materials in this regard is to assess the ratio of strenght to Young's modulus, where a higher indicates better suitability.

An alternative method involves the evaluation of the material's resilience, which provides an indication about the amount of energy per unit of volume that a material can endure without undergoing a permanent deformation. The modulus of resilience can be calculates as one-half the yield strenght squared divided by the Young's modulus. Below in Figure 2.1 is provided a table of common materials compared considering their yield strength to Young's

Material	E (GPa)	S_y (MPa)	$(S_y/E) \times 1000$	$(0.5 \times S_y^2/E) \times 0.001$
Steel (1010 hot rolled)	207	179	0.87	77
Steel (4140 Q&T @400)	207	1641	7.9	6500
Aluminum (110 annealed)	71.7	34	0.48	8.1
Aluminum (7075 heat treated)	71.7	503	7.0	1800
Titanium (Ti-35A annealed)	114	207	1.8	190
Titanium (Ti-13 heat treated)	114	1170	10	6000
Nitinol (high-temperature phase)	75	560	7.5	2100
Beryllium copper (CA170)	128	1170	9.2	5300
Polycrystalline silicon	169	930	5.5	2600
Polyethylene (HDPE)	1.4	28	20	280
Nylon (type 66)	2.8	55	20	540
Polypropylene	1.4	34	25	410
Kevlar (82 vol%) in epoxy	86	1517	18	13 000
E-glass (73.3 vol%) in epoxy	56	1640	29	24 000

Figure 2.2. Materials classification based on yield strenght to Young's modulus ratio and resilience

modulus ratio and resilience values. Under the same material conditions, geometrical features have an important influence on the overall behaviour of CM and they are closely dependent on boundary and loading conditions.Indeed a different distribution of material enables the mechanism to rigidly react along determined load directions and to deform along others. Considering for instance the need to reduce the output rotation [20], as can be seen from the following Figure 2.3. In this case, the required minimization of output rotation is reached through a very accurate system of thin flexible areas.

The geometry features are able to transform the input rotation in such a way that the mechanism deforms internally, distributing more evenly possible the deformation energy, in order to avoid the creation of stress concentrations.

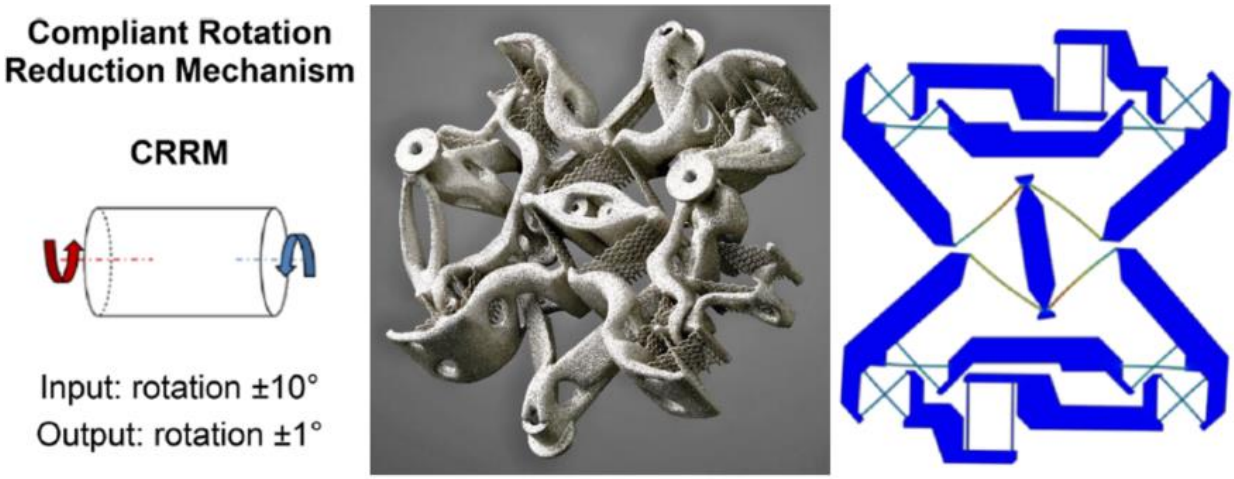

Figure 2.3. Compliant rotation reduction mechanism, concept, prototype and FEA

Another important aspect to focus attention on is the "Off-axis stiffness", which can be described as the stiffness concerning an undesired axis divided by the the stiffness along the axis around which the motion must take place. A high off-axis stiffness suggest that the mechanisms has robust resistance to motion in unwanted directions. Conversely, a low ratio implies an element more susceptible to undesired movements under external loads. An high off axis stiffness is often required in CMs' design, and this could be reached by lowering the stiffness in the axis of desired rotation or increasing the stifnesses in the undesired directions. To clarify this concept, an example of compliant flexural pivot is reported below in Figure 2.4 [21]. In this rotational pivot the body a is fixed while b is able to rotate around the c axis. This layout has the ability to maintain constant stiffness despite the force applied to the rotating body "b", respecting the geometrical conditions given in Figure 2.4 [16][21].

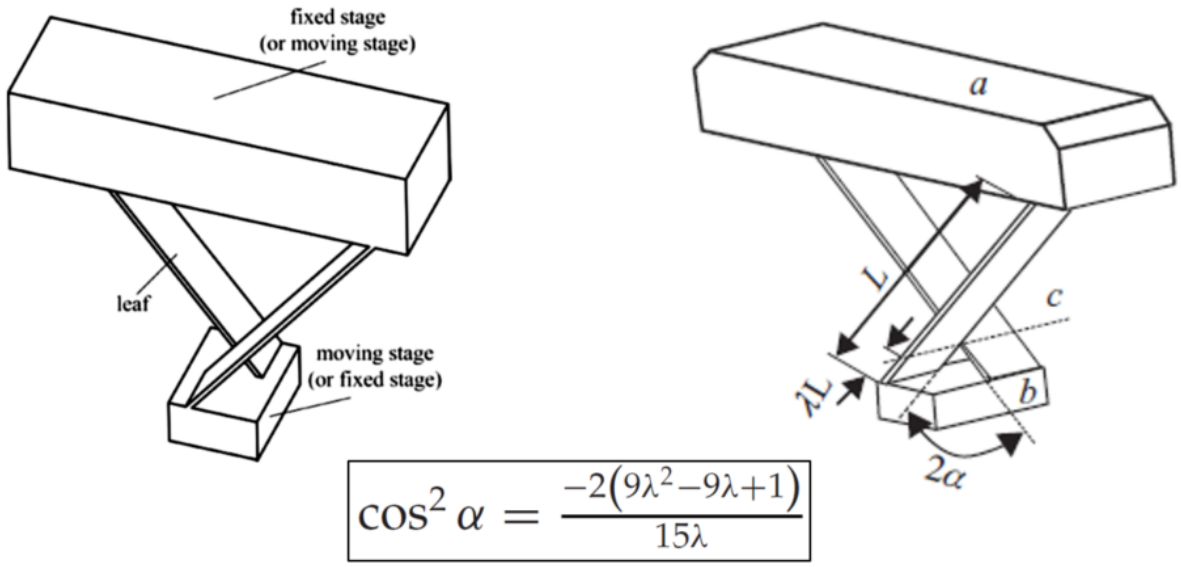

Figure 2.4. High off-axis stiffness: Costant stiffness cross-axis flexural pivot

Following will be described some of the most widespread CMs' design methods, each one more appropriate to specific situations depending on the project requirements.

2.2 Modeling of Compliant Mechanisms in intermediate and large displacement range

Considering at first the boudary conditions belonging to the motion of a flexure mechanism, degrees of freedom (DoF) indicates lower stiffness directions while degrees of constraint (DoC) are related to orientations of significantly higher stiffness. The following parallelogram flexure mechanism for instance has two DoC (in X and θ) and only one DoF in Y direction assuming a planar motion. It can be easily noticed that as displacement along Y direction increases there's also a decline of the

stiffness on X and θ directions. Likewise, the stiffness on Y direction enhances or decreases respectively applying a tensile or a compressive force in X direction.

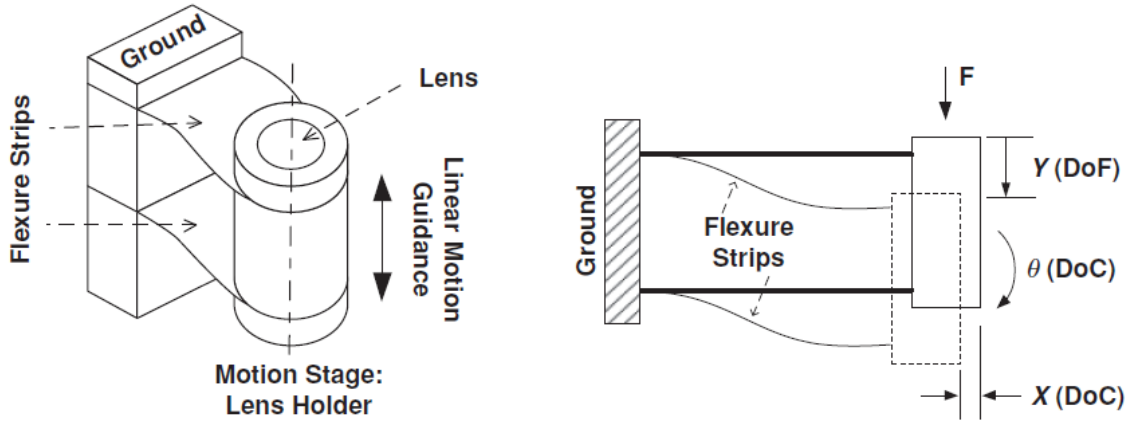

Figure 2.5. Degrees of freedom and degrees of constraint of a parallelogram flexure mechanism

Indeed it can be stated from analytical and experimental findings that the abovementioned aspects are heavily reliant on geometric nonlinearities, which are not detectable through a linear-elastic model but only using nonlinear FEA or accurate mathematical models which are anyway tricky to be achieved. In order to take into account geometric nonlinearities, it's useful considering two ways of solving the following standard mechanics equation based on Euler and Bernoulli assumption. Hereinafter E indicates Young's modulus, Mz the moment, Izz the second moment of area on Z axis, ρ the radius of curvature.

$$\frac{E}{\rho(X)} = \frac{M_Z(X)}{I_{ZZ}}$$

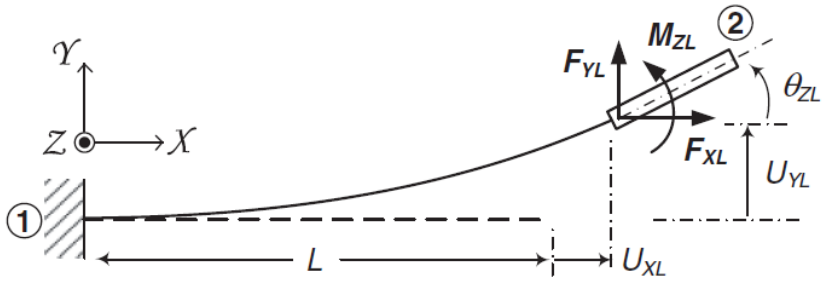

Figure 2.6. Beam model graphical representation related to standard mechanics formulation

The bending moment equilibrium can be applied in the undeformed (Eq.2.1.a) or in the deformed configuration (Eq 2.1b) as outlined below:

(a) $M_Z(X) = M_{ZL} + F_{YL}(1 - X)$

(b) $M_Z(X) = M_{ZL} + F_{YL}(1 + U_{XL} - X) - F_{XL}(U_{YL} - U_Y(X))$

Equation 2.1. Bending moment equilibrium in the undeformed (a) and deformed (b) configuration of the beam

While the former is valid only with small displacements, the latter considers how the rotation of cross-sections affects axial strain. Next it's possible to define the beam curvature both considering deformations constituting less than 10% of the beam's length or in generic conditions.

(a) $\frac{1}{\rho(X)} = Y''(X)$ (b) $\frac{1}{\rho(X)} = \frac{Y''(X)}{(1 - Y'(X)^2)^{+1/2}}$

Equation 2.2. Beam curvature for deformations less than 10% of the beam's length (a) and in generic conditions (b)

Substituting the equations from Eq 2.1a and 2.2a in the equation in Fig.2.6 is obtained a linearized form of the differential equation for the beam (Equation 2.3a), solvable using the assumption that the cross sections remain the same along the length of the beam. This one is unable to observe geometric nonlinearities, and provides true results only with small axial load and displacements less than 10% of beam's length. Otherwise using equations 2.1b and 2.2b the more general nonlinear differential equation of beam can be determined (Eq 2.3b) [16]. This equation however turns out difficult to solve when generic loads are applied at the beam's end.

(a) $$EI_{ZZ}U_Y''(X) = \boldsymbol{M_{ZL}} + \boldsymbol{F_{YL}}(1 - X)$$

(b) $$\frac{EI_{ZZ}Y''(X)}{(1 - Y'(X)^2)^{+1/2}} = \boldsymbol{M_{ZL}} + \boldsymbol{F_{YL}}(1 + U_{XL} - X) - \boldsymbol{F_{XL}}(U_{YL} - U_Y(X))$$

Equation 2.3. Linearized beam governing equation (a) and nonlinear beam differential equation (b)

Besides FEM analysis approach, which precisely considers nonlinearities, some accurate solutions can be numerically achieved through elliptic integrals although only for particular loads and beam cross sections.

A simplified approach defined as Beam Constrained Model (BCM) involves the partial linearization of beam equation using the approximate curvature (Equation 2.2a) but employing the precise load equilibrium (Equation 2.1b) providing the following equation (Eq 2.4a). Once solved, it can be obtained two parametric relations concerning loads and displacements at the end of a simple beam (Equation 2.4 b,c)[16].

(a) $$EI_{ZZ}U_Y''(X) = \boldsymbol{M_{ZL}} + \boldsymbol{F_{YL}}(1 + U_{XL} - X) - \boldsymbol{F_{XL}}(U_{YL} - U_Y(X))$$

(b) $$\begin{bmatrix} \boldsymbol{F_{YL}}L^2/EI_{ZZ} \\ \boldsymbol{M_{ZL}}L/EI_{ZZ} \end{bmatrix} = \begin{bmatrix} k_{11}^{(0)} & k_{12}^{(0)} \\ k_{12}^{(0)} & k_{22}^{(0)} \end{bmatrix} \begin{bmatrix} \frac{U_{YL}}{L} \\ \theta_{ZL} \end{bmatrix} + \frac{\boldsymbol{F_{XL}}L^2}{EI_{ZZ}} \begin{bmatrix} k_{11}^{(1)} & k_{12}^{(1)} \\ k_{12}^{(1)} & k_{22}^{(1)} \end{bmatrix} \begin{bmatrix} \frac{U_{YL}}{L} \\ \theta_{ZL} \end{bmatrix}$$

(c) $$\frac{U_{XL}}{L} = \frac{1}{k_{33}}\frac{\boldsymbol{F_{XL}}L^2}{EI_{ZZ}} + \begin{bmatrix} \frac{U_{YL}}{L} & \theta_{ZL} \end{bmatrix} \begin{bmatrix} g_{11}^{(0)} & g_{12}^{(0)} \\ g_{12}^{(0)} & g_{22}^{(0)} \end{bmatrix} \begin{bmatrix} \frac{U_{YL}}{L} \\ \theta_{ZL} \end{bmatrix}$$
$$+ \frac{\boldsymbol{F_{XL}}L^2}{EI_{ZZ}} \begin{bmatrix} \frac{U_{YL}}{L} & \theta_{ZL} \end{bmatrix} \begin{bmatrix} g_{11}^{(1)} & g_{12}^{(1)} \\ g_{12}^{(1)} & g_{22}^{(1)} \end{bmatrix} \begin{bmatrix} \frac{U_{YL}}{L} \\ \theta_{ZL} \end{bmatrix}$$

Equation 2.4. Simplified beam differential equation with Beam Constrained Model (a) and parametric BCM relations for simple beam considering end loads and displacements

Despite it's a simple parametric model, BCM effectively provides solutions just for an intermediate displacement range, i.e. displacements lower than 10% of beam's length. Below is reported a diagram of elastic stiffness and load-stiffening coefficients for simple beam, with a comparison of BCM and nonlinear FEA results [16]. It can be noticed that the higher deviations from FEA begin to occur when displacements u_y or θ_z increase (the horizontal axis is normalized on the beam's length).

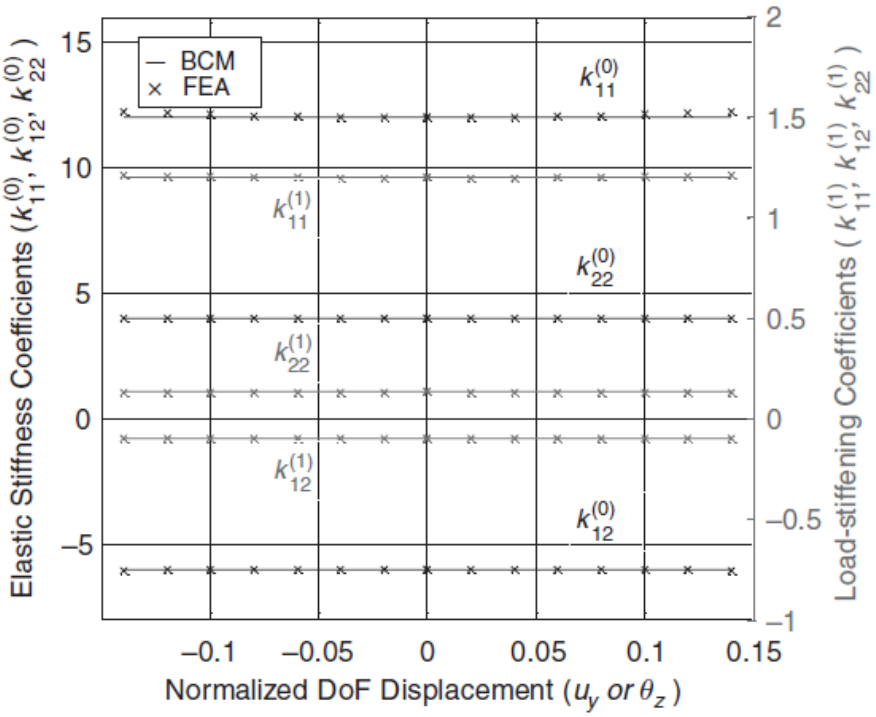

Figure 2.7. Graphical comparison of elastic stiffness and load-stiffening coefficients for a simple beam modeled through BCM and FEA

Indeed, it's interesting considering that the load-stiffening effect appears also using the BCM model, and therefore in the intermediate displacement range, since applying a tensile or compressive force along the X direction has respectively an influence on the increasing or the reduction of stiffness in Y direction, as already seen in Figure 2.5 with a parallelogram flexure mechanism.

One of the options to take into account large displacements in a CM's design is recurring to the elliptic integrals such as the ones shown following as F(k,ϕ) and E(k,ϕ).

(a) $$\sqrt{\alpha} = F\,(k, \phi_2) - F\,(k, \phi_1)$$

(b) $$\frac{b}{L} = -\frac{1}{\sqrt{\alpha}}\left\{2k\cos\psi(\cos\phi_1 - \cos\phi_2) + \sin\psi\,[2E\,(k, \phi_2) - 2E\,(k, \phi_1) - F\,(k, \phi_2) + F\,(k, \phi_1)]\right\}.$$

(c) $$\frac{a}{L} = -\frac{1}{\sqrt{\alpha}}\left\{2k\sin\psi(\cos\phi_2 - \cos\phi_1) + \cos\psi\,[2E\,(k, \phi_2) - 2E\,(k, \phi_1)] - F\,(k, \phi_2) + F\,(k, \phi_1)]\right\}.$$

Equation 2.5. Nonlinear beam equations based on elliptic integrals F(k,ϕ) and E(k,ϕ), describing the force (a), the horizontal and vertical deflections (b,c) at the beam's end.

Known the boundary conditions, displacements along the constant thickness beam can be achieved by solving the above equations through nonlinear numerical solution. Otherwise, knowing the displacements along the beam it's possible vice-versa to obtain the forces at beam's ends. An illustrative example of this nonlinear solution is shown below in Figure 2.8 implemented on a steel beam with a rectangular section of 50 x 10mm, fixed at one end and loaded in the other with different orthogonal forces from 500 to 8000 N [16]. Two particular characteristics stands out from this elliptical integrals model:

- The loaded end forms an approximately circular path, centered nearer to the fixed end.
- As the force intensifies, the beam displays increased stiffness.

From the first consideration originates the Pseudo Rigid Body Model (PRBM, following introduced), where the movement of a flexible beam is depicted by combining a rigid link fastened to a second rigid link. The second point moreover is applied in PRBM to take into account that, as the horizontal displacement amplifies, the moment acting on the beam descreases.

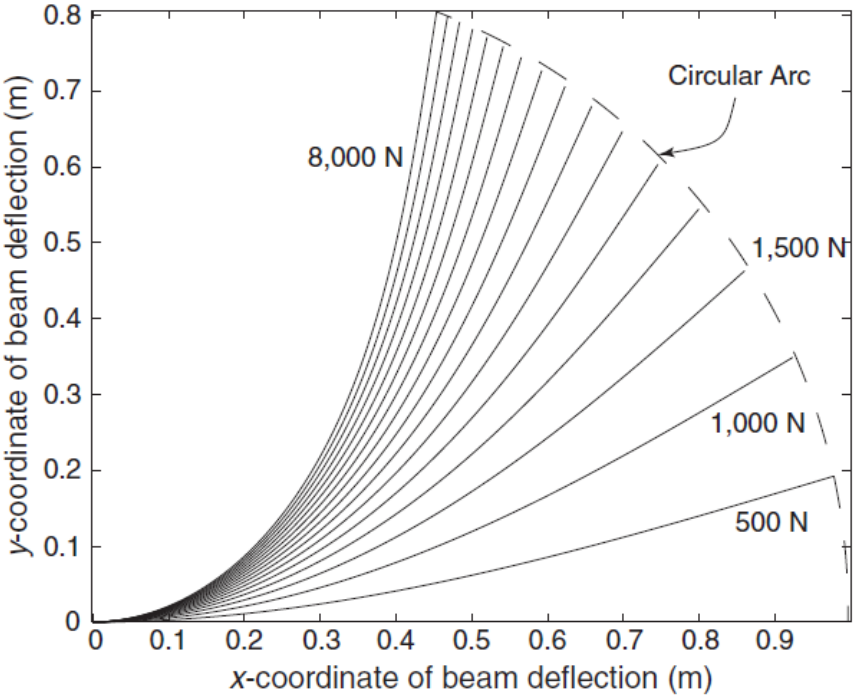

Figure 2.8. Nonlinear beam modeling via elliptic integrals: deflections of a steel beam loaded with vertical forces from 500 to 8000 N

Moreover, elliptic integral solution for flexible beams subjected to large deflections proves to be specifically effective in foreseeing the motion of buckled beams, since it can provide the first and the second mode bending deflections. Knowing these ones is a significant issue mainly dealing with compliant bistable mechanisms, also considering that a simple FEA model is not equally effective in predicting bending deflections.

Pseudo Rigid Body Modeling (PRBM) is a valuable tool for CMs'design that enable the representation of flexible bodies through rigid bodies properly connected together with flexible segments. Indeed, for each loading condition and for a specific configuration, it's possible to find a pseudo-joint position, where a torsional spring is placed and where the flexible body can be divided in rigid bodies. A simple configuration of a flexible planar beam fixed at one end and loaded on the other is following reported (Figure 2.9)[16] to better display PRBM method. The length γL, named characteristic radius, is referred to the length of the pseudo-rigid link (Figure 2.9 left), in which the factor γ is called characteristic radius factor. The torsional spring indicated below has a characteristic stiffness K, while E, I and L are Young's modulus, second moment of area and length of the flexible beam. In this precise configuration, the length of the pseudo-rigid link is between 0.83L and 0,85L. The angle of rotation of loaded end is represented by Θ, which is related to the coefficient γ: if small deflections are expected, using 0,83L is preferable while for large deflections 0,85L is

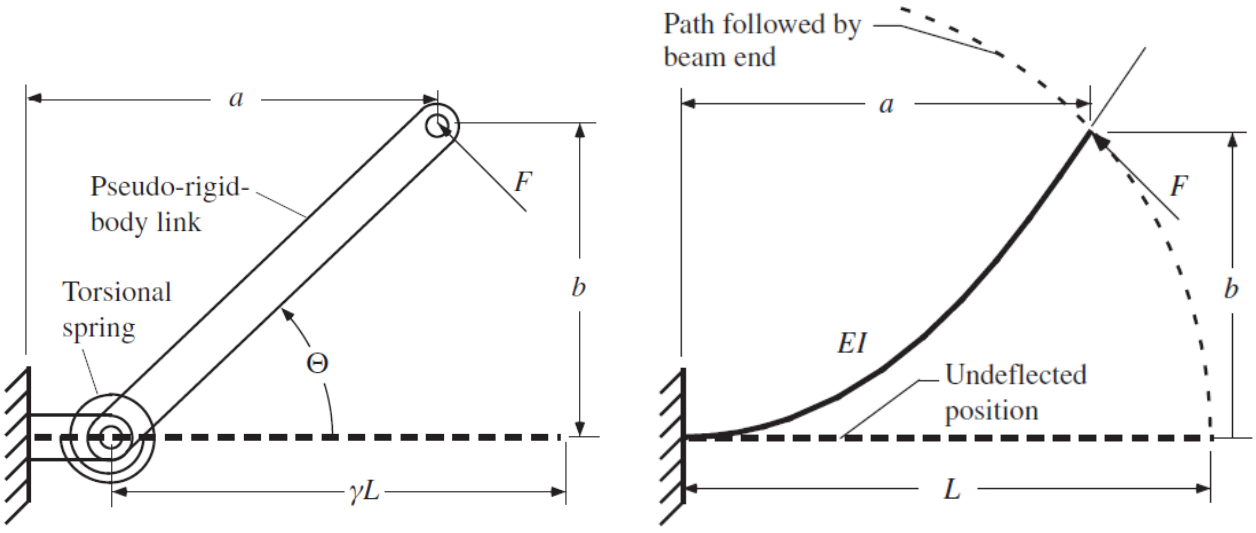

Figure 2.9. PRBM model (left) of a compliant beam (right) fixed and loaded with an orthogonal force, with details of the main geometrical parameters

more accurate to be used as characteristic radius. Therefore, displacements of PRBM equivalent configuration are available once known the characteristic factors for a specific load condition and a flexible beam configuration. Following are reported as example the equations showing the X and Y coordinates (a, b) and the torsional spring's stiffness.

$$a = (1-\gamma)L + \gamma L \cos\Theta \qquad K = 2.25\, EI/L$$
$$b = \gamma L \sin\Theta$$

Equation 2.6. PRBM parameters of a compliant beam fixed and loaded: a and b are related to the x and y displacement, K is the stiffness of the torsional spring.

Defining the relative errror as the error in predicted displacement divided by the total displacement from the undeformed condition, it result to be less than 0,5 % assuming a load constantly applied on the beam's tip with the same direction [22]. A number of these examples have been extracted for different configurations ad are available in literature [16] to predict CMs experiencing large deflections, under the assumption that the flexible segments maintain a uniform cross-section, exibit homogeneous material properties remaining within the elastic limits. A more intuitive approach for CMs design is represented by the Freedom and Constraint Topologies (FACT) which is an interesting method useful for identifying a suitable concept. After identifying a desired DOF configuration, this method provides an existing library of solutions (Figure 2.10 [23]) where for each Freedom Space (referred to DOFs needed) is matched only one corresponding exclusive complementary Constraint Space, illustrating the areas where the compliant constraints could potentially be positioned enabling the desired motions.

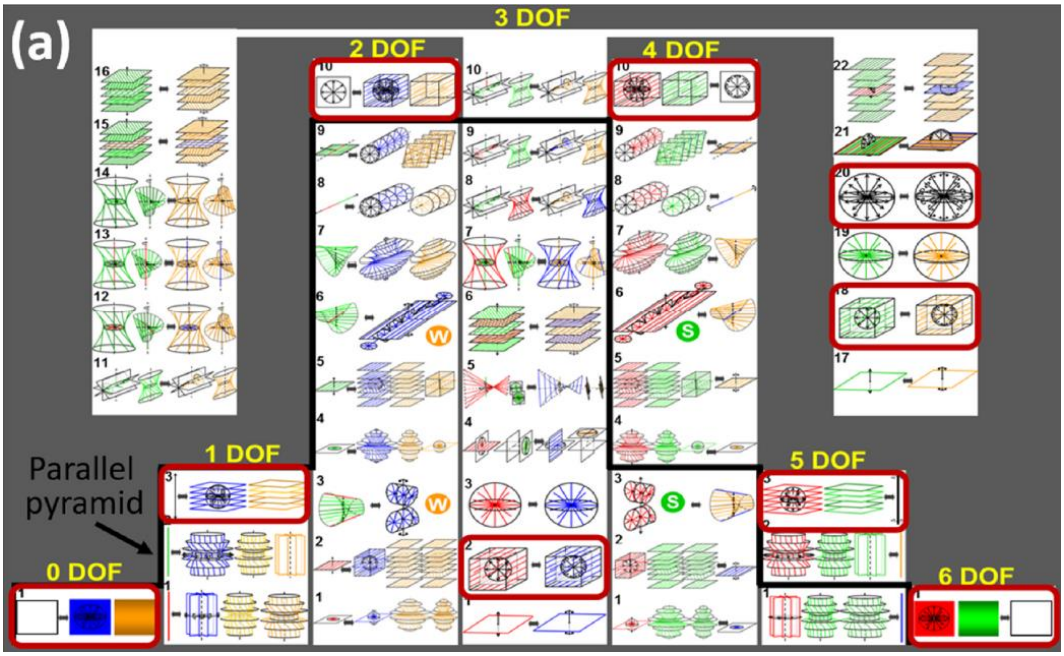

Figure 2.10. Library of Freedom and Constraint Topologies detailed for each number of Degrees of Freedom desired on the Compliant Mechanism [23]

Within the same cathegory of DOFs there are kinematically equivalent mechanisms, which differ in properties such as stiffness, loading potential, symmetry and so on. An example of FACT application on a ball joint is reported below [16]. The three rotational axis required for motion are displayed in Fig. 2.11a, with their corresponding freedom and constraint spaces, this ones represented by intersecting lines converging on the ball joint. For these three constrained lines to be considered independent, it's crucial that they don't lie within a single plane simultaneously (Fig. 2.11c). Finally, the stiffness and load capacity of mechanism is addressed through the dimensioning of the constrained flexible members. Apart from applications on precision, manipulation and nanoscale mechanisms, FACT method finds application also in Directionally Compliant Metamaterials (DCMs) which perform an adjustable anisotropy foreseen by imposing specific flexibility and stiffness directions (Fig.2.12)[24].

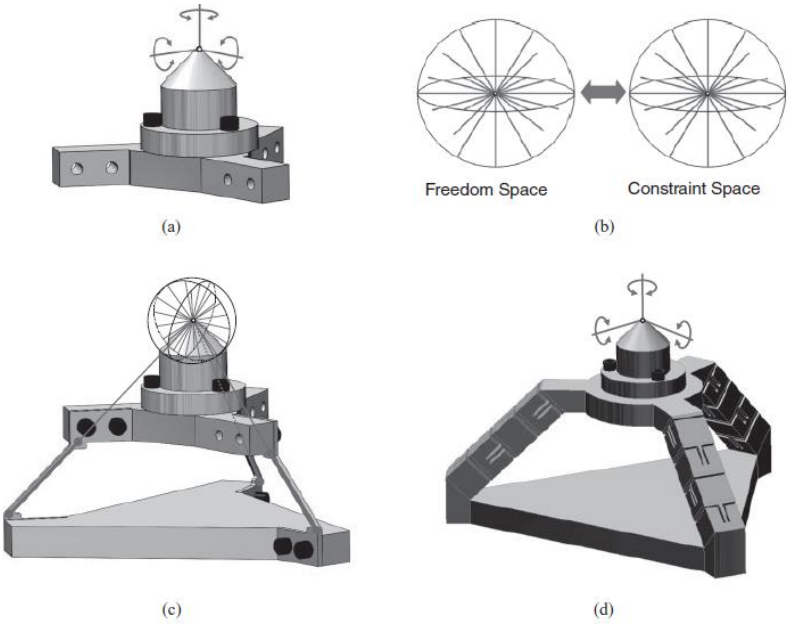

Figure 2.11. Definition of CMs layout using FACT method: required DOFs (a), freedom and corresponding constraint space (b), constraints definition (c), kinematically equivalent mechanism with proper dimensioning of constraints (d) [16].

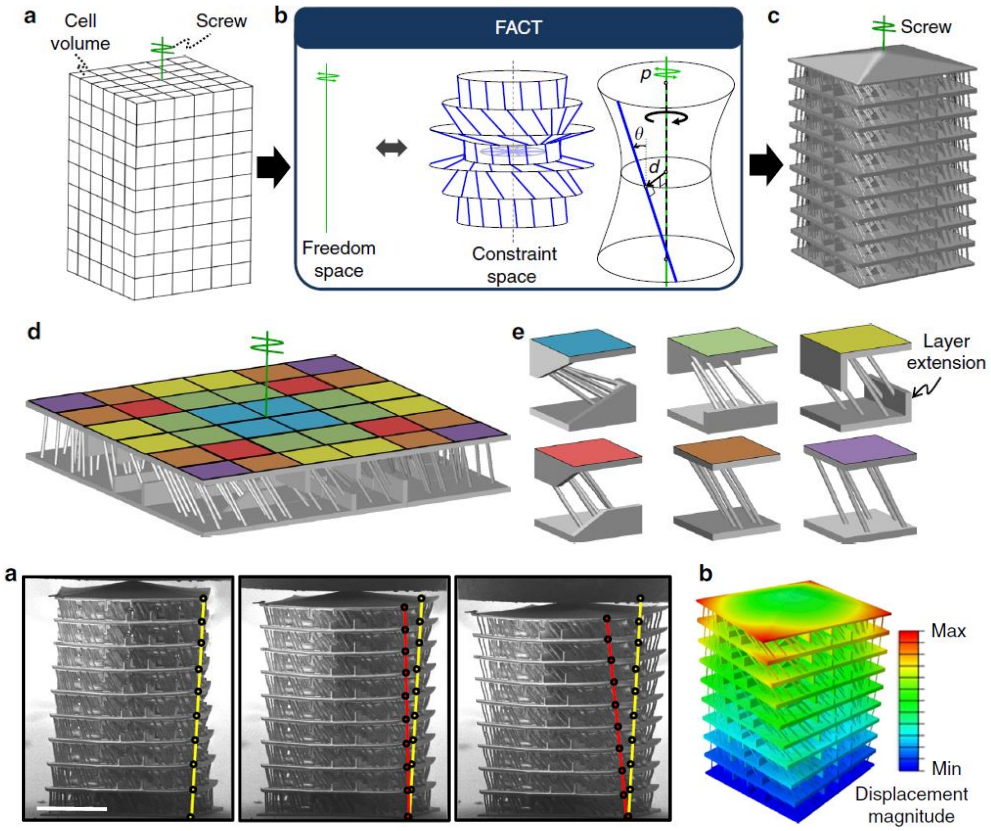

Figure 2.12. Directionally Compliant Metamaterial designed through FACT method: division of the available volume in unit cells with specific constraints, details of compression experiment on prototype and comparison with FEA displacement [24]

One of the most practical and widespread method for CMs'design is the Rigid Body Replacement procedure, which takes advantage of Pseudo Rigid Body Modeling to identify an appropriate flexible mechanism to perform a desired task or to be equivalent to an original rigid body mechanism. This approach has the advantage of exploiting both traditional rigid-body mechanism analysis and existing rigid mechanisms, adding all the aforementioned benefits of CMs, but also precluding the replacement od some mechanisms where rigid body joints are required to carry out continuous rotations. Moreover, the need of associating the CM to a corresponding rigid body mechanism represents a relevant limitation, since this method is unable to conceive new layouts, unlike the Topology Optimization method detailed afterwards. An example of Rigid Body Replacement is briefly reported below, applied to a bycicle derailleur, whose rigid body mechanism is originally made up by four bars and a spring to store potential energy (Figure 2.13 [16]). Once identified the rigid body

Figure 2.13. Bycicle derailleur and a representation of his rigid body mechanism

mechanism, it has to be chosen the rigid components to be replaced with flexible ones, in this case represented by one compliant fixed-fixed beam.

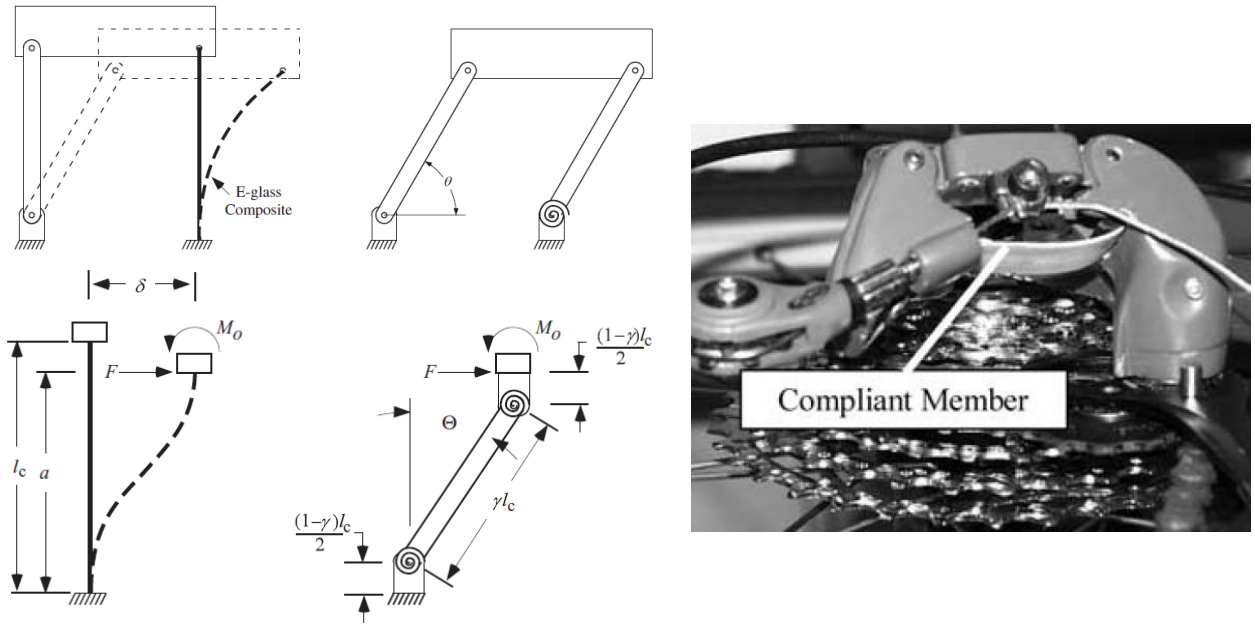

Figure 2.14. Four bar mechanism, PRBM representation of fixed-fixed flexible beam, and bycicle derailleur with the integration of compliant member [25]

The PRBM model of the beam with his parameters is developed in order to verify that the kinematic behaviour is the same of the original mechanism. Finally, consideration about the material selection are made, closely related to admissible stresses and deflections. In this case, E-glass composite has been chosen for his high ratio σ_{yield} / E, providing a weight reduction of 10%, reducing friction and also avoiding the use of the spring, given the potential energy storage capability of the flexible member. Attempting to overcome the limitations imposed by these CMs design methods, the following chapter is focused on the Topology Optimization instrument, which results to be a unique tool especially when there is not a specific CM to be based on. Moreover, through this tool unique solutions can emerge that the designer may not have reached through methods such as transforming a known rigid-link mechanism into a compliant one.

3. Topology Optimization

The kinematics-centered methods, such as the ones described above, although well-structured and extensively applicable in CMs'design, sometimes necessitate substantial intuition and specific expertise from designers. Compliant mechanisms developed through these approaches besides tend to exhibit concentrated compliance, implying that only the material proximal to the hinges affects deflection at the output areas when the mechanisms are under load. Consequently, such compliant mechanisms prove highly challenging to downsize for application at the micro or nano-scale, since a highly flexible area with a small cross-section, due to the miniaturization, could result in unbearable stress peaks compared to the mechanical properties of material. In contrast, Topology Optimization techniques are favored for designing devices compatible with MEMS (Micro Electro Mechanical Systems). These methods indeed are able to suggest to the designer novel layouts of distributed compliant mechanisms, making them better suited for such miniature applications, since a more distributed compliant mechanism provides a better distribution of deformation throughout the entire structure. After a brief initial overview of different structural optimizations, the major Topology Optimization methods implemented on CMs were introduced.

3.1 Comparison of the main structural optimization methods

Structural optimization has the aim of improving the performances of a structure so that specified requirements can be obtained, according to precise boundary and load conditions. A designer indeed could be interested in optimizing several structural aspects, defined through objective functions, that could be related to a maximum allowable stress or weight, to the reaching of a given output displacement or force, or also to the definition of a more stiffer or flexible structure. These objectives closely depend on design variables such as geometrical or material parameters, while manufacturing constraints could also be taken into account according to the foreseen production process. Approaches to structural optimization typically fall into three main categories based on design variables: size, shape, and topology optimization. The first one is related to the local optimization of geometric features such as predefined dimensions, thickness, areas, inertia or cross-sections. Size optimization however assumes that the structure's design is already in a conclusive phase, since it proves to be particularly beneficial for further refinement of an existing product, where the internal member's arrangement remains unaffected.

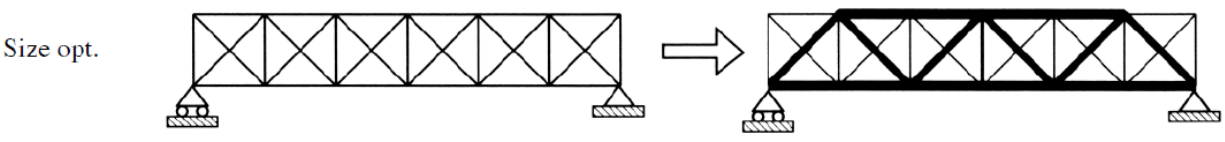

Figure 3.1. Schematization of the effects of size optimization applied on a simple structure, resulting in diversified thicknesses of the beams [26]

Although size optimization is able to affect only limited geometrical aspects, its usefulness is noticeable in the final fine-tuning of complex structures, such as the back frame of a large aperture telescope reported below [27].

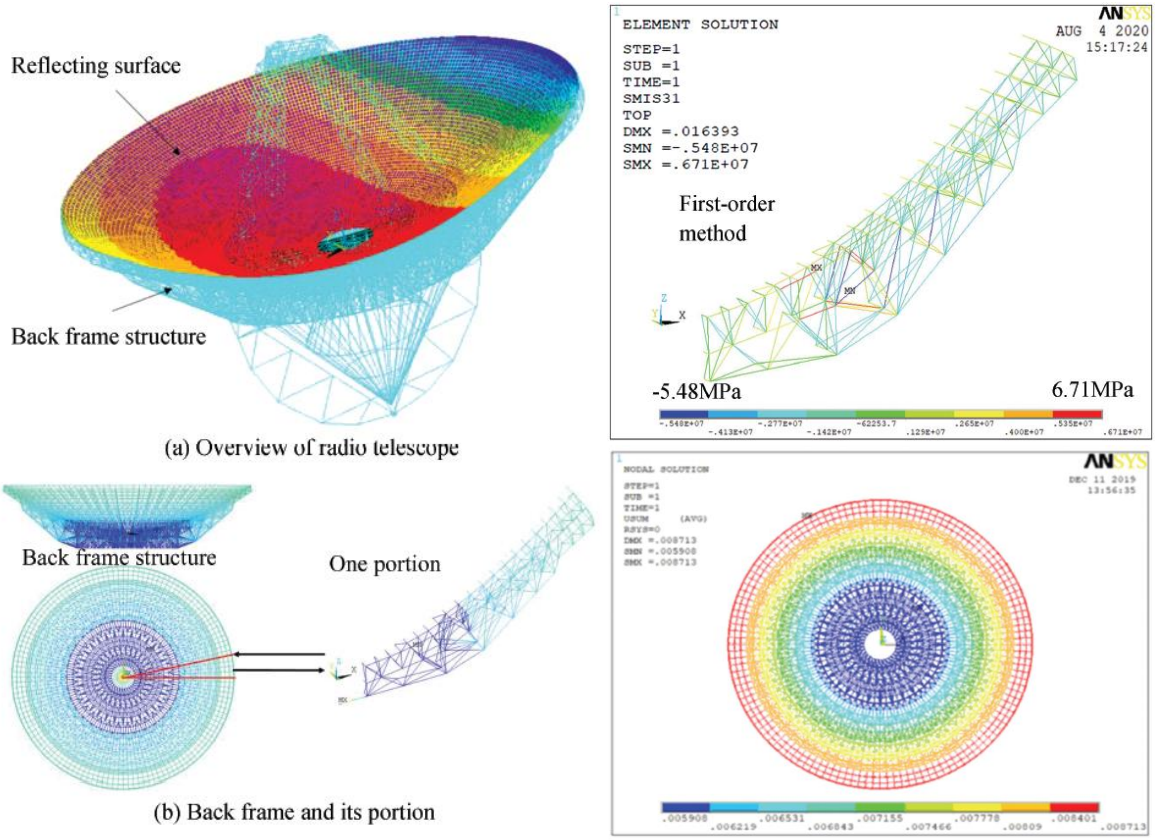

Figure 3.2. Back frame of large aperture telescope, subjected to FEA and size optimization to find the optimal cross-section size of structural parts [27]

Otherwise, shape optimization pertains to the overall designed parts, and it's able to address shape and curvature of structural elements or also their respective positioning but, similarly to size optimization, the number of internal components stays the same. For instance, shape optimization doesn't create empy volumes but it's effective in shaping the already existent contours. As above, this method is more suitable to the enhancement of an almost defined design, although allowing more impactful geometrical modifications in comparison with size optimization.

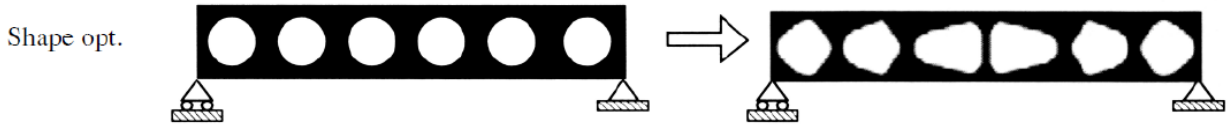

Figure 3.3. Representation of the curvature changes due to shape optimization [26]

The term topology refers to the arrangement of members and their connections within a structure. In this context, the design domain defines the space where the structure is allowed to be developed. The striking feature of Topology Optimization is related to his capability of determining the material distribution along the design domain by suggesting to the designer whether a precise volume should be empty or not. This fundamental characteristic is particularly appreciable in the early stages of design, since it's possible to reduce the number of iterations and structural verifications, which usually occur only when the structure is sufficiently defined. Different typologies of TO will be following detailed, especially in relation to CMs'design, but basically their working principle relies on the subdivision of the design domain in unitary elements, which are subjected to a gradual process of erosion, different for each method, through the application of precise mathematical algorithms. If this procedure reaches a convergence for the required optimization parameters then the optimized structure can be found, otherwise some adjustments on the design variables or established parameters needs to be made.

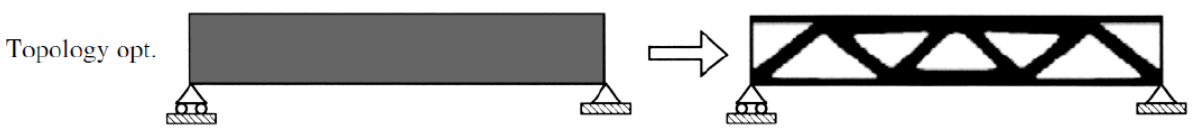

Figure 3.4. Initial design domain and material distribution resulting from TO [26]

According to the specific requirements of each application, each one of the previous optimization methods could possibly turns out to be the most suitable for the purpose, and sometimes they could be exploited also in a combined way such as the one reported below for the optimization of a marine structure for offshore wind turbines support [28].

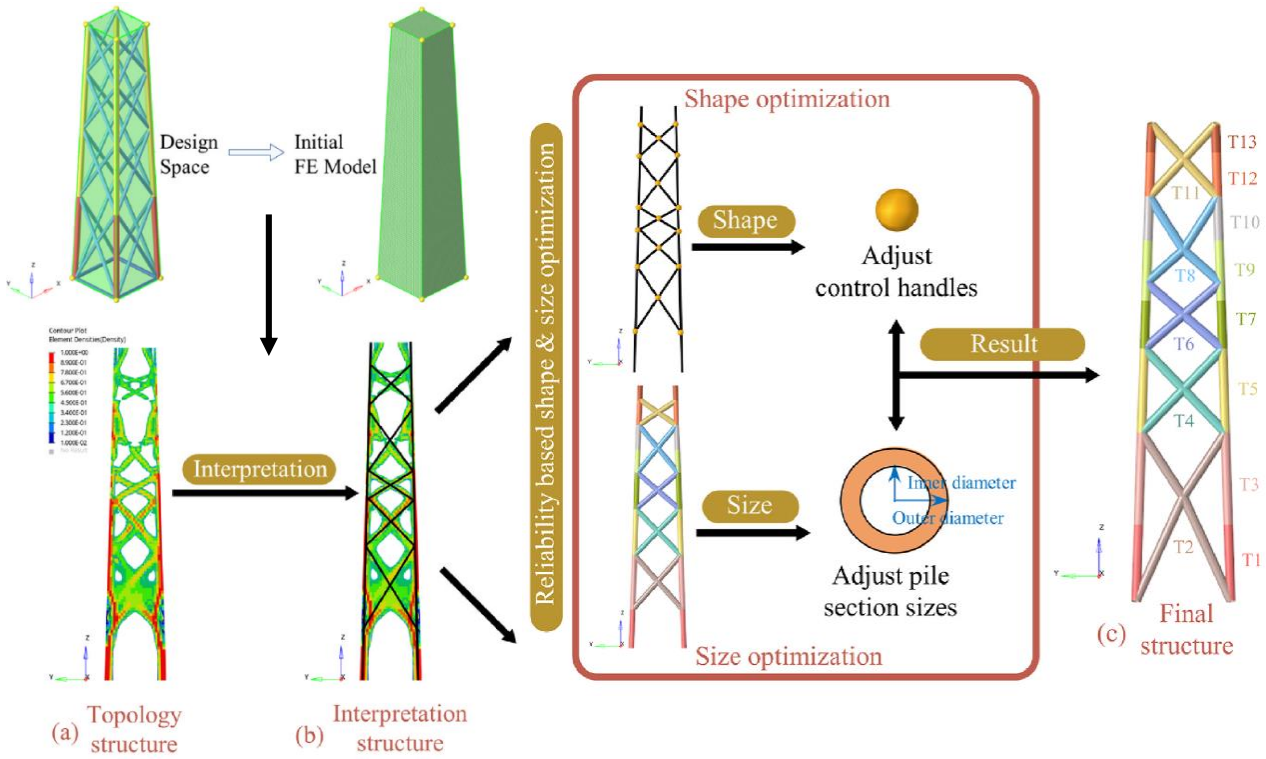

Figure 3.5. Combined topology, size and shape optimization approach for the design of a marine wind turbine supporting structure [28]

3.2 CMs' design through TO: main methods overview

In contrast to the conventional optimization's issue of creating the most rigid structure possible, the design problem, dealing with TO of compliant mechanisms, involves finding a balance between flexibility and stiffness.

Indeed, achieving the stiffest possible structure, i.e. the mininum compliance solution, leads to a negligible output displacement when an input load is applied. On the other hand, assuming the goal of optimization to be maximization of compliance, this will lead to the absence of material. The study of such a balance is addressed with the methods illustrated below.

The Ground Structure Approach employs a dense arrangement of truss or beam elements to discretize a design domain. This design space is broken down into sections using nodes, which are then interlinked by elements. A complete ground structure would enclose the maximum count of elements, establishing connections between every node in the system. Regardless of whether a complete ground structure or a portion of it is employed, a substantial quantity of elements is typically required trying to mimic a continuous structure. Each element's cross-sectional area is considered a design parameter. During the optimization process, as an element's cross-sectional area approaches zero or nears the lower limit of the design parameter, that specific element is eliminated. Consequently, upon convergence of the optimization procedure, certain elements from the initial full set are removed. The optimized structure is therefore defined by the undeleted elements that establish the configuration or layout. When employing beams within the design space, they can withstand both axial loads and bending moments. Indeed, the connections at joints are typically assumed to be rigid at both ends, allowing the transfer of bending moments throughout each beam. In this way, ground structure method provides a more accurate representation of CM’s deformation. In order to clarify this method, a practical example is illustrated in Figure 3.6 related to the optimization of

a compliant pliers mechanism [16] where the objective is to obtain the Δ output displacement by imposing the input force F. Once imposed the boundary conditions and the initial design domain with a dense truss network, the method shows the optimized structure in grayscale (Fig.3.6d) where the darkest elements are the ones to be selected. Despite the output displacement is reached, there's also a certain amount of undesired output displacement in horizontal. Furthermore, a possible drawback is the risk of creation of overlapping geometries, which can be considered as sliding joints

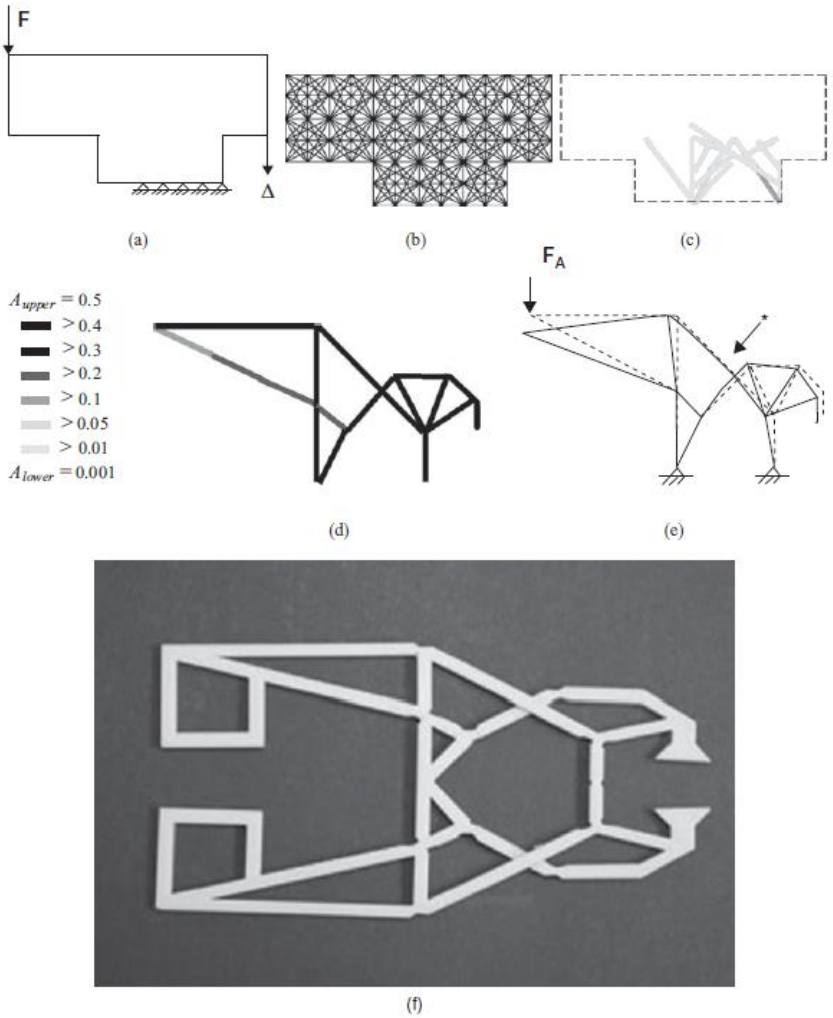

Figure 3.6. Topology optimization of compliant pliers through Ground Structure Approach: design domain and boundary conditions (a), representation of ground structure model (b), initial phases of solution (c), optimized layout and deformed shape (d,e), 3D printed prototype by FDM (f) [16]

but on the other hand represent a further critical issue especially on manufacturing planar mechanisms. A simple expedient to overcome this problem is employing a reduced ground structure (Figure 3.7) where elements do not overlap among themselves [29].

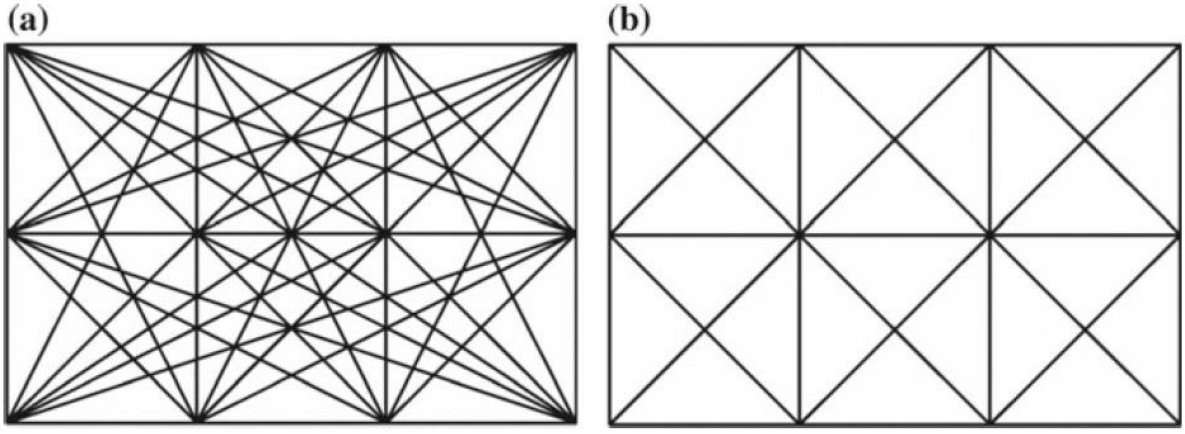

Figure 3.7. Fully connected and reduced Ground Structure optimization approach [29]

Differently from Ground Structure Approach, in the continuum approaches following introduced the design domain is typically divided into quadrilateral regions of space, so that the real structure behaviour can be closely simulated by employing a highly refined mesh. In these approaches, the design variable is usually coincident with a determined material's property, which is differently assigned to each meshed element. In this way, the different material properties of each element are exploited to decide whether an element should be removed or maintained during optimization process. Among the first continuum approaches for CMs optimization, the Homogeneization Mehod has been initially employed for minimization of compliance [30] and subsequently to CMs. This method simplifies intricate structural topology optimization issues into size optimization problems by introducing a material density function on the elements. Within the design

domain, each element is made by a unit cell defined through the variables μ, γ, θ (Figure 3.8), being the last one the angular orientation of the cell. The extreme possible values between which μ and γ can continuously range are from 0 to 1, where 1 refers to a completely filled cell while 0 indicates an empty cell. All the intermediate values of these parameters suggest a porous cell. Commonly the orientation θ assumes the same direction of the principal stresses. Based on the optimal values of these parameters, a density function is established for the structure, defining the optimal layout. Since this method requires more intricate computations compared to the following explained continuum optimization methods, it's more difficult to find practical applications. Moreover, homogeneization method often provides a structure with many intermediate densities and therefore less sharply defines an optimized layout than other techniques.

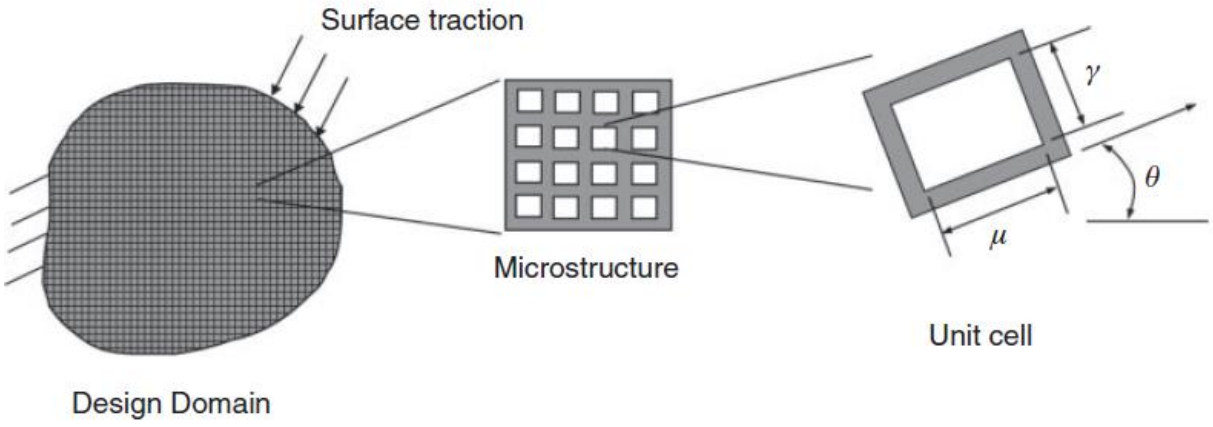

Figure 3.8. Design domain of Homogeneization method and details of the three geometrical parameters used to control the overall CM's layout [16]

Solid Isotropic Material with Penalization (SIMP) is one of the most exploited optimization methods for CMs and also the most implemented on commercial software owing to its computational efficiency and

straightforward conceptual framework. The design variables are represented by the relative densities x^e of each element, which are exploited to calculate the density ρ_e of each element through the following relation:

$$\rho_e = x^e \rho_0$$

$$0 < x^e_{min} \leq x^e \leq 1$$

The value ρ_0 is referred to the density of the selected base material. The relative density can range from a maximum value of 1 to a minimum value of x^e_{min}, which indicate respectively a full element and an empty element. The reason for setting x^e_{min} sufficiently near to zero is to prevent the model from reaching singularities in the stiffness matrix. When an element has an intermediate density can be interpreted both as full or empty, but this creates uncertainties on the structure definition. A penalty factor p is therefore used to overcome this problem, introducing it in the calculation of the element stiffness k^e. Considering k^0 the stiffness matrix of an element made up of a base material, the element stiffness is calculated as follows:

$$k^e = (x^e)^p \, k^0$$

The penalty factor p has values major than 1 and usually it used $p \geq 3$. A variety of mathematical methods has been developed to implement the SIMP optimization, such as sequential linear programming [32], sequential convex programming [33], optimality criteria [34] or the method of moving asymptotes [35]. Dealing with continuum topology optimization, some common concerns are related to avoid numerical instabilities. One of them is the mesh dependency of the model, since has been observed that different sizes of initial mesh could carry out different optimized layout. In a different

way, some checkerboard patterns issues could rise, showing a resulting geometry made up of empty and full spaces very close to each other. A representation of these numerical instabilities is reported below, toghether with a solution using a design domain with a more refined mesh [36].

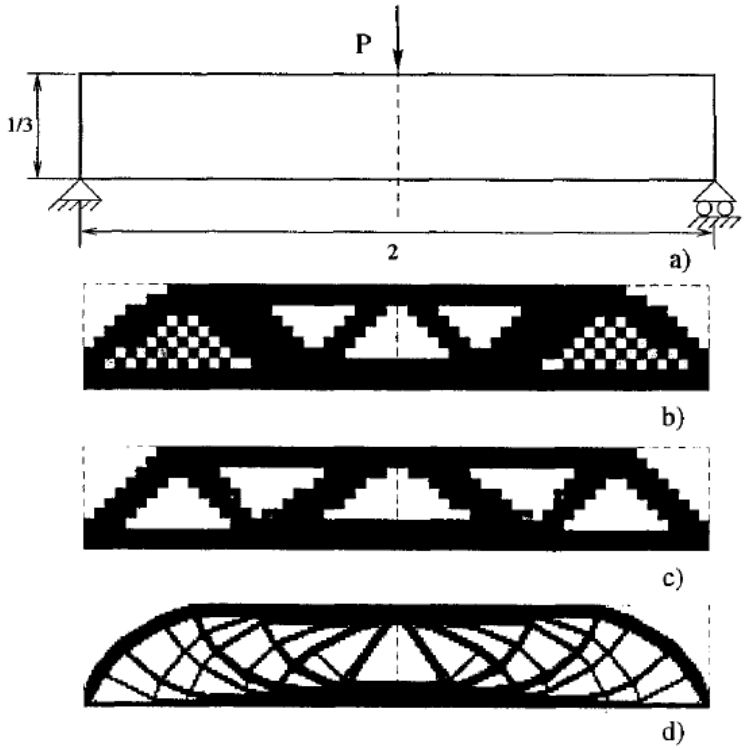

Figure 3.9. Simple case study (a) showing both checkerboard issues (b,c) and effects of mesh refinement on the solution (d) [36]

To overcome these numerical intabilities so that TO could be able to provide manfacturable layouts, the use of morphology centered constraints methods operating as density filters has proven to be effective [37]. This filtering method considers in a different way the mechanical strenght of an element, by relating it to a function derived from the neighboring elements' design variables. The gradual transition between solid and void areas, leading to uncertainties on defining the optimized shape, is in this way softened, providing a more net shaped layout, as displayed below in Figure 3.10.

Figure 3.10. Optimized CM inverter (left) and two different filters applied: density filter with linearly decaying weighting (center) and bi-lateral density filter (right) [37]

Moreover, these categories of filtering demand minimal CPU time and are also simple to use, not requiring additional constraints to be modeled.

Considering the optimization problem in SIMP method, the objective function is referred to the geometric advantage, i.e. the ratio of output and input displacements. With F_{in}, u_{in} and u_{out} are respectively defined the input force, the input displacement and the output displacement while k_{in} and k_{out} represent the input stiffness of an hypotetical actuator and of the workpiece. Applying the TO to Compliant Mechanisms design is therefore associated to the maximization of the output displacement u_{out}, by taking into account both a material mass constraint on the total volume V and the range of possible values of element densities ρ_e, described by the following relations:

$$\max : u_{out}$$

$$Vol = \sum_{e=1}^{N} (\rho_e v_e) \leq V; \qquad v_e = volume\ of\ element\ e$$

$$0 < \rho_{min} \leq \rho_e \leq 1; \qquad e = 1, \dots, N = total\ number\ of\ elements$$

A generical simplified representation of the design domain with the abovementioned variables is represented below in Figure 3.11 within a simple displacement inverter mechanism solved through SIMP method [29].

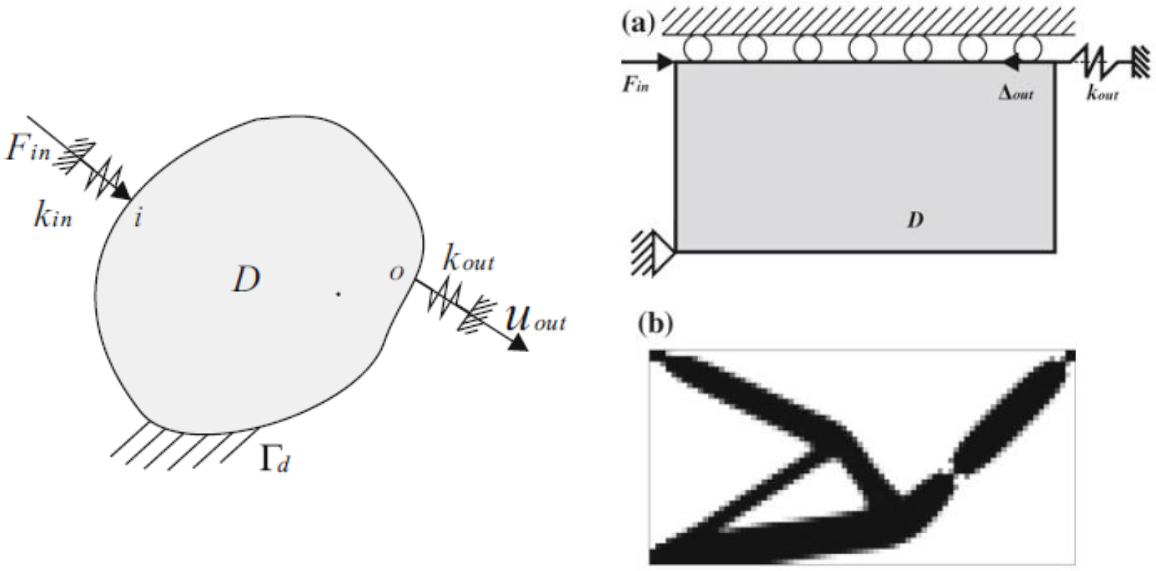

Figure 3.11. Simplified representation of generical SIMP design domain (left) and practical example of optimization setting for a displacement inverter and final layout [29]

The resulting layout shows a small area with a very small thickness whose task is similar to the one of a revolute joint. This particular shape is commonly known as de facto hinge, and represents a significant issue in TO since the small area affected could undergo to high stresses concentration, leading to challenging manufacturing processes and moreover to the impossibility of miniaturization. Nevertheless a robust formulation has been proposed by Sigmund et al [38] to provide optimized designs not depending on manufacturing constraints, preventing the formation of elements connected through only one node. Evolutionary Structural Optimization (ESO) is another widespread TO approach, conceived from the fundamental concept of progressively eliminating ineffective material within a structure to achieve its optimized shape. Basically, this method is inspired by the concept of a full stressed design. According to this ideal design, the stress levels in various points of an optimal structure tend to hover around a similar safe threeshold. In a structure owning a similar stress map, a criterion for

removing material can be established, considering that any material experiencing low stress becomes inefficient and consequently his presence within the structure itself can be avoided. As happens with the SIMP method, the design domain is initially segmented into numerous small elements, facilitating a progressive material removal. The stress within each element can be assessed through various methods, however the Von Mises stress is the most widely used. The Von Mises stress for a plane stress model is described as follows:

$$\sigma_v = \sqrt{\sigma_x^2 - \sigma_x \sigma_y + \sigma_y^2 + 3\tau_{xy}^2}\ ;$$

$$\sigma_x, \sigma_y = normal\ stresses; \qquad \tau_{xy} = shear\ stress;$$

In finalizing the optimization process, a crucial aspect is determining when an element should be removed. In ESO the Von Mises stress of an element σ_v^e is compared to the maximum stress of the structure σ_v^M, consequently the element is removed according to the following relation:

$$\frac{\sigma_v^e}{\sigma_v^M} \leq RR_i$$

Considering RR_i the rejection ratio of the iteration i, for each cycle of FEA an amount of elements is removed. When the number of deleted elements begins to decrease, the optimization process is reaching a stazionary state, therefore an evolutionary rate ER is added to RRi which remains constant until a new stationary state is reached.

$$RR_{i+1} = ER + RR_i$$

These last parameters are the only that need to be set for optimization and in most applications it's suggested to use 1% for both [39]. An advancement of this method is the Bidirectional ESO (BESO), which introduces the capability to both add and remove the elements, enabling also a better research of a global optimum solution. The condition on which it depends whether an element should be added or not is based also in this case upon a comparison of the element's Von Mises stress with the maximum stress of the structure.Therefore once verified the following relation an element can be added:

$$\frac{\sigma_v^e}{\sigma_v^M} \leq IR_i\,; \qquad IR_i = inclusion\,ratio;$$

Although this method is well developed finding application in general mechanical structures, microstructures of cellular materials or composites and frequency optimization, it results less commonly used for CMs' design in comparison with SIMP method. Homogeneization, SIMP and ESO methods prove therefore to be effective in CMs design, moreover providing different results of the same application (Figure 3.12)[31], it could be useful trying to compare their final optimized layout assessing the performance's differences, depending on the design's requirements.

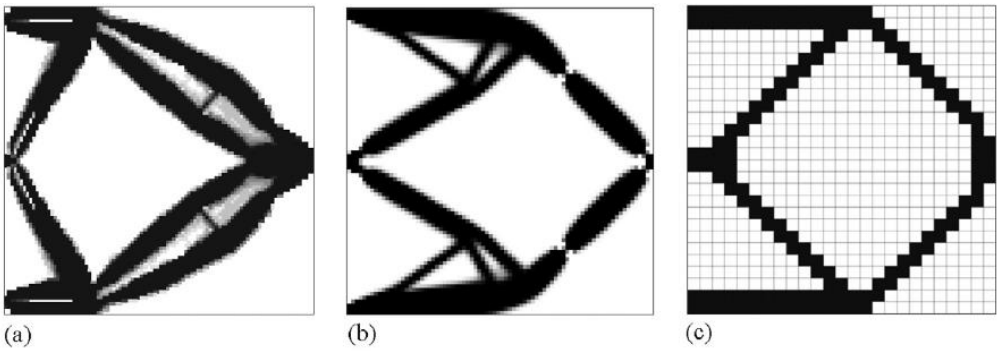

Figure 3.12. Comparison of TO applied to a simple displacement inverter using three different methods: Homgeneization (a), SIMP (b) and ESO (c) [31]

4. Bio-Inspired Designs: Flapping Wing Micro Air Vehicles

The application of clever natural designs has attracted considerable interest in engineering fields, especially concerning mechanisms and vehicles. Taking cues from living systems like organisms and ecosystems has sparked numerous groundbreaking advancements, presenting numerous benefits that transform conventional engineering approaches. By mimicking biological principles in crafting mechanisms and vehicles, it not only delivers unmatched effectiveness but also proves to be beneficial considering adaptability and sustainability of engineering solutions. Indeed, taking inspiration from natural structures for reducing weight, material consumption, or just simplifying a product reducing its number of components, could improve for example the overall carbon footprint related both to the manufacturing process and to the lifecycle of the product.

If we think about one of the most popular bio-inspired design such as Leonardo Da Vinci's concept for a glider (Figure 4.1a) [69] the resemblance of his device to a bird's wing makes it clear of how his delving into living beings'morfology was significant even in those days to develop a novel design. Drewing inspiration from the interaction between cocklebur and his dog's fur, in 1951 the swiss engineer George de Mestral has patented the Velcro, observing the hook-shaped spikes of cocklebur [70] able to grasp onto dog's hair (Figure 4.1b). Such technology is still industrially employed and improved over the years, as can be seen for instance considering the

3M™ Dual Lock™ (Figure 4.1c)[71]. Likewise, the consolidated and widespread usage of radar and sonar systems has been supported from the exploration of bats' echolocation ability, which continuously allows to capture echoes variations in amplitude and frequency (Figure 4.1d) identifying physical objects' positioning [72,73].

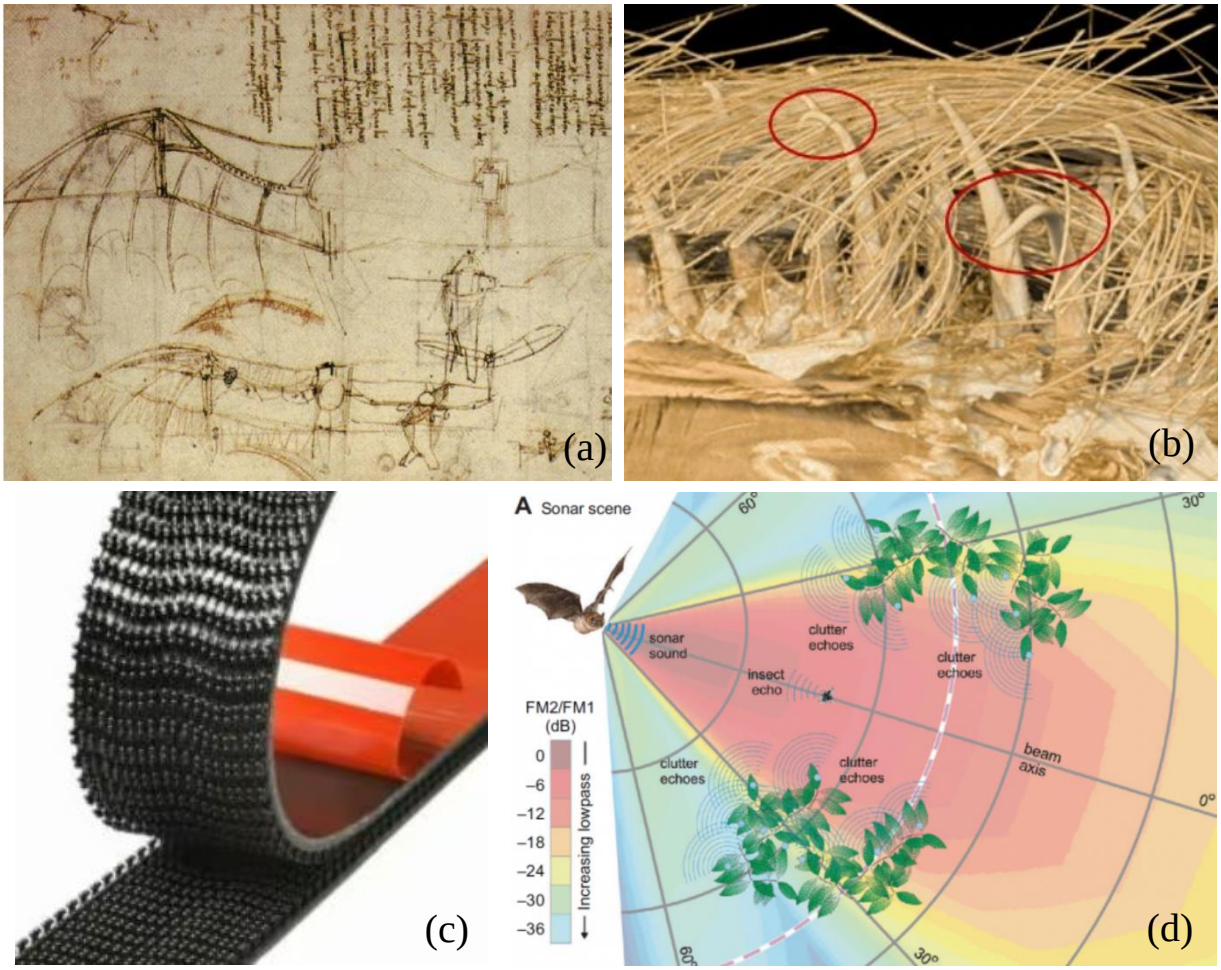

Figure 4.1. Leonardo Da Vinci's concept for a glider (a), hook-shaped spikes of cocklebur (b), 3M™ Dual Lock™ (c), schematization of bats'sonar system for echolocation (d).

In order to make a design process suitable to succesfully exploit advices coming from nature, it would be greatly useful taking advantage from an overview of biological features, properly classified. A similar approach has been recently proposed known as Expandable Domain Integrated Design

(xDID) [40]: this method is able to create precise geometric classification termed as domains, organized considering biological traits based on their distinct characteristics, extracted from a range of examples of bio-inspired designs (Figure 4.2).

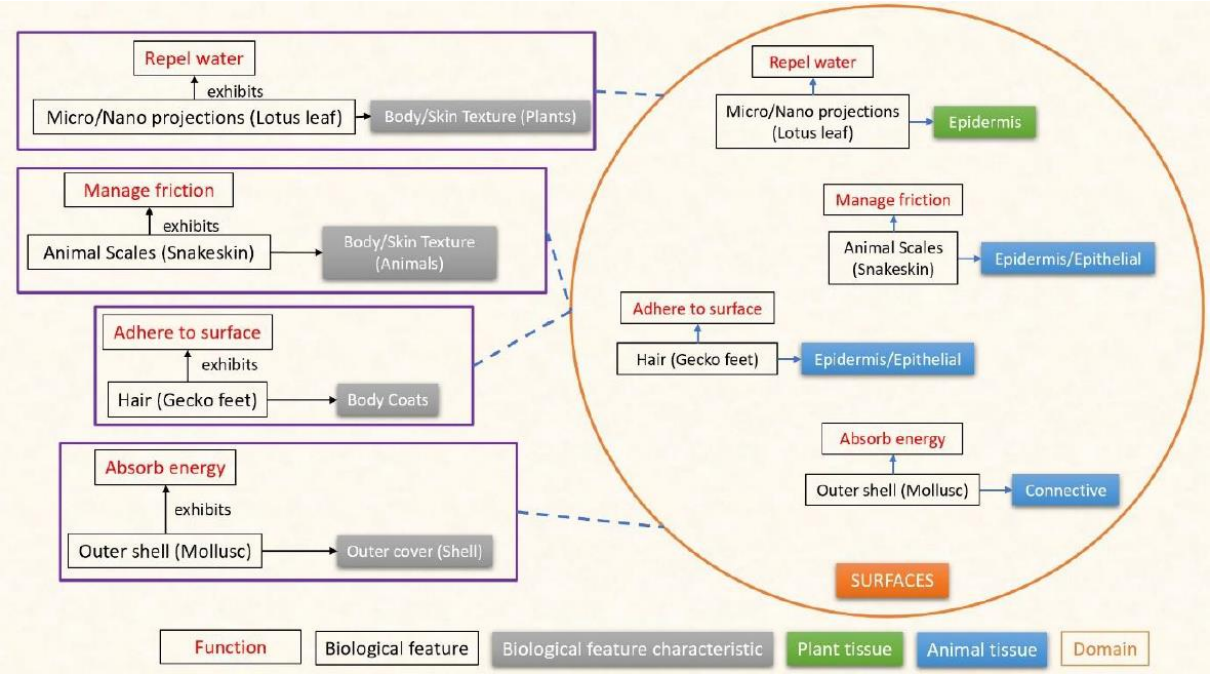

Figure 4.2. Example of a map extracted through the Expandable Domain Integrated Design technique (xDID) assembled considering many properties useful for a specific project requirement [40]

These categorized biological features are then correlated with corresponding plant and animal tissues from their origins. Throughout the design of an innovative product, the availability of these classified domains containing surfaces, shapes, cross-sections and cellular structures, proves to be extremely effective since combining several biological traits, coming from different living beings, leads to the development of exclusive multifunctional design concepts. Three significant applications of xDID bio-inspired designs are resumed below in Figure 4.3. The first case concerns the development of painless sutures achieved by combining the cross-

section of a kingfisher's beak and the barbs on porcupine quills. In the second design, involving a concept of a gas turbine for engine applications, were combined the camel's turbinate properties of high heat transfer and low pressure drop with the capability of water absorption from fog owned by a desert beetle.

(a)

(b

(c)

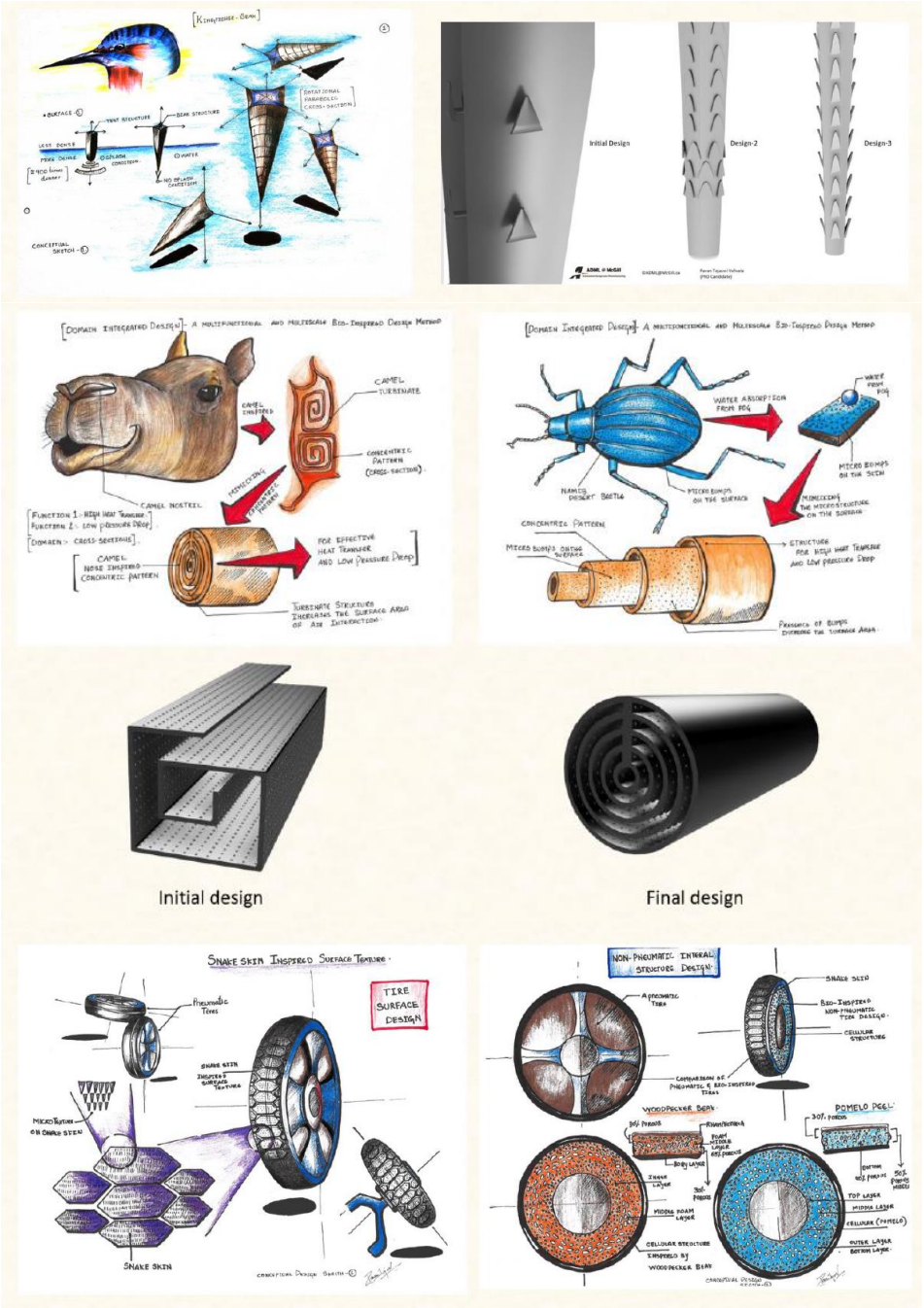

Figure 4.3. Multifunctional bio-inspired designs achieved with xDID [40]

Similarly, a the multifunctional non-pneumatic tire was conceptualized exploiting both the snakeskin scales, able to manage variable friction, the woodpecker's beak foam and the pomelo peel, useful for impact absorption features [40]. Among all the bio-inspired designs object of research, it can also be found in several recent applications in the field of robotics the growing tendency of exploiting the possibility of creating innovative structures taking advantage both of the increasingly in-depth knowledge on living organisms and of technological progresses. Indeed, the wide availability recently gained by Unmanned Air Vehicles (UAVs), previously confined predominantly to military applications, withnesses their great development. These vehicles, able to operate without a human pilot through remote piloting or autonomously, find nowadays regularly applications for aerial photography, urban planning, security purposes in identifying people in crowded places, for packages or urgent medical transports, in industrial risky environments or public facilities to detect potential dangers and so on. The UAVs can be categorized in three main groups based in their lift generation: fixed wing, rotary wing and flapping wing vehicles. Fixed wing vehicles needs to move forward above a certain minimum speed, using one

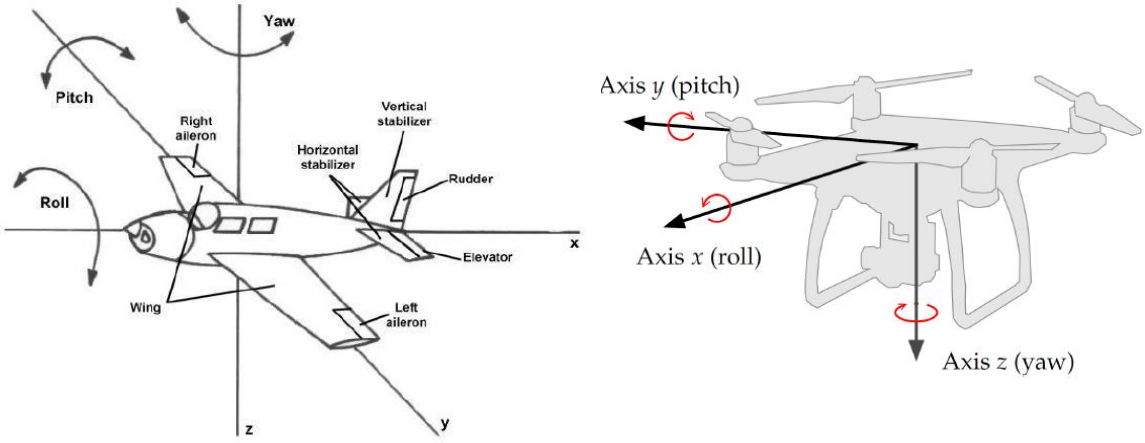

Figure 4.4. Simplified representation of fixed wing [41] and rotary wing vehicles [42]

or more propellers, in order to create sufficient lift under the wings and are mainly used outdoor. Rotary wing vehicles create the sufficient lift using more rotating bladed propellers, whose simultaneous operation needs to be properly coordinated through on-board electronics. These vehicles have the advantage to be able to perform vertical take-off, feature that makes them particularly suitable for indoor or in confined spaces flight. Flapping wing vehicles have been developed by taking inspiration from the flight of insects and birds, which exhibit improved performance, acrobatic abilities and extended flight times compared to the artificially created fixed and rotary wing vehicles. Consequently, the aspiration to attain these exceptional flight characteristics motivates active research in the field of flapping flight.

Considering for example that the flight efficiency of flapping vehicles, among other various factors, can be attributed to the power loading, which measures the ratio between thrust and input power and it's also used for rotary wing drones. Comparing this value for flapping and rotary wing

	Power Loading	
	lb/hp	gf/W
Hawkmoth	70	42,6
Micro rotor 1	30	18,2
Orchid bee	50	30,4
Micro rotor 2	20	12,2
Phantom 2	6,6	4
KUBeetle-S	8,2	5
Dragonfly	40	24,3
Delfy Nimble	8,2	5

Figure 4.5. Comparison of power loadings for flapping and rotary wing vehicles [44]

vehicles, the former proves to have higher power loading [43] as can be seen also from figure 4.5 where is reported a table with power loadings compared for both robotic insects and micro-rotors vehicles [44].

An insect's wing movement involves a sequence of actions: a downstroke motion followed by an upstroke, each divided by two rotational phases known as pronation and supination, which are respectively referred to the rotation of the wing's surface downwards and upwards. This rotational action ensures that during every shift in the stroke, the foremost part of the wing, known as leading edge, remains at the front. Researchers have detected five fundamental aerodynamic mechanisms that characterize the use of wings to generate aerodynamic forces: added mass, absence of stall, rotational circulation, clap and fling and wing–wake interactions [45][46].

During wing's acceleration and deceleration, the surrounding air generates a pressure on wing's surface that could be mathematically described as a time-varying growth in the wing's inertia (added mass effect), especially when wing's motion is reverted. The leading edge vortex (LEV) which forms at high angle of attack (i.e. the angle created by the wing chord and the incoming flow velocity) does not separate from the wing, as happens with a fixed wing translating at high angles of attack creating the stall phenomenon. Instead, the flow behind the vortex reattaches to the wing not allowin the stall, and moreover increases lift especially in the middle of downstroke and upstroke. The air circulating around the wings is exploited to increase the lift by rotating the wing before the stroke reversal. In the same instant, the wings get together and this clapping phenomenon also results in an improvement of lift. Another beneficial aerodynamic effect is related to

the ability of the wing to capture the air vortices created at the end of each stroke, increasing by doing this the lift forces. A simplified representation of flapping wing's aerodynamic is provided below in Figure 4.6 [45].

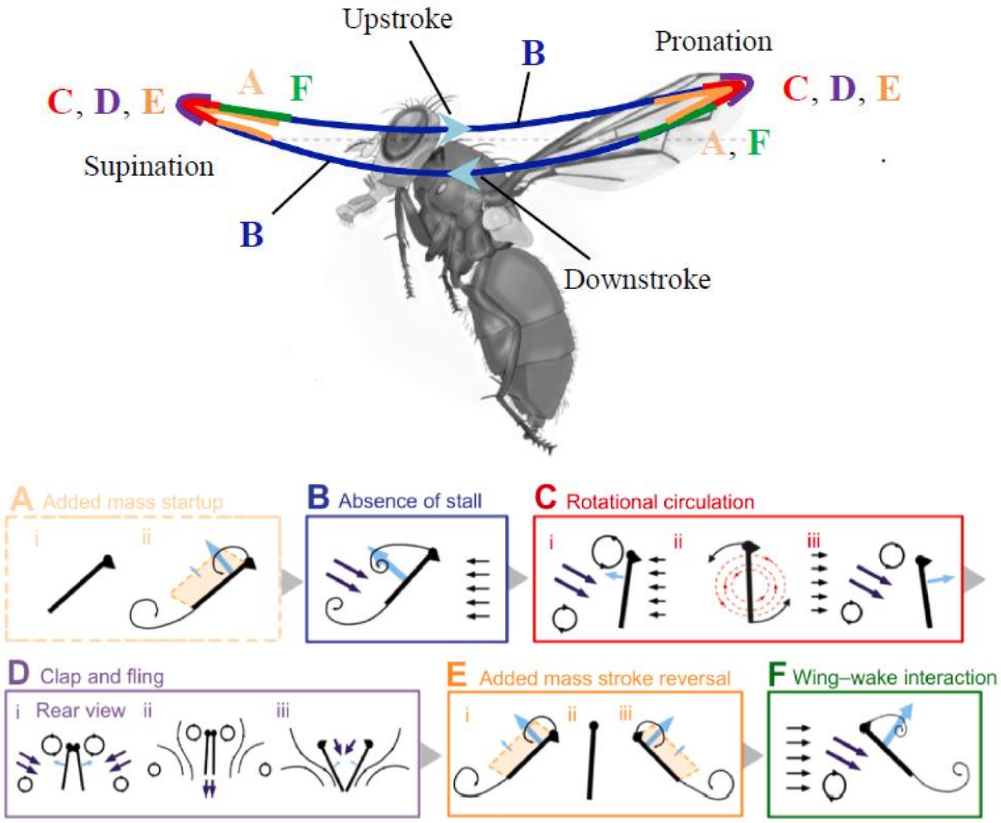

Figure 4.6. Simplified aerodynamic force mechanisms in insects'flight and schematized wing path during upstroke and downstroke [45]

Although a great diversity of insects' structures exists, each one having a particular shape, these aerodynamic effects are approximately the same for flapping wing insects. The increasing in-depth study of these flying mechanisms led to the development of various insect-inspired vehicles. In addition to their higher flight efficiency, flapping vehicles result more safer to be used among people since their operating frequencies are lower than rotary wing drones. Besides, due to their insects'mimicking capability, a possible deployment for security or military purposes becomes possible.

Observing insects's morphology, three main configurations can be defined, categorized on the basis of their wings, reported below in Figure 4.7.

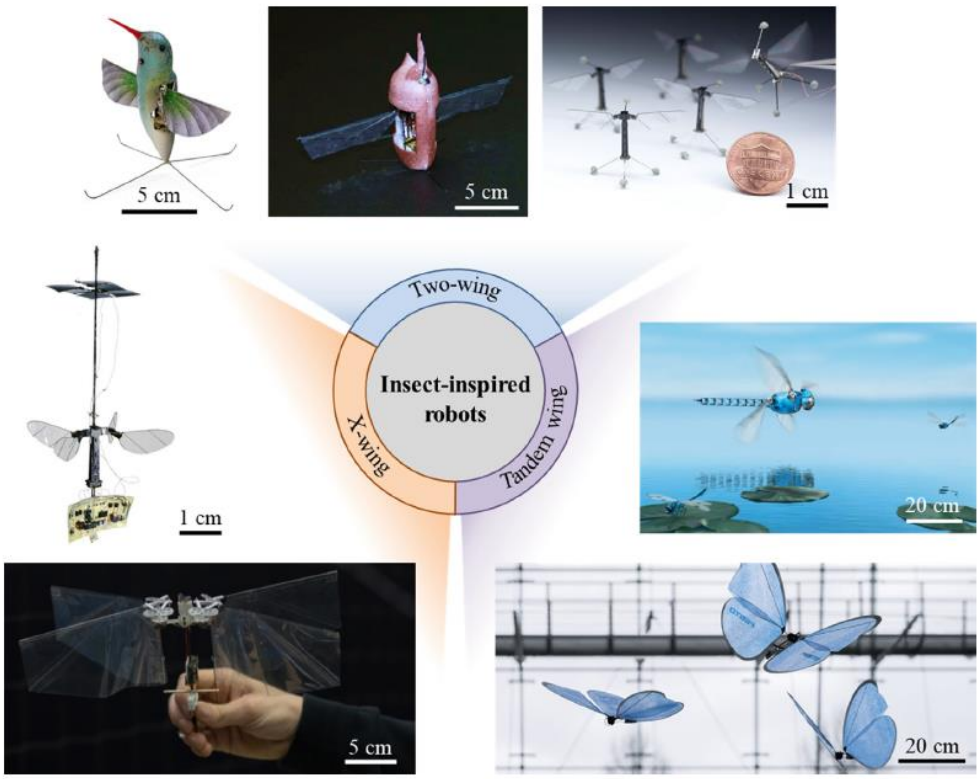

Figure 4.7. Different insect-inspired robots categoryzed through their wings' configuration, and details on vehicles'wingspan [44]

For each one is also described the target dimension of the prototype, ranging from 1 cm to 20 cm of wingspan. Compared to bird-inspired robots, which necessarily have larger dimensions, Flapping Wing Micro Air Vehicles exhibit some design challenges, some of them can be summarized below:

- Smaller dimensions, which necessitates of highly performing internal structures in order to provide motion and support electric and electronic devices;
- Large flapping frequencies, resulting in highly varying inertia caused by the added mass startup aerodynamic phenomoenon;

- Wider flapping amplitude, needed to maintain the distinctive and beneficial effect of the Leading Edge Vortex, whish results in actuation mechanisms capable of high frequency large displacements;

Combining all the required items to make the FWMAV able to fly withouth loosing compactness is also an essential point to be attentioned. To provide a generic vehicle arrangement suitable to represent the majority of FWMAVs designed so far, the x-wing NUS-Roboticbird [47] is depicted below in Figure 4.8. In this case, two brushless motors have been selected to actuate the propulsion mechanism, composed by a crank, slider and rocket rigid body mechanism. The battery, accounting for 20% of the total weight, is conveniently positioned in the lower part of the frame in such a way that the center of gravity is located in a beneficial way during the flapping maneuvers. Two servo motors, each one located near the wings, are essential to perform yaw, pitch and roll motions by independentely modulating the stroke planes of the two pair of wings. Since this vehicle in particular is able both to fly and carry out yaw, pitch

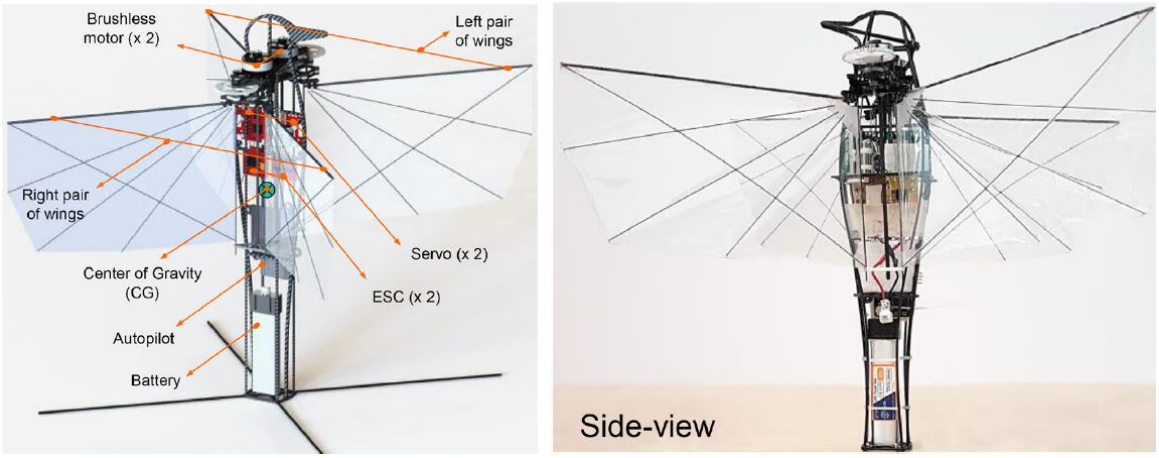

Figure 4.8. Detail of components generally required in a FWMAV, in this case a 3d cad model of the x-wing NUS-Roboticbird (left) and a flying prototype (right)[47].

and roll motions by simply regulating the flapping parameters, two electronic speed controllers have a fudamental role in coordinating all the electronic devices. Three main sources of energy are broadly used to operate the internal mechanisms able to create the reciprocating flapping motion of wings: DC motors, piezoelectric actuators and electromagnetic actuators. The first are the most diffused due to their reliability and availability, presenting practical advantages such as high power density and easiness on control. On the other hand DC actuators have the drawback of high energy consumption and low efficiency [48]. Piezoelectric actuators show fast response speed and high efficiency in energy conversion but they require high driving voltage in order to correctly operate. Electromagnetic actuators otherwise present low operating voltages and power but are hardly available as off the shelf components, instead they are mainly customized and tailored on the basis of the specific requirement. Insects and birds have dissimilarities in their anatomy, indeed in insects is notable the absence of a control surface comparable to a bird's tail. Consequently, insects need to actively adjust their wing movements during flapping flight to generate control forces or moments alongside the force propelling their flight. As a result, creating an aerial vehicle resembling an insect without a tail represents a significant engineering challenge, which necessitates the comprehensive application and implementation of the control principles observed in insect flight. Inspired by the observation of insect’s structures and flight controls, many approaches have been developed in FWMAVs to generate yaw, pitch and roll maneuvers, some examples of these control

techniques are depicted in Figure 4.9 [45]. In Figure 4.10 instead are better shown the axis around which the control motions occur [49], being Z the vertical axis. To perform these maneuvers, both the flapping planes and the flapping frequencies are adjusted, sometimes in a differentiated way for each wing, in order to reach an asymmetry in motion, therefore resulting in different aerodynamic effects and flapping motions.

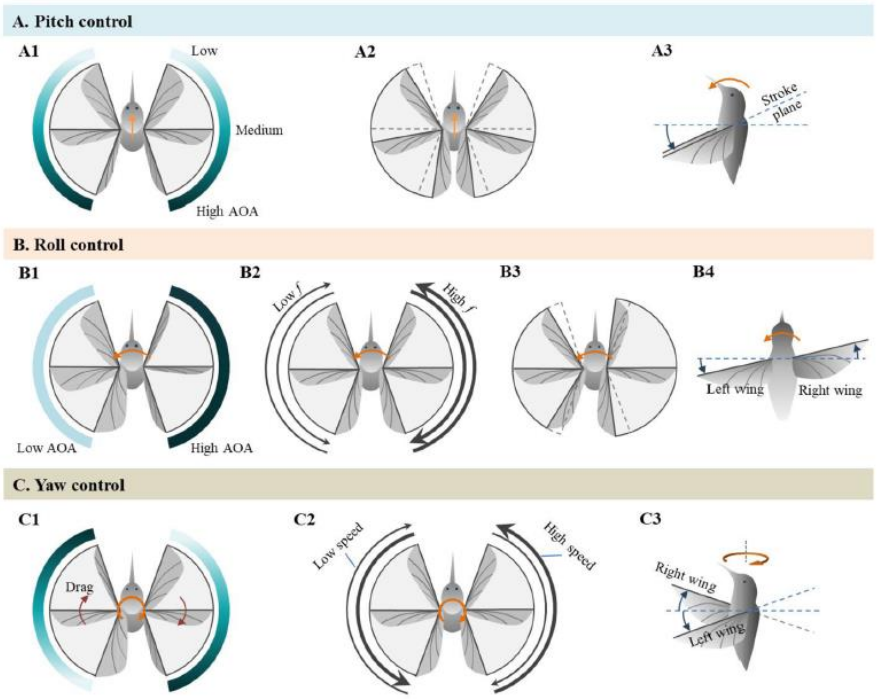

Figure 4.9. Examples of yaw, pitch and roll control methods in tailless FWMAVs [45].

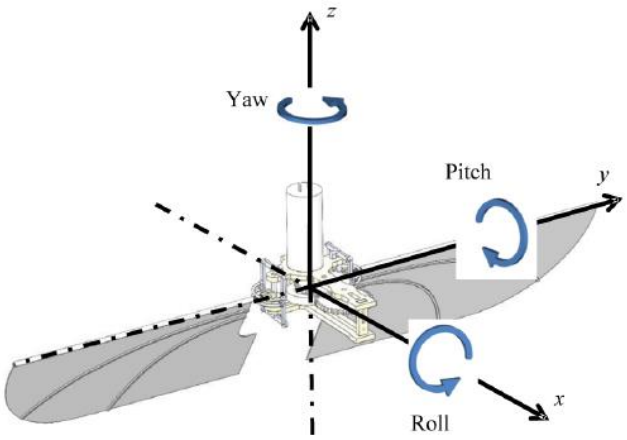

Figure 4.10. Schematic representation of yaw, pitch and roll axis in FWMAVs [49].

5. Additive Manufacturing Technologies: Fused Deposition Modeling

The spreading of additive manufacturing technologies over since 1980s allowed both the development of new specific application areas and also enabled the re-engineering of existing products. Compared to the traditional subtractive manufacturing processes, AM presents strenghts and weaknesses, some of them regarding to:

- Production time: subtractive technologies might exhibit higher speed in certain instances due to its capacity of removing materials in larger quantities compared to the incremental, layer-based approach utilized in additive manufacturing.
- Desing complexity: additive manufacturing provides increased liberty and intricacy in design without notably impacting production expenses. In contrast, subtractive methods face constraints in creating intricate designs due to limitations posed by tools and machining capabilities.
- Material usage and waste: AM typically demonstrates a higher efficiency in material usage by adding material solely where needed, resulting in reduced waste. Conversely, subtractive manufacturing leads to increased waste production through the removal of surplus material.

According to the ISO/ASTM 52900:2021, the international standard establishing terms used in Additive Manufacturing technologies, seven categories of AM processes can be distinguished [68]:

- Binder Jetting (BJT): in this process a liquid bonding agent is selectively deposited to join powder materials;
- Directed Energy Deposition (DED): a thermal energy source is used to fuse materials by melting them as they are being deposited;
- Material Extrusion (MEX): a nozzle or orifice is used to selectively dispense the material to be extruded, progressively creating the part;
- Material Jetting (MJT): this technology uses droplets of feedstock material which are selectively deposited;
- Powder Bed Fusion (PBF): the parts are made by selectively fusing regions of a powder bed using a thermal energy source;
- Sheet Lamination (SHL): sheets of material are progressively bonded to form the desired part;
- Vat Photopolymerization (VPP): a liquid photopolymer contained in a vat is selectively cured by light-activated polymerization;

Although a great variety of AM processes has been progressively developed to avoid printing defects and to improve the products' resolution and mechanical properties [50], it's useful to describe four widespread processes resuming their main features.

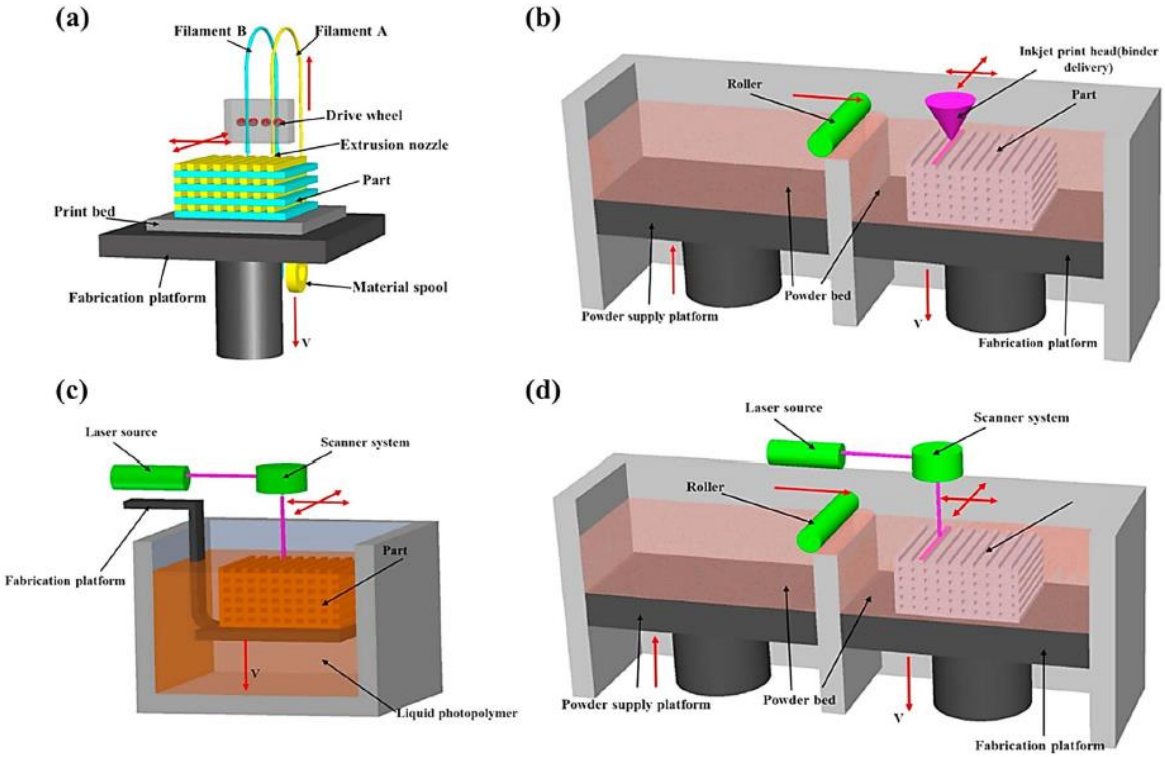

Figure 5.1. Overview of four widespread Additive Manufacturing processes: fused deposition modeling FDM (a), inkjet printing (b), stereolithography (c), selective laser melting (d) [50].

Through inkjet printing, which is a BJT process, the material is pumped inside a nozzle and deposited on the substrate in form of droplets which solidify once adherent to a colder platform or another substrate. This method is especially used to create complex ceramics scaffold for tissue engineering. Stereolithography is among the first AM processes, and it's based on progressive UV polymerization of layers inside a resin or monomer solution. Although the slowness of process and the limited choice of materials, through this VPP technology an high resolution up to 10 micrometers can be achieved. The selective laser melting technology (a PBF process) implies the melting of the material, in form of atomized metal powder, through a laser beam. Once a layer is completed, a roller spreads new powder above the previous layer so as to melt them together.

The high duration and costs required for this process are balanced by excellent resolution and material performance, which make it suitable to biomedical, aerospace and electronics applications. Fused deposition modeling, belonging to the Material Extrusion category, involves the heating of a continuous filament of thermoplastic polymer which is extruded on a platform layer-by-layer gradually defining the product.

The most influential process parameters to be adjusted are the layer thickness, the platform and the nozzle temperatures and the material flow speed. Reaching an optimal adherence between layers is essential to obtain the highest possible material properties, since inter-layer distortion has been identified as the primary reason of mechanical weaknesses.

Simultaneously with parameters'choice, a careful 3D modeling of product and his supports is required, avoiding problems related to insufficient stability between layers, surfaces with too high angles resulting in staircase effects, or poor final mechanical properties due to an unsuitable infill pattern. The wide availability of FDM 3D printers lead to a general good knowledge of process parameters'correct choice to reach a sufficient printing quality. Nevertheless, a recent research trend is focused on further improving the FDM parts'quality by exploiting the machine learning algorithms [51].

In such a way have been indeed experienced FDM quality enhancements concerning the prediction of surface roughness, geometric deviations, energy estimation and defect detection.

CMs'manufacturing particularly take advantage from the geometrical freedom allowed by FDM together with the diffusion of a great range of materials, which despite being low-cost, ensure good mechanical properties and surface quality. FDM's applicability to the most challenging CMs' design is witnessed for instance by the realization of an high-performance fiber reinforced compliant nanopositioner [52].

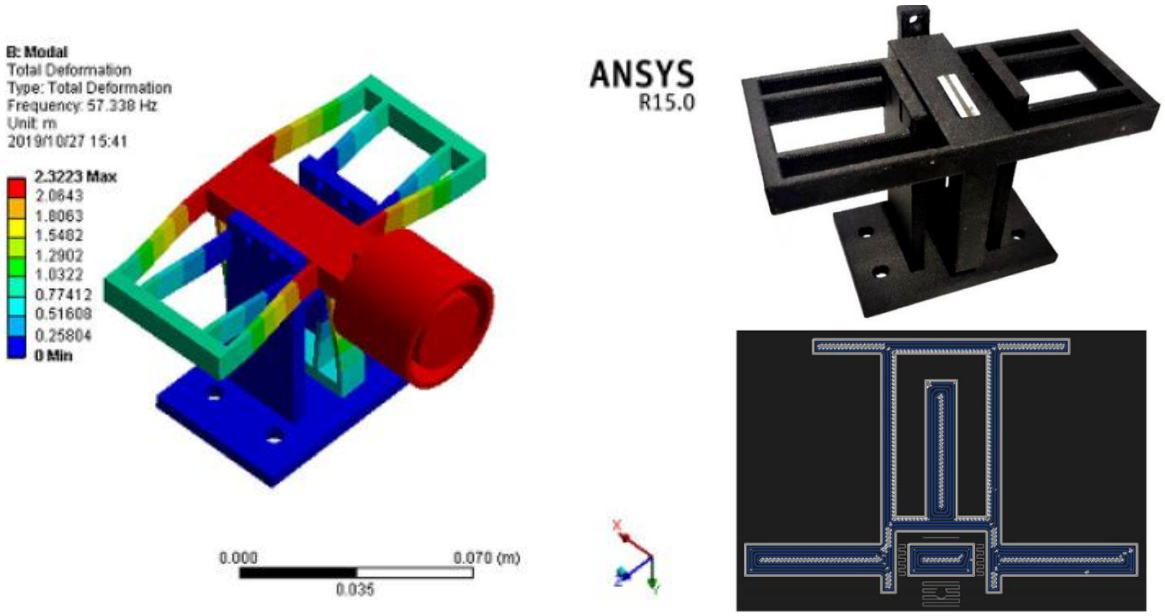

Figure 5.2. FEA model of a compliant nanopositioner (left) and the FDM prototype realized with a differentiated layout, containing inner carbon fibers and external onyx material (right) [52].

In this research a CM with a mixed structure of Carbon Fiber Reinforced Polymer (CFRP) is implemented using carbon onyx and carbon fibers, which are properly oriented to provide the desired mechanical performances (Figure 5.2). Another remarkable aspect for exploiting FDM in CMs'development is the capability of printing with materials suitable to store large amount of elastic energy. This advantage for instance is considered in realizing bio-inspired compliant spiral springs, useful for soft robotic, medical or industrial applications [53].

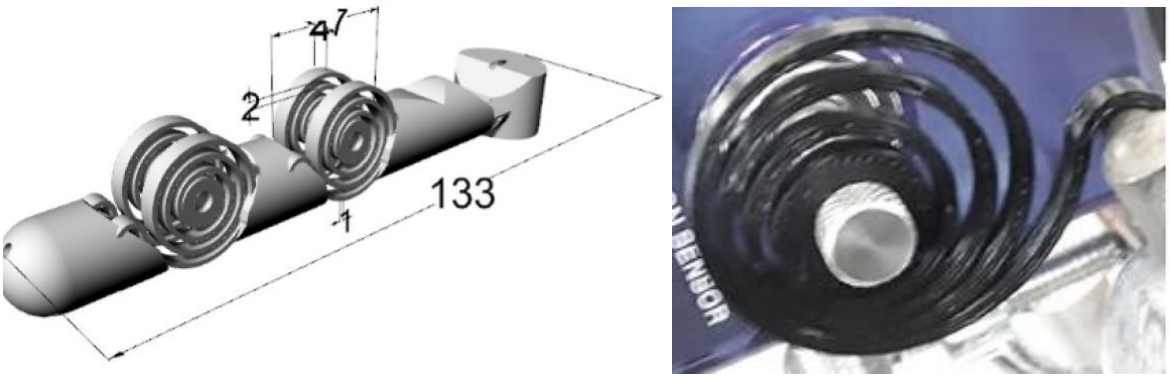

Figure 5.3. Bio-inspired compliant spiral springs realized with FDM in ABS and Nylon materials, and employed in a tendon actuated 3D-printed finger [53].

These highly customizable compliant springs, in addition to providing elastic energy storage within a small volume and also having a light weight, prove to be beneficial to avoid undesirable vibration or preventing buckling phenomenons. Although both FDM materials used in this applicarion (ABS and nylon) allow the operation of compliant spring, the highest output displacement has been reached with nylon, whose elastic modulus is half of ABS. This suggests that depending on the amount of required displacement, more flexible materials are preferable to develop large deflection compliant mechanisms. On the other hand, if the CM undergoes to a medium displacement range, then also materials having lower stiffness can be exploited.

6. Design of CMs with low frequency of deformation: wiper case study

Before starting to deal with CMs undergoing to large deflections at high motion frequency, it was considered beneficial to acquire an initial experience on design of low frequency and moderately deflected compliant mechanisms. This provided the dual advantage both of increase the insight on the mechanical behaviour of 3D printed flexible materials and to better comprehend the FEA modeling of these mechanisms. This chapter is therefore focused on the development of a novel monolithic wiper, whose layout has been definded through numerical analysis so as to exploit FDM 3d printing and compliant mechanisms. Its performances were compared with those of the wiper made in the traditional way and with those of the only other existing single-component wiper of which we have news, the one patented by the United States (US) company Flexsys, achieving good results in both in terms of weight reduction, pressure distribution at the wiper/glass interface and effectively lowering the maximum stress levels [54]. This application aims also to provide a practical illustration of re-engineering process, redesigning a product conventionally consisting of numerous components and joining elements and transforming it into a single-component 3d printable product.

6.1 Reengineering approach and definition of a novel flexible monolithic wiper

For an effective reengineering of the component, an analysis of the traditional windscreen wiper's functionality was crucial before the design phase. This analysis aimed to comprehend the fundamental aspects essential for crafting the innovative frame. The structural elements responsible for applying the required pressure to the windscreen include:

- The blade: this component serves the purpose of clearing water from the windshield. Usually is composed by a rubber internally reinforced by two curved metal vertebrae. These vertebrae aid in achieving a more uniform distribution of pressure across the surface.
- The frame: this part provides support to the blade. It comprises metal arches interconnected by hinges, serving as the structural foundation for the blade.
- The arm: typically composed of galvanized steel, this component applies the necessary force to the frame. Its role is to ensure proper adherence of the rubber blade to the windshield, enabling intermittent movement enabled by the connected electric motor.

Since the wiper must correctly adhere to the windshield, whose surface has a variable radius of curvature, the compliant wiper design process will focus on the most challenging configuration, i.e. the maximum radius of curvature. Another primary requirement is to apply pressure as uniformly as possible

across the contact surface with the windshield, essential to prevent any unwanted deviations that could result in inadequate cleaning, especially during challenging weather conditions.

The wiper taken as example for the re-engineering process is a traditional wiper whose aluminum frame features one input point and eight output points. Together with the main frame, the wiper contains two secondary arches and four smaller arches, with an overall total length of 550 mm. The only other existing single-component wiper patented by Flexsys company was analyzed as well, whose layout aimed to evenly distributing the input force from the arm across eight contact points between the frame and the blade. This frame is indeed centered on the repetition of triangular elements, used to split an input force into two output forces, ensuring more balanced force distribution across the wiper assembly.

In contrast to the conventional frame that maintains the blade in a straight position initially and then bends it by exerting force from the arm, the single-component Flexsys frame was designed with a specific initial curvature given to the blade. This initial curvature, further accentuated by the

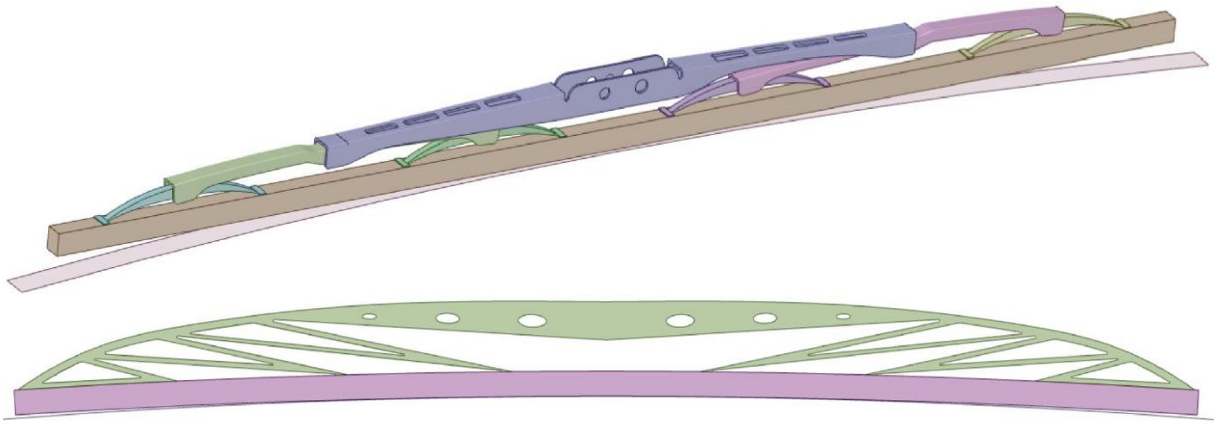

Figure 6.1. CAD models of traditional windshield wiper (above) and Flexsys single-component frame (below) [54]

application of force, enables the blade to adapt progressively to the curvature of the windscreen throughout different operational phases. This design facilitates the blade's flexibility to conform effectively to the windscreen's varying shape during its functioning. To succesfully assess the novel monolithic compliant wiper’s performance, cad 3D models of these two aforementioned wipers have been created, in order to perform a comprehensive FEM analysis of each wiper model.

After having settled the requirements to be used as target to introduce structural innovations, the choice of material was made taking into account both the opportunities of Additive Manufacturing and the capabilities of integrating Compliant Mechanisms into the wiper frame. Aiming to an overall lightening of the product, at least maintaining the performances of existing wipers, steel and aluminum materials were discarded, although being used in AM manufacturing, since the high metal 3d printing cost is justified especially for aerospace or biomedical applications. Otherwise, considering also the need of a large scale manufacturable product, thermoplastic polymers were selected, offering low costs and fine 3D printing quality. Moreover, the wiper must correctly operate with constant properties in a range of temperatures between 5°C and 40°C according to European Union legislation. Comparing ABS, PLA and nylon materials, it turns out that the last one has an higher Heat Deflection Temperature (HDT) and therefore his mechanical properties start to decrease at higher temperatures. Carbon reinforced nylon, i.e. Nylforce CF produced by Fiber Force Italy, has been consequently choosen, presenting the following mechanical and thermal properties:

Mechanical properties			***Thermal properties***			
Density [kg/m^3]	Young module [MPa]	Ultimate tensile strenght [MPa]	Melting temperature [°C]	HDT [°C]	Max temp. of use long period [°C]	Max temp. of use short period [°C]
1000	6000	100	180	155	90 – 120	150

Table 6.1. Mechanical and thermal properties of Nylforce CF produced by Fiber Force Italy [54]

The initial hypothesis of introducing a straight blade into the novel compliant mechanism, similar to the one of the traditional wiper, was discarded because it would lead to a flexible mechanism with concentrated compliance, consequently having very thin flexible joints, which would compromise the system's durability and unable to generate enough pressure at the blade's ends. Therefore a wiper configuration with an initial already curved shape was decided. With the aim of simplify the research of the optimal configuration, is assigned a constant thickness of 12 mm to the wiper frame, in such a way to uniquely evaluate the geometrical parameters inside the plane. Differently from the Flexsys frame, which relies on triangular elements to divide an input force into two output forces, the design of the innovative frame introduced here draws inspiration from compliant mechanisms' principles, and therefore aims to incorporate within the same structure both rigid sections to withstand applied loads and flexible areas necessary for enabling the required movements essential for the component's functionality. This integration however makes every geometrical feature able to influence the overall monolithic frame. The frame concept was

initially created from scratch. Subsequently the main geometrical parameters such as position, thickness and inclination of internal features were inserted in a simple parametric model and refined through FEA and Adaptive Single Objective Optimization. By defining the maximum Von Mises stress as the objective function to be minimized, this approach facilitated the determination of the most appropriate geometric parameters' values, although the final arrangement was reached after some considerations. These ones were aimed to identifying the correct balanced positioning of flexible and stiff areas, which need to coexist within the same frame. Some details regarding the reasoning behind certain design choices of the final frame configuration were presented, offering a broader insight on CM's behaviour, followed by a subsequent comparison of numerical analyses results. The central area of the structure, being the one where the load is applied, has been modeled to be as rigid as possible, and simultaneously it was ensured that the outer regions possess ample flexibility to effectively conform to the windscreen's curvature across different operational conditions. This aims to exert adequate pressure, ensuring consistent contact even in extremely challenging gripping situations. In Figure 6.2. is reported a simplified overview of the arrangement that has been determined, considering A, B, C and D as the contact points with the windshield. The input force is predominantly transmitted across the entire structure through Element 1, while Elements 4 and 5 facilitate the transfer of pressure to the blade. They also enable localized enhancement of stiffness, converging at a common point.

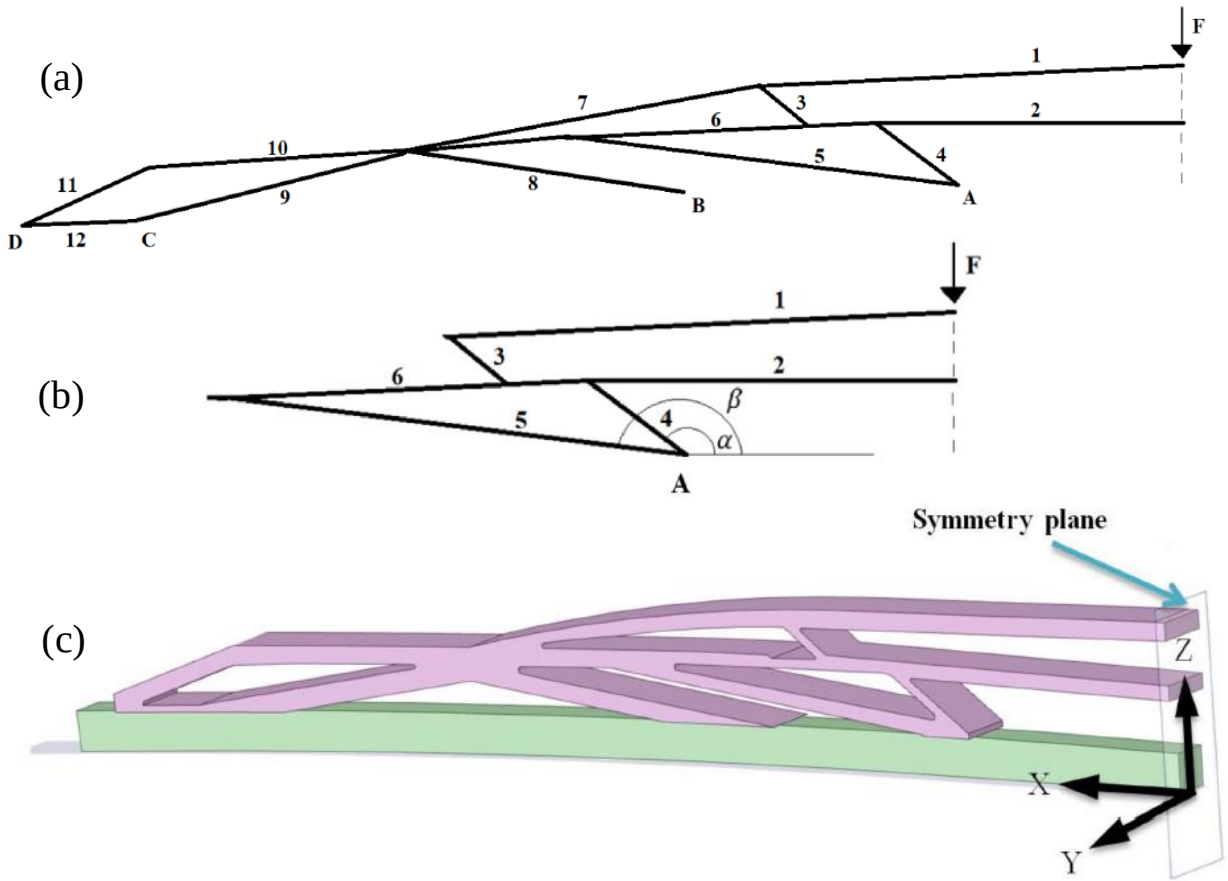

Figure 6.2. Simplified schematization of the novel compliant frame with relative numbering of internal features (a)(half frame is represented above since the structure is symmetrical) some geometrical details describing angles on point A (b) and Cad model of the novel compliant wiper (c)[54]

It's important to note that the frame and blade, as observed in existing market frames, aren't directly linked rigidly. Instead, they are connected via prismatic guides that enable the blade's movement along the guide's axis and restricts movement in the perpendicular direction. Thus, the positioning and angle of Elements 4 and 5 have been determined to strike a precise balance between sliding motion of the blade on the windshield and applying the required pressure. When the angles α and β (depicted in Figure 6.2) closely approach 90°, the pressure on Point A intensifies. However, this configuration restricts the blade's ability to slide appropriately along the

prismatic guides, potentially preventing the optimal functioning of the wiper and not allowing an appropriate adherence. Instead, the placement of element 2 was determined to enhance rigidity near the point where the load is applied. Element 7 assumes a function comparable to the Element 1, concurrently transmitting the input force towards the blade via Element 8 and through the interconnected system of Elements 9-10-11-12.

The inclination of Elements 8 and 9 was decided similarly as explained before for angles α and β, while Element 3 is essential to correctly transfer the load to the extremity on points C and D. Analyzing a general windshield's shape, it was found that the maximum radius of curvature is in the rest position, where the wiper spends most of its time in a deformed condition. Indeed, this condition is considered to be the most challenging since an uneven pressure distribution could lead to a permanent wiper deformation. An input force value of F_i = 10,79 N was obtained from literature [55] and confirmed through measurements.

6.2 FEA results and performance comparison

In FEA modeling, the frame was analyzed using brick quadratic elements with 20 nodes, each with 3 degrees of freedom describing the displacements. The windshield surface was instead modeled using shell elements with 4 nodes, each having six degrees of freedom, considering displacements and rotations around three axes. At least two elements along the thickness are used in every model analyzed. In Table 6.2 are reported the material properties of the three wipers compared.

Material	*Conventional frame Aluminum*	*Flexsys frame PBT – GF30*	*Innovative frame Nylforce CF*	*Blade rubber*	*Windshield Glass*
Young module [MPa]	*71000*	*9500*	*6000*	*7,6*	*8700*
Poisson coefficient	*0,33*	*0,42*	*0,42*	*0,49*	*0,25*

Table 6.2. Main mechanical properties of the three wipers analyzed [54]

A “Contact pressure analysis” was carried out comparing the three frames, with the aim of finding out which of them is able to apply pressure as evenly as possible on the windshield surface. In this stationary condition the wiper is subjected only to the vertical force F_i coming from the wiper arm, which presses down the rubber blade on the glass surface. Secondly, a “Flexural stiffness analysis” was implemented to assess if the two monolithic frames are able correctly operate also when in motion. Therefore, a motion along the glass surface was added, together with the vertical force F_i, which implies the presence of friction between contact surfaces. As explained before, the frame and the blade aren’t directly linked but are connected through prismatic guides. This interaction has been modeled in Contact pressure analysis considering a “no separation” contact type, which enables the mutual sliding between surfaces in tangential direction while is forbidden their separation in the normal direction. Since in the flexural stiffness analysis it became necessary to account for the impact of friction between the blade and the windscreen, a "Frictional" contact was established between them, imposing a friction coefficient of $\mu = 0.5$. This coefficient

corresponds to the highest friction value observed in wet conditions, as supported by data cited in literature [56]. In this analysis instead the rubber blade was considered bonded to the frame to better transfer the input load directly to the windshield surface. The presence of non-linear contacts in both analyses implied the use of Newton-Rhapson iterative method respectively with full and unsymmetric type in contact pressure and flexural stiffness analysis. Below in Figure 6.3 are shown the deformed shapes assumed by the three wipers in contact pressure analysis.

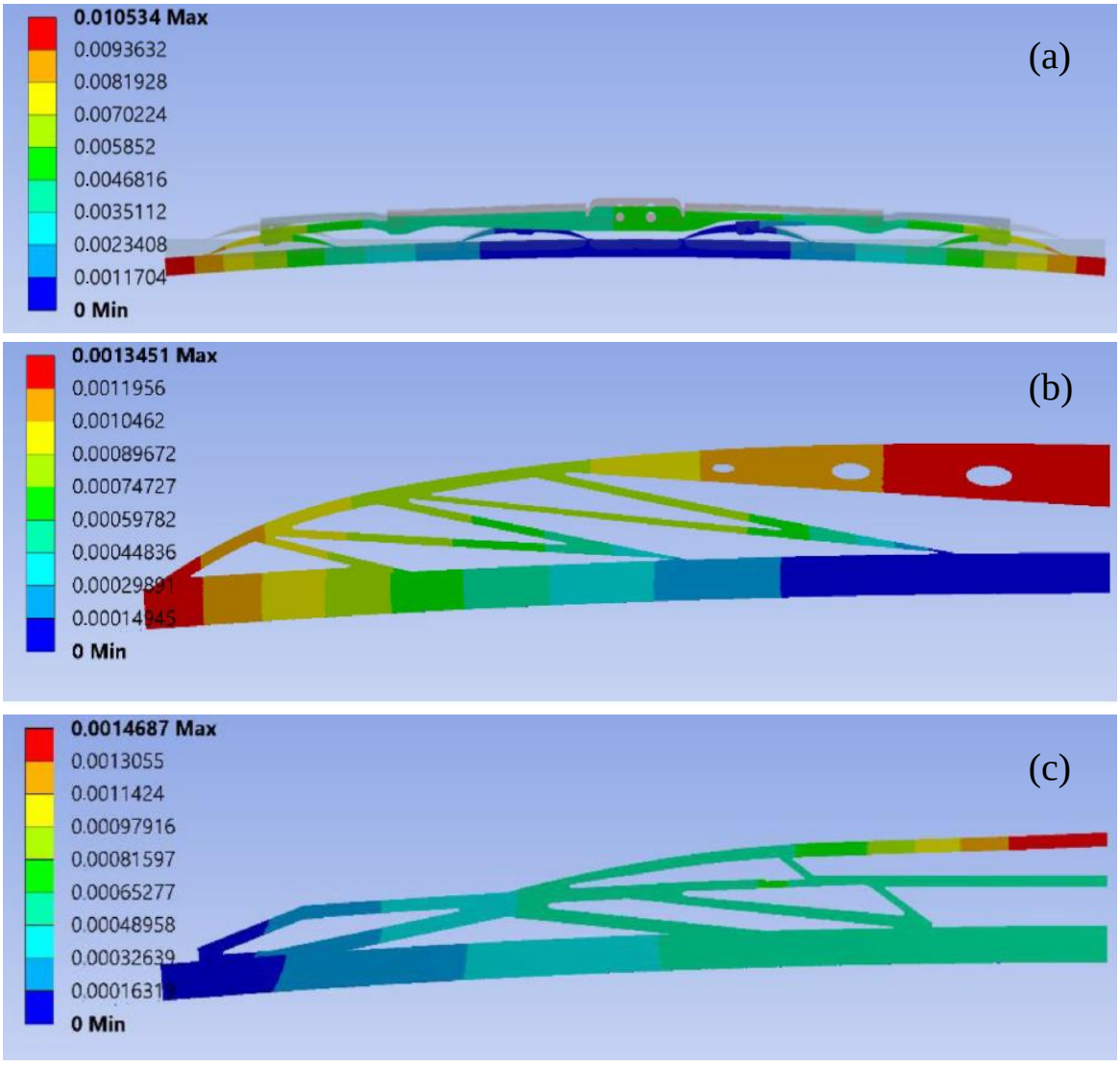

Figure 6.3. Total displacements [mm] of conventional aluminum frame (a), Flexsys frame and innovative compliant frame (c) from contact pressure analysis [54]

Since both Flexsys and the developed compliant frame have a symmetrical structure, only half of them has been analyzed and it's represented in Figure 6.3. Considering contact pressure analysis, the conventional aluminum frame experiences 10,5 mm of displacement at the ends of the frame, a much higher value compared with Flexsys and compliant frame, presenting maximum deformations respectively of 1,3 mm and 1,5 mm. The highest value of conventional frame is mainly due to the initial completely flat configuration of its blade in undeformed condition, differently from the monolithic wipers which already have a curved shape in undeformed conditions. In terms of stresses, each wiper has a maximum stress way far from the material limit, as described in the following Table 6.3. In Figure 6.4 are represented in side-view the deformed shapes of the monolithic wipers resulting from the flexural stiffness analysis. Both the single-component wipers demonstrate a sufficient stiffness while operating, moving almost rigidly along the windscreen's surface.

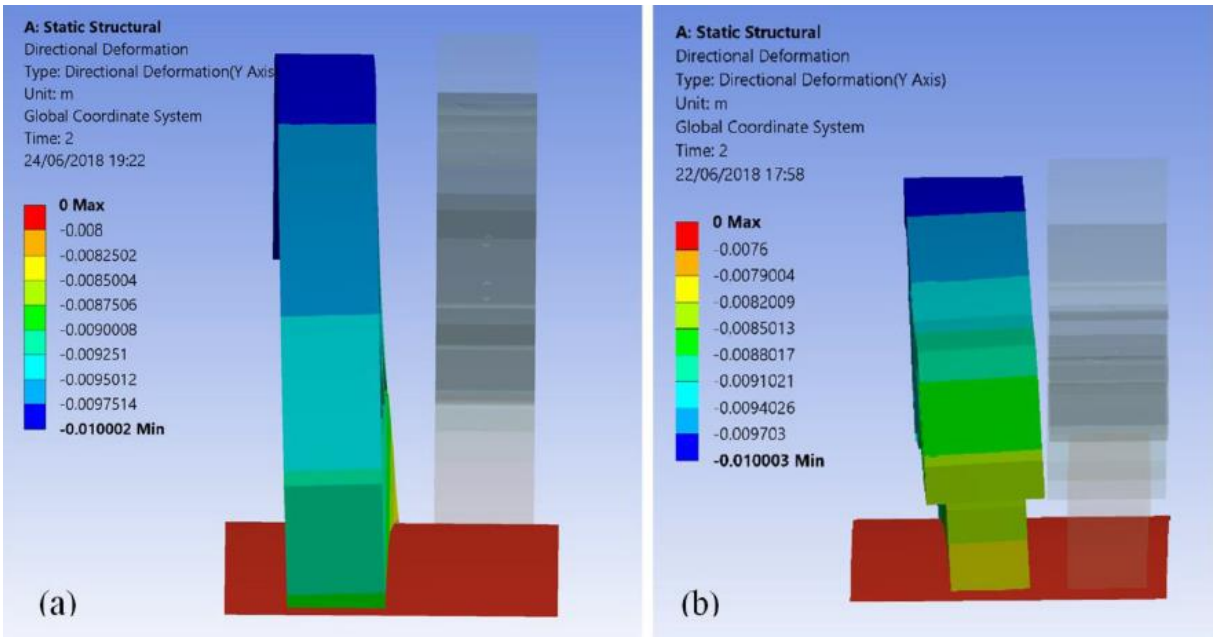

Figure 6.4. Total displacements [mm] of Flexsys frame (a) and innovative compliant frame (b) from flexural stiffness analysis [54]

Materials	σ_{max1} [MPa]	σ_{max2} [MPa]	σ_R [MPa]
Aluminum	68,4	/	300
PBT-GF30	23,2	60,2	130
Nylforce CF	16,9	23,4	100

Table 6.3. Comparison of wipers'performances in terms of stresses (the aluminum frame was not analyzed in the second load condition regarding flexural stiffness analysis) [54].

Also in flexural stiffness analysis the maximum stresses remain low, underlining the ability of uniformly distributing the stresses along all the monolithic structures. The interest in re-engineering a traditional wiper has been also motivated by the purpose of applying a more uniform pressure to the windshield. Indeed it was exploited the Compliant Mechanisms' possibility to internally deform, conveying the input force through the flexible frame of wiper towards larger areas of the windshield. To effectively assess the distribution of the pressure exerted on the windshield, the pressure trends along each of the three wipers have been analyzed and reported below. The areas with highest pressures were numbered starting from the wiper's extremity up to the middle. A graph reporting pressure values together with the extension of each pressure area is shown in Figures 6.5, 6.6 and 6.7. Traditional frame contains four mainly asymmetrical bell-shaped pressure trends with a maximum extension of 18 mm and a maximum pressure of 22,3 kPa which is equally reached by all the four pressure areas. Differently, the Flexsys frame revealed an unequal splitting of the input force in the three pressure areas, since the maximum pressure of 26,5 kPa is mostly withstanded by the area closest to the middle of wiper.

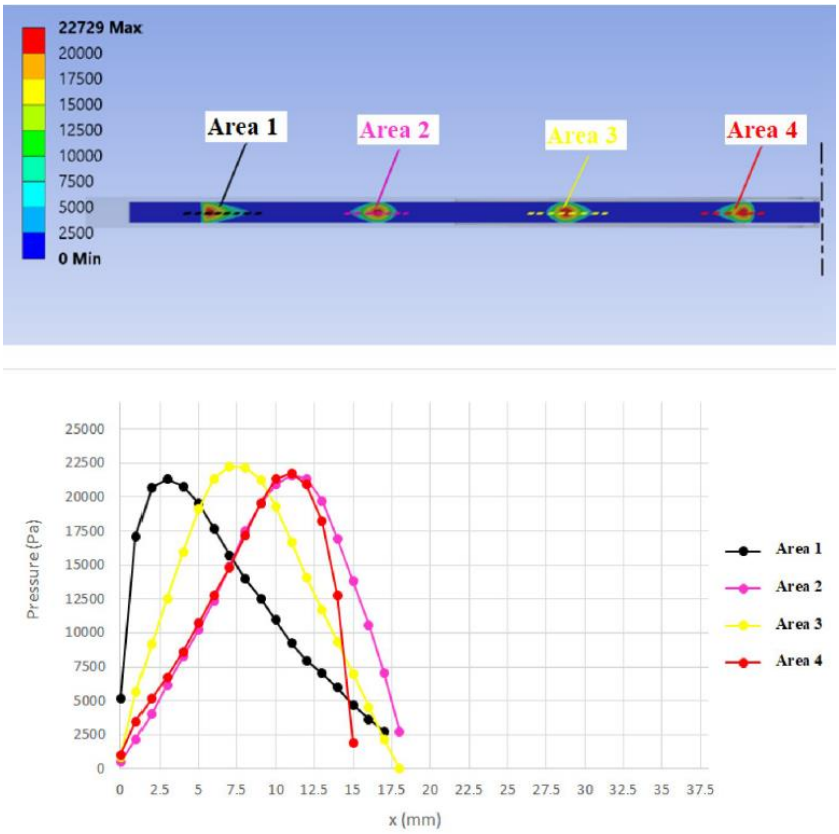

Figure 6.5. Pressure distribution on traditional frame and graph reporting pressure values and width of the areas subjected to highest pressure [54]

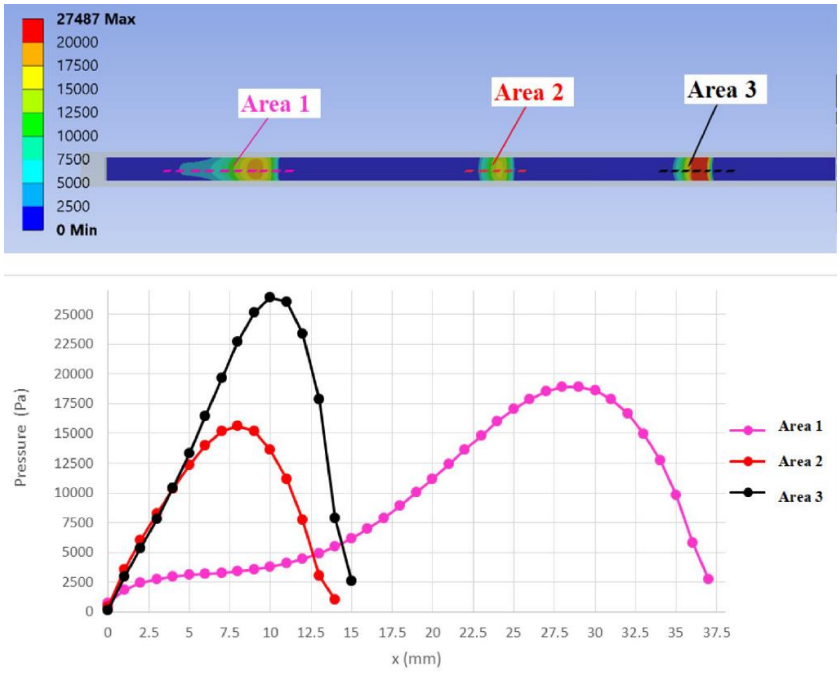

Figure 6.6. Pressure distribution on Flexsys frame and graph reporting pressure values and width of the areas subjected to highest pressure [54]

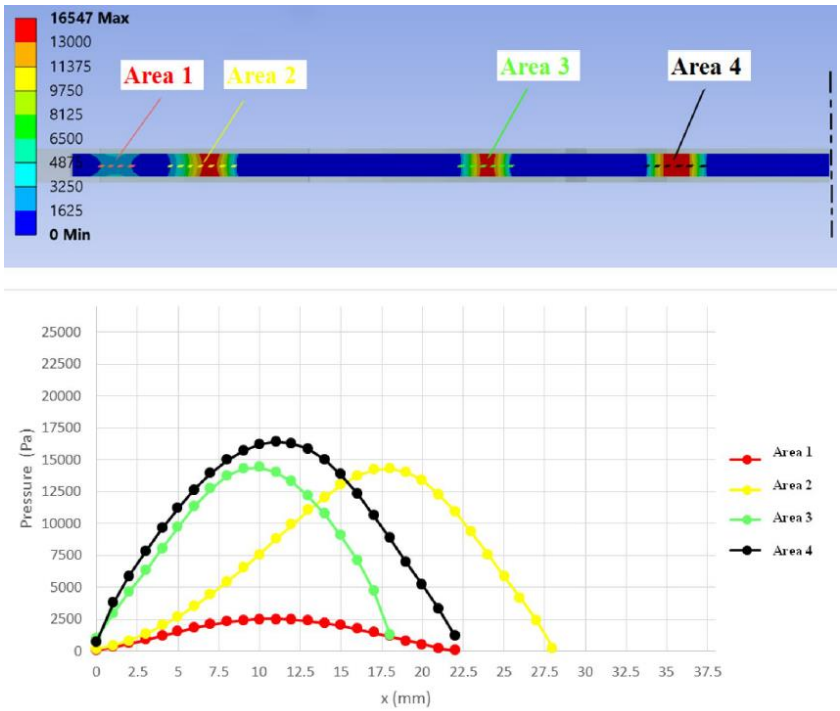

Figure 6.7. Pressure distribution on innovative compliant frame and graph reporting pressure values and width of the areas subjected to highest pressure [54]

Instead, it can be assessed that the main pressure areas of compliant monolithic frame have greater extension, having a maximum width of 28 mm. Moreover, compliant wiper's pressure trends show a more uniform distribution compared to the Flexsys frame and closely similar to the ones of traditional frame. Regarding the areas where substantial pressure values are registered in the monolithic compliant wiper, this ones appears to surpass both the conventional and Flexsys frames, reaching a 32.7% of the total contact area, enabling therefore a more efficient exploitation of the rubber blade. Another crucial aspect to consider in each frame is the positioning of Area 1 referred to the end of the rubber. This specific area, being the first from the extremity towards the centerline where significant pressure values are detected, is fundamental in ensuring the wiper's terminal part remains in contact with the windscreen surface. By measuring the distance between the

end of the rubber and the initial point where notable pressure values are observed in each of the three frames, this distance is 26 mm in the conventional frame, 25 mm in the Flexsys frame, and notably reduces to 10 mm in the innovative frame. Consequently, the innovative frame ensures the application of pressure in areas closer to the extremities compared to the other two frames. Achieving a more even pressure distribution across the blade surface could also offer additional advantages by reducing the noise and vibrations generated during wiper motion. It can be supposed that the condition where the windshield exhibits maximum curvature, coinciding with the wiper's rest position here used as a reference configuration for design, is also the most suitable condition to inducing vibrations [57]. Indeed it’s observed that high vibration amplitudes occur precisely at start and end of the wiper’s stroke, while relatively stable motion exists during the middle of the rotational stroke. Furthermore, a more uniform pressure, especially in the rest position assumed by the wiper most of its time, could avoid permanent deformations. Besides outperforming the Flexsys frame, the innovative compliant frame enables a weight reduction of 16,3 % compared to Flexsys’weight and 40,1% compared to the traditional wiper. Following is depicted the wiper prototype effectively realized by FDM using Nylforce CF with 100% filling.

Figure 6.8. FDM prototype of compliant monolithic frame realized in Nylforce CF[54]

The compromise between flexibility and stiffness was followed by diversifying the role of the various wiper areas depending on the point where are placed, enabling the compliant mechanism to behave rigidly where needed (near the application of input force) and to deform by properly conforming to the windshield curvature. Therefore, the combined reengineering approach here used, effectively merging the benefits provided by CMs with the production adaptability enabled by Additive Manufacturing, allowed a weight reduction of 40% and a part reduction from 19 to 1, compared to the traditional wiper frame. Considering the combined design approach here used to improve existing products, the possibility of simoultaneously exploiting also the suggestions coming from natural structures turns out to be even more appealing. The possibility of developing novel bio-inspired designs is therefore highlighted, benefitting both from Compliant Mechanisms and Additive Manufacturing advantages.

7. Actuation systems for FWMAVs: bio-inspired CMs

With the aim of pursuing a novel design approach, merging nature's solutions and living organisms' capabilities with the latest design techniques was considered a effective research direction to try out new projects. Keeping this in mind, this phase of dissertation was intended to explore the opportunities of re-engineering the innate flexibility of biological structures by combining the benefits of Compliant Mechanisms with the adaptability offered by Additive Manufacturing processes. Indeed, starting from the examination of insects' physical structures, it has been attempted to identify potentialities and critical aspects of employing CMs to create bio-inspired monolithic actuation mechanisms suitable for powering Flapping Wing Micro Air Vehicles (FWMAVs), feasible for fabrication through affordable 3D printing methods. Observing the internal characteristics that make insects able to fly, it was noticed the relevance of exploiting flexible internal organs during flapping flight, which play an important role in the transmission of energy from muscular apparatus to the wings. Therefore, several designs inspired by the motion of insects' wings have been developed, seeking to replicate both the functionality and the structure of insects' thoraxes using single-component flexible mechanisms. The design process and the outcomes coming from FEA studies are outlined below, backed up with insects' internal morphology description.

As previously aforementioned, Compliant Mechanisms can be regarded as an highly significant tool for mimicking flexible biological structures, and in this context, the area of robotics focusing on Micro Air Vehicles (MAVs) unquestionably represents an ideal domain for both embracing a bio-inspired design approach and implementing CMs. Indeed, CMs modeled after biological systems could potentially improve Flapping Wing MAVs' performances, considering CMs' capability to store energy via elastic deformation, diminishing friction, weight, wear, and the necessity for lubrication. The chance of CM's to be manufacturable with scalable designs is additionally valuable given the typically reduced dimension of FWMAVs. Moreover the assembly process and the maintenance of conventional rigid-body mechanisms used for the actuation of FWMAVs could particularly benefit from a replacement with a flexible monolithic actuation mechanism. The above features thus represent an opportunity to reducing the required number of components, simplifying construction complexities and also for potentially extending the flight range of FWMAVs. To better address the development of novel efficient actuation CMs with reduced energy consumption, an initial examination of the flight mechanisms in flapping wing insects and small birds was carried out. This phase had the purpose to identify the most flexible internal organs or apparatus which majorly constituting a suitable baseground to implement a compliant mechanism. Differently from fixed and rotary wing vehicles, FWMAVs waste a notable portion of the input power in counteracting inertial forces while reversing wing motion. Indeed, while the wing undergoes acceleration and deceleration, the air exerts pressure on the wing's surface, representing a

time-varying increase in the wing's inertia. This aspect was considered a relevant opportunity to take advantage of CMs' ability to continuously store and release energy in form of elastic deformation. In figure 7.1 are represented two schematic cross-sections describing two main insects' thorax configurations. Insects possess an apparatus characterized by a shell or exoskeleton composed of highly elastic materials, featuring chitin microfibers surrounded by a protein matrix [58].

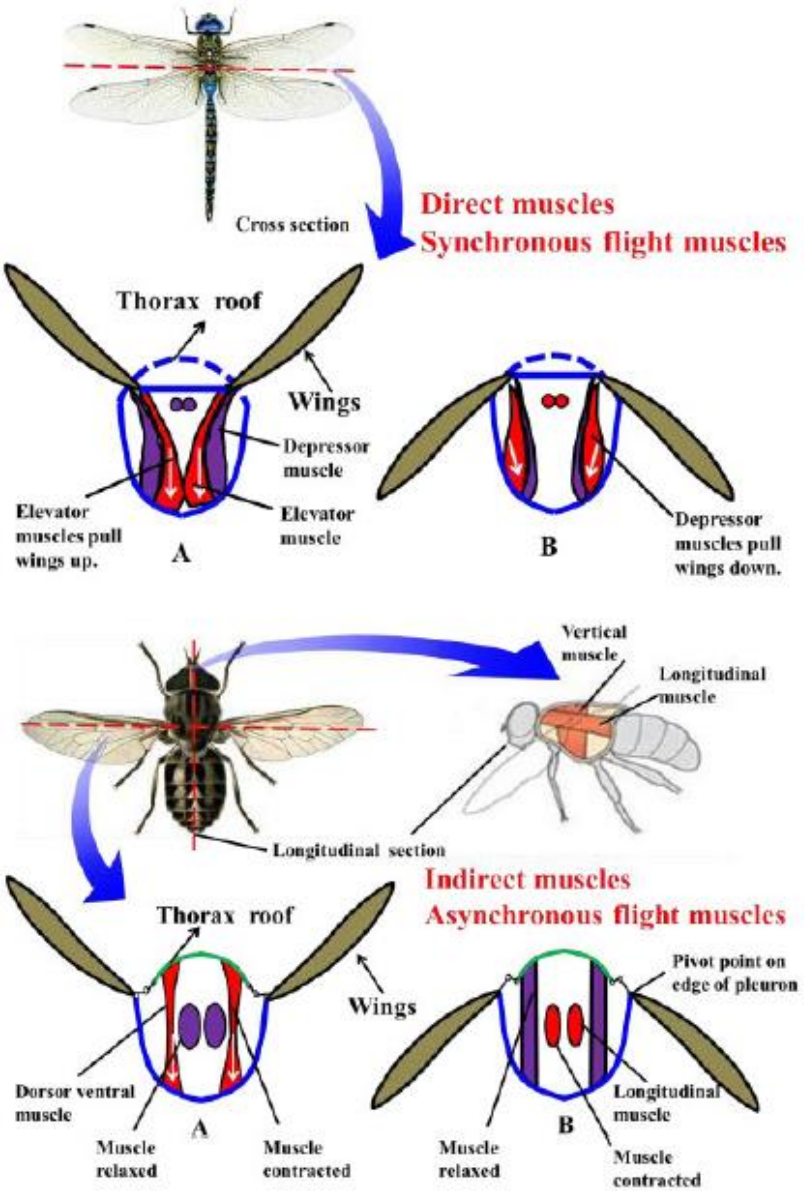

Figure 7.1. Schematic cross-sections of insects'thorax describing direct synchronous and indirect asynchronous flight muscles [58]

Their thorax can be conceptualized as a structure resembling a box, comprised of the sides, known as pleura, and the base, referred to as the sternum. The wings are attached to these sides through flexible membranes. Two methods exist to generate wing flapping, accomplished through either direct or indirect muscles. Direct synchronous muscles are employed for wing flapping in phylogenetically older insects like dragonflies, while indirect asynchronous muscles can be found in phylogenetically modern insects like bees and flies. In insects with direct muscles, the wings are directly joined to the two kinds of muscles, which are controlled separately by the brain and alternatively pull the wings up and down allowing relatively low flapping frequency but high agility. Otherwise, in insects with indirect muscles the wings' movements are executed through the hinge mechanism located at the wing's base, while the main wings'actuation is provided by the elastic deformation of the thorax shape. Indeed, vertical muscles contract to lower the thorax roof directly, causing the wing to move upward during upstroke. Conversely, downstroke motion is generated by longitudinal muscles, which deforming the thorax roof upward, allow the wings' downstroke motion. This second muscles configuration enables higher flapping frequencies and larger wing's rotation amplitudes.

Considering instead small birds like hummingbirds, their flapping flight is fundamentally generated by massive muscles supported by an endoskeleton (Figure 7.2 [58]). The hummingbird's ability to flap its wings at high frequencies and sustain high aerobic power is primarily attributed to its flight muscles, which contain fast oxidative-glycolytic fibers along with

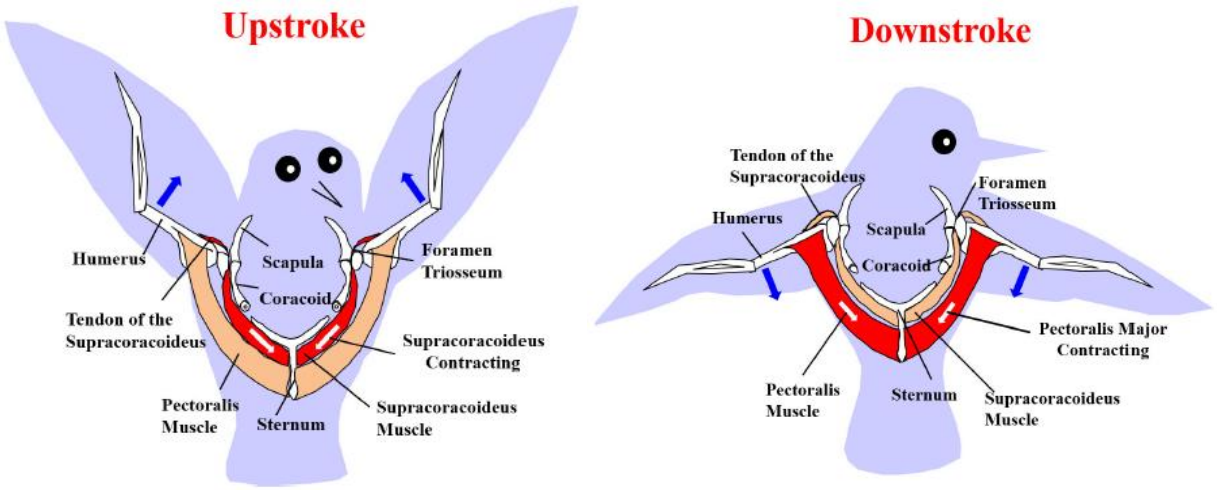

Figure 7.2. Schematic representation of muscoloskeletal structure of hummingbirds during upstroke and downstroke flapping motions [58]

substantial giant mitochondria, and constitute approximately 25-30% of their total body weight. A substantial difference can be therefore taken into account comparing the actuation mechanisms of insects and small birds like hummingbirds. It has been observed that the hummingbirds'flight is mainly resulting from their extremely efficient muscular structure, indeed among vertebrates they have the highest known mass-specific metabolism of around 40 ml oxygen per gram per hour when hovering [59]. On the other hand, has been found out that the insects' ability to store energy through internal elastic structures, rather than the use of particularly efficient muscles, allows them for lower energy consumption [60]. Based on these observations, has been assumed that employing structural components capable of cyclical elastic deformation and therefore suitable to store and release energy could enhance the efficiency and flight range of a Flapping Wing MAV. Consequently, it was decided to mainly draw inspiration from the flexible insects' thorax rather than hummingbirds, since the former provides a more suitable basis to exploit CMs' flexibility, while re-

engineering the hummingbirds' structure substantially would require the use of high energy efficient power sources, at least comparable to the high efficiency of hummingbirds' muscular apparatus. Once established the source to be used as starting point for defining a novel bio-inspired mechanism, another relevant issue is related to the choice of a manufacturing process suitable for this kind of applications. Upon examining various prototypes of flapping wing vehicles and microrobots, it's noteworthy to mention some of the most interesting techniques observed in scientific literature. One example is provided by the use of injection molding process, which despite being able to generate compliant mechanisms, it necessitates a prior study to design multipiece multigate molds together with proper molding process constraints [61]. An alternative manufacturing approach is represented by the so-called Smart Composite Microstructure process (SCM), which consists of a series of laser micromachining and lamination operations [62]. In particular, a flexible polymeric material is inserted between sheets exhibiting a more stiff behaviour, e.g. composite materials, in such a way that the globally rigid sheets are locally made flexible in some particular sections where only the

Figure 7.3. Details on the production sequence of flexible joints through Smart Composite Microstructure technique [62]

polymeric material is maintained while the stiffer material is removed. Although this process is able to succesfully integrate flexible and rigid areas within the same domain, in requires an accurate phase of process' development. Therefore, while both preceding studies propose effective manufacturing processes for producing flexible mechanisms, their feasibility turns out to be complex considering their costs and a nontrivial setting up phase. Taking into account also these aspects, the Fused Deposition Modeling (FDM) process has been selected for the design of novel flexible monolithic actuation mechanisms, in particular since FDM stands out as a cost-effective technology that enables achieving high-quality results while providing a broad range of available materials. Considering the need to create a monolithic actuation mechanism where highly flexible regions have to coexist in proximity of rigid structural areas within the same layout, an essential role is played by the material to be used. Indeed, in order to compare different materials and evaluate the most appropriate one for this application, several materials commonly employed in Fused Deposition Modeling (FDM) processes, such as ABS, PLA, Nylon 645, Ninjaflex, FlexiFil, and Onyx, were subjected to preliminary testing. Therefore, in an initial phase, a series of non-linear FEM analyses have been conducted using different materials on various configurations of flexible actuation mechanisms, in order to assess their mechanical behaviour and identify the material that would allow an appropriate compromise between rigidity and flexibility. After comparing the dimensions that generally have FWMAVs actuation mechanisms from literature, has been assigned to the analyzed layouts a maximum planar size of 70 mm x 70 mm and a mininum thickness

of flexible regions of 1 mm approximately. In this step of design it was decided to set for the planar mechanisms a uniform thickness of 5 mm. This aspect will be further analyzed and discussed when dealing with topology optimization desings following, considering also a comparison involving uniform thickness on mechanism's plane. At this exploratory stage it was preferred not to consider the influence of the thickness basically in order to focus the attention on examining the overall mechanism behaviour without affecting it also with problems of low "Off-axis stiffness". Therefore an high off-axis stiffness is desirable, since this latter, as seen on Chapter 2, represents the ratio between the stiffness concerning an undesired axis divided by the the stiffness along the axis around which the motion must take place. After various initial FEA, some of the initially considered materials, such ABS, PLA, Nylon and Onyx, were discarded since they have turned out to be excessively rigid to be effectively exploited within the considered design space for this application. Conversely, despite the capacity of Ninjaflex to facilitate extensive elastic deformations in the flexible regions, it was discarded too from consideration since it's also noteworthy its unsuitability to provide the necessary overall stiffness to the mechanism, potentially resulting in buckling instability. In Table 7.1 is provided a table useful for comparing Young's Modulus of these materials.

	ABS	PLA	Nylon12	Onyx	Ninjaflex
Young's Modulus [MPa]	2270	2345	1300	2400	12
Specific gravity [g/cc]	1,06	1,24	1,05	1,2	1,19
sources	*xometry.eu*			*markforged.com*	*ninjatek.com*

Table 7.1. Properties of FDM materials preliminarly tested

After considering these aspects, the choice of material conducted to the use of FlexiFil, a partially bio-based Thermo-plastic Co-Polyester (TPC) whose main properties, outlined in Table 7.2, provide a mechanical behaviour halfway between rigid FDM materials and Ninjaflex, especially in terms of flexibility.

	Specific gravity	Young's modulus	Tensile strenght	Elongation at break	Hardness
FlexiFil™	1,14 [g/cc]	95 [MPa]	24 [MPa]	530 %	45 D
sources	*Formfutura.com*				

Table 7.2. FlexiFil™ main mechanical properties [63]

As following better clarified by FEA results, this material allowed the most appropriate compromise for defining a monolithic structure that results comprehensively stable, being rigid where needed and at the same time enough flexible in certain areas, enabling significant displacements and rotations. The choice of the driving actuator for providing energy to the flexible mechanism has been made considering both the maximum planar size established as target of the mechanisms and the material to be used. From a distibution of the main driving actuators employed in existing prototypes in literature (Figure 7.4 [45]), correlated to the corresponding dimensions and weights of insect inspired flapping vehicles, stands out that the use of DC motors would be recommended considering, along with the mechanism itself, also the wings' length and the required electric/electronic accessories.

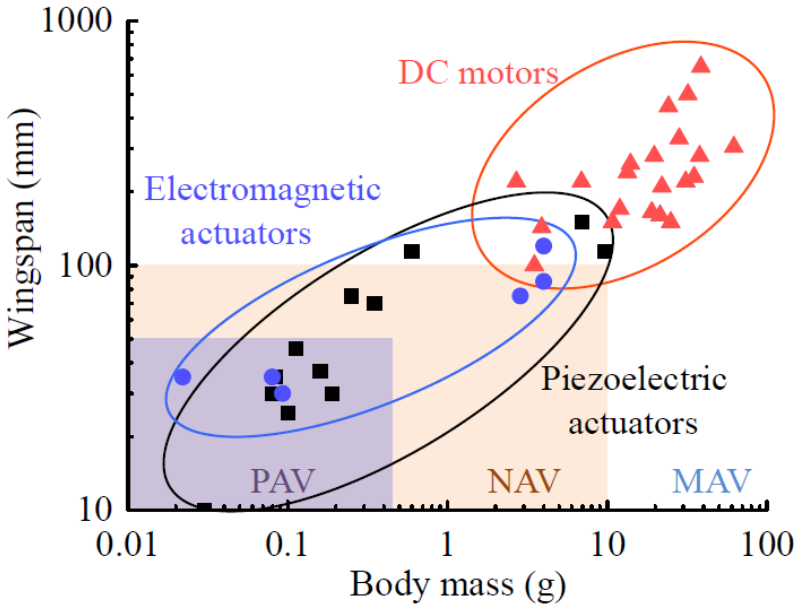

Figure 7.4. Distribution of driving actuators used in insect-inspired vehicles according to dimensions and weights of each specific range of vehicles [45]

Therefore, DC motors were selected as propulsion systems also taking into account their reliability, versatility and availability as cheap off the shelf products. Drawing inspiration from the thoracic structures observed before in flapping wing insects employing indirect muscles, several configurations of single-component CMs were devised and extensively examined through non-linear FEM analyses in order to assess their mechanical performance and their ability to generate a wing motion useful for FWMAVs. Each bio-inspired layout has been conceived by conceptually dividing the mechanism's areas in three parts with three distinct functions. Some regions take a role similar to the one of the flexible area of the thorax, which cyclically deforms, storing and releasing part of the input energy. The energy release for instance could be advantageous especially during the motion inversion, when happens the "added mass effect" described before, and representing a time-varying increase of wing's inertia.

Other mechanism's regions are instead designed with the aim of mimicking the action of muscles that alternately deform the thorax upwards and downwards. While these two previous areas should adopt a flexible behaviour, from the third kind of area it's conversely required a more rigid function, since it represents the stiff thoracic region responsible for supporting the rotation of the wings and providing an overall stability to the mechanism. Therefore, taking inspiration from insect's morphology, four different bio-inspired layouts were modeled and tested through non-linear FEA, whose results are following outlined. Layout 1, whose meshed geometry is represented in Figure 7.5, has been modeled as a planar CM with a uniform thickness of 5 mm. The mesh of the model has been attentioned so as to have on the areas of minimum cross-section at least 3 elements along the thickness. FEA analyses were conducted using quadratic

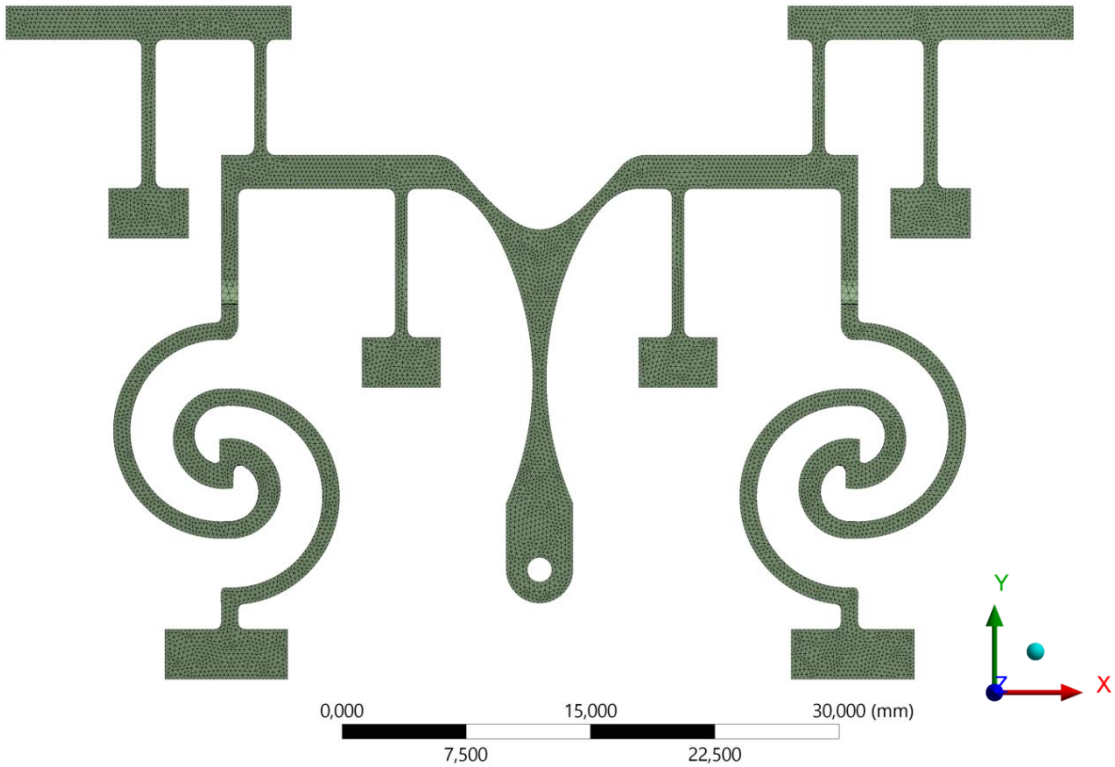

Figure 7.5. Layout 1: Meshed model of Bio-inspired Compliant Mechanism

brick elements with 20 nodes, each with 3 DOFs related to the displacements along the 3 axes. Quadratic tetrahedral elements were also used where needed, especially in proximity of high curvature areas. The shape of some regions resembling some kind of spring was conceived to elastically connect the parts near to the wings to the fixed supports of the mechanism, in such a way to not to localize the deformation only in small areas. Non-linear FEA analyses were required for taking into account the stiffness' changes of the highly flexible material, which undergoes to large deformations when is actuated by the rotation of an electric DC motor. Indeed, in this exploratory stage it has been decided to set the flapping frequencies to 15 Hz. The boundary conditions imposed for this model are more clearly visible in Figure 7.6a, which depicts the stress distribution of mechanism considered in a deformed configuration corresponding to the downward motion of wings. A brushless DC motor is connected to the CM by means of a crank (both of them are not shown). The rotation axis of DC motor is highlighted with an orange X in Figures 7.6. During the rotation of the DC motor, the area A of the CM is driven along a circular trajectory (yellow dashed line) in the XY plane. The area A has a shape of a circular hole so as to be able to accomodate a low friction bearing that connects the CM to the crank. As the area A goes through the circular yellow dotted trajectory, the area D, directly connected with A, experiences alternating upward and downward movements. This area assumes a role similar to the one of the flexible thorax in insects with indirect muscles, as noted above. These two regions A and D, despite being within the same single-component flexible mechanism, make it possible the conversion of the continuous rotary input motion

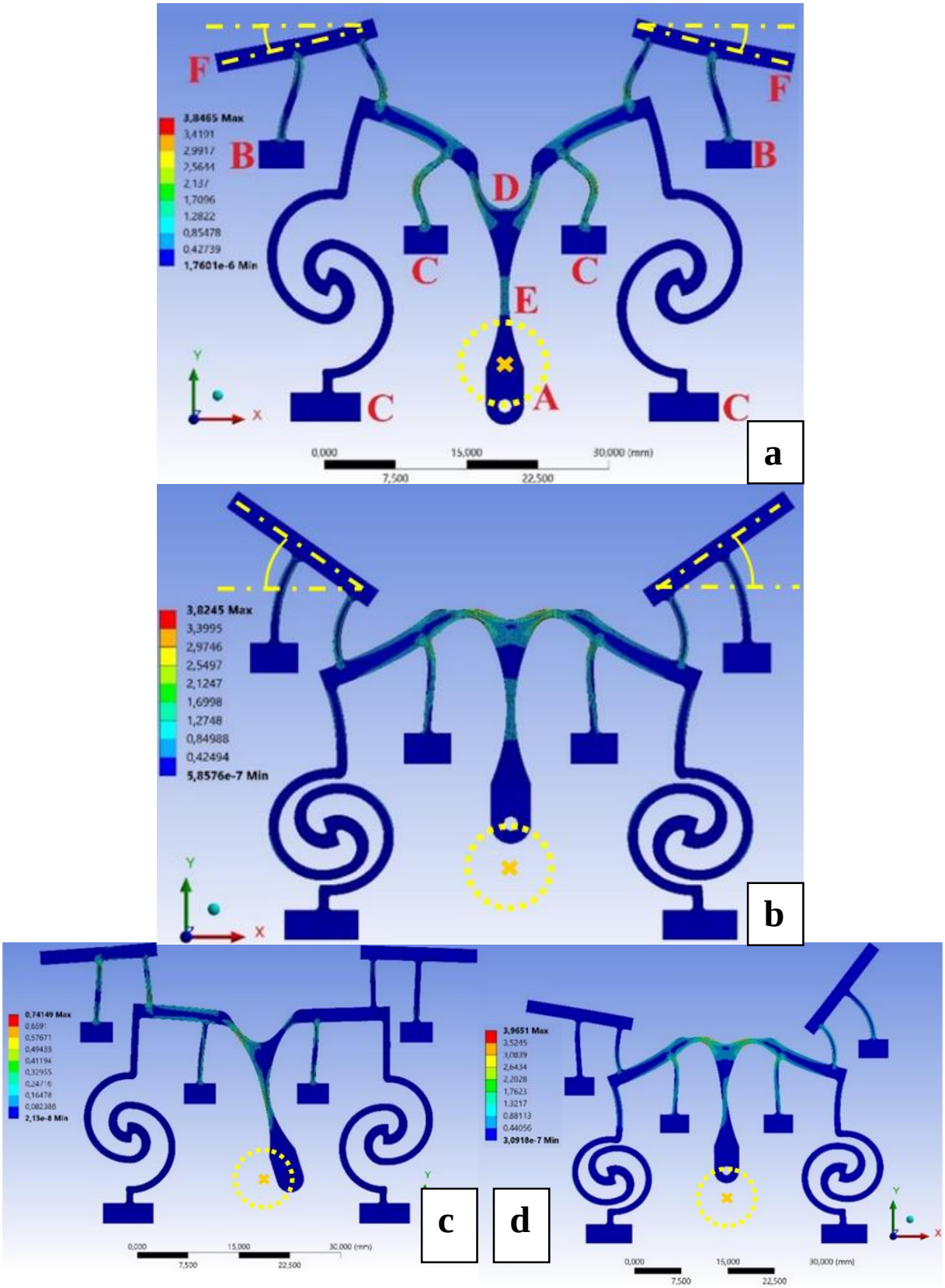

Figure 7.6. Layout 1: end of downstroke (a), end of upstroke (b), central position of wings with an angle of 0° (c), and position of asymmetrical wing rotation (d) [64]

generated by the electric motor into an alternating translational output movement to be transmitted to the wings. Therefore the motion of the area D, combined with the bending of the adjacent regions, enables the symmetrical alternating rotational movement of the two areas labeled as F. Although not depicted in Fig. 7.6, the two flapping wings are linked to the single-component CM through these areas F. The yellow dash-dot lines shown in Fig. 7.6a and Fig. 7.6b define the angles delineated by the wings' rotation as they move away from the central horizontal position. Ultimately, supports B and C have been fixed to the frame and linked to the mechanism through flexible regions. Among these, the ones exhibiting a spiral shape have been specifically designed to be useful in storing and releasing energy through their elastic deformations. The area marked as E has been modeled with a decreased thickness compared to its neighboring sections. This deliberate design aims to decouple the displacement of area A along the x-direction from the rest of the mechanism. Consequently, even when area A moves to asymmetric positions along the x-axis (as depicted in Fig. 7.6c), the wing supports are able to maintain symmetrical positions relative to each other. This particular arrangement provides to the mechanism the capability to transform a continuous rotary input motion from the DC motor into an alternate symmetrical rotation of the wings, decoupling the two motions so as to be independent along the x-axis. In Figure 7.6a and b are respectively depicted the maximum downstroke and upstroke positions, when the wings reach the extreme positions regarding to the middle of the stroke. This deformed configuration is represented in Figure 7.6c, where it can be seen an almost perfectly horizontal position of the wings. In Fig. 7.6d, an

approach is illustrated wherein the two wings rotate differentially by inducing opposite displacements of supports B, which are inversely shifted upwards and downwards by few millimeters. This FEA has been in particular carried out with the purpose of exploring a possible actuation control of the flapping motions. Indeed, as described in Chapter 4, to make a flapping vehicle capable to perform yaw, pitch and roll maneuvers, it's possible to operate both adjusting flapping frequencies and shifting the flapping planes. Therefore, in addition to a possible flapping frequency control through the DC motor's speed, this analysis suggested another potential approach to perform flapping maneuvers. Moreover, depending on the different requirements involving both fixed supports positioning or adjustable ones (such as B supports in Fig.7.6a), this layout and also the following presented below could be potentially beneficial for a parameterization of geometry, enabling also an optimization of specified geometric parameters, leading to customizable designs of compliant actuation mechanisms. Different bio-inspired CM's layouts resulting from the assessment of insects' indirect muscle arrangement, are depicted below in Figure 7.7, 7.8 and 7,9. Some prototypes made of FlexiFil material using FDM (as shown in Fig.7.7 and 7.9) have been additionally generated in this instance. The printing parameters used for the FDM process are reported below in Table 7.3 [65].

	Nozzle temperature	Bed temperature	Initial layer printing speed	Printing speed
FlexiFil™	215 °C	55 °C	15 mm/s	30 mm/s

Table 7.3. FDM printing parameters of FlexiFil™ [65]

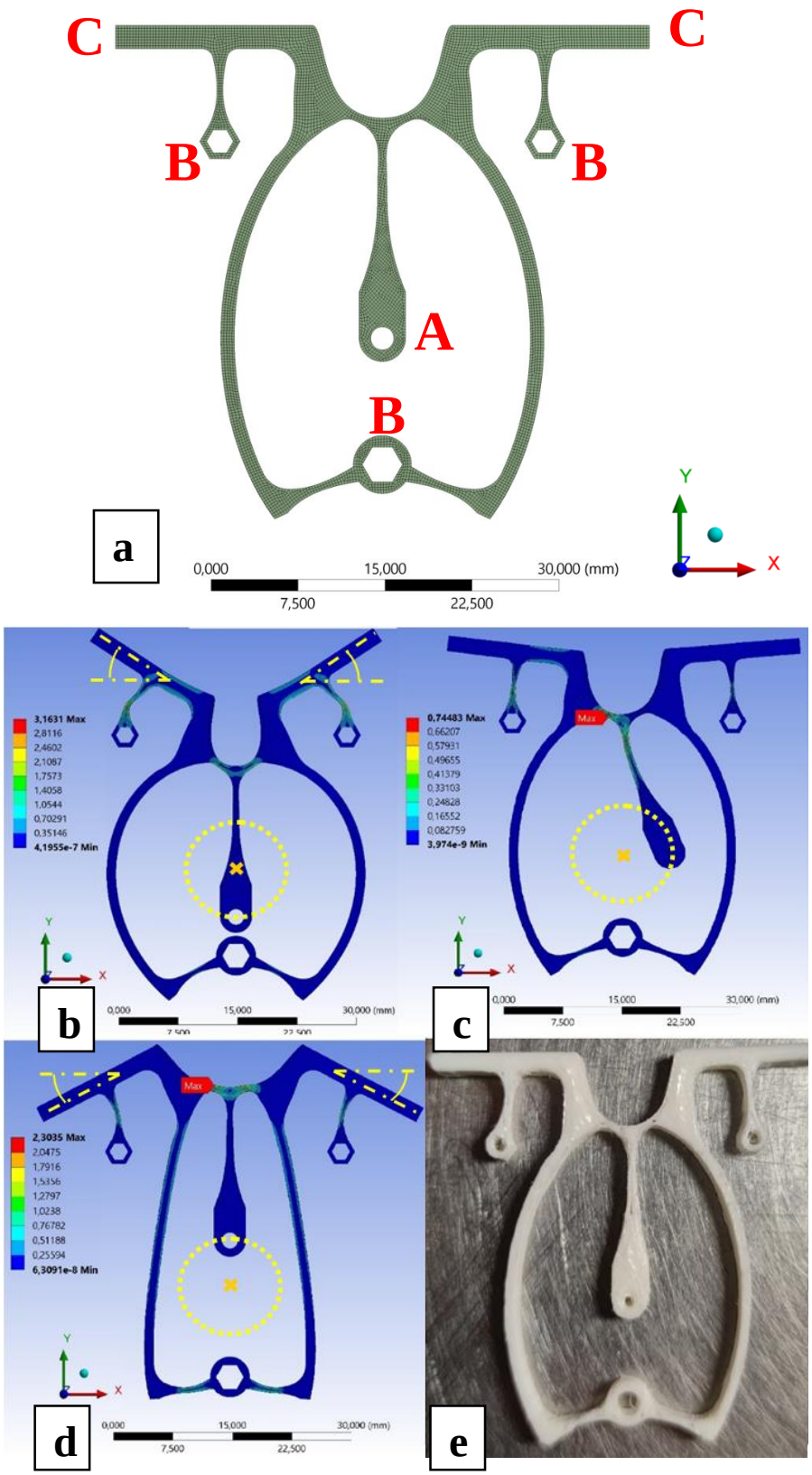

Figure 7.7. Layout 2: Meshed model of Bio-inspired Compliant Mechanism (a), CM configuration at the end of upstroke (b), central position of wings with an angle of 0° (c), end of downstroke (d) and FDM 3D printed model in Flexifil (e) [64]

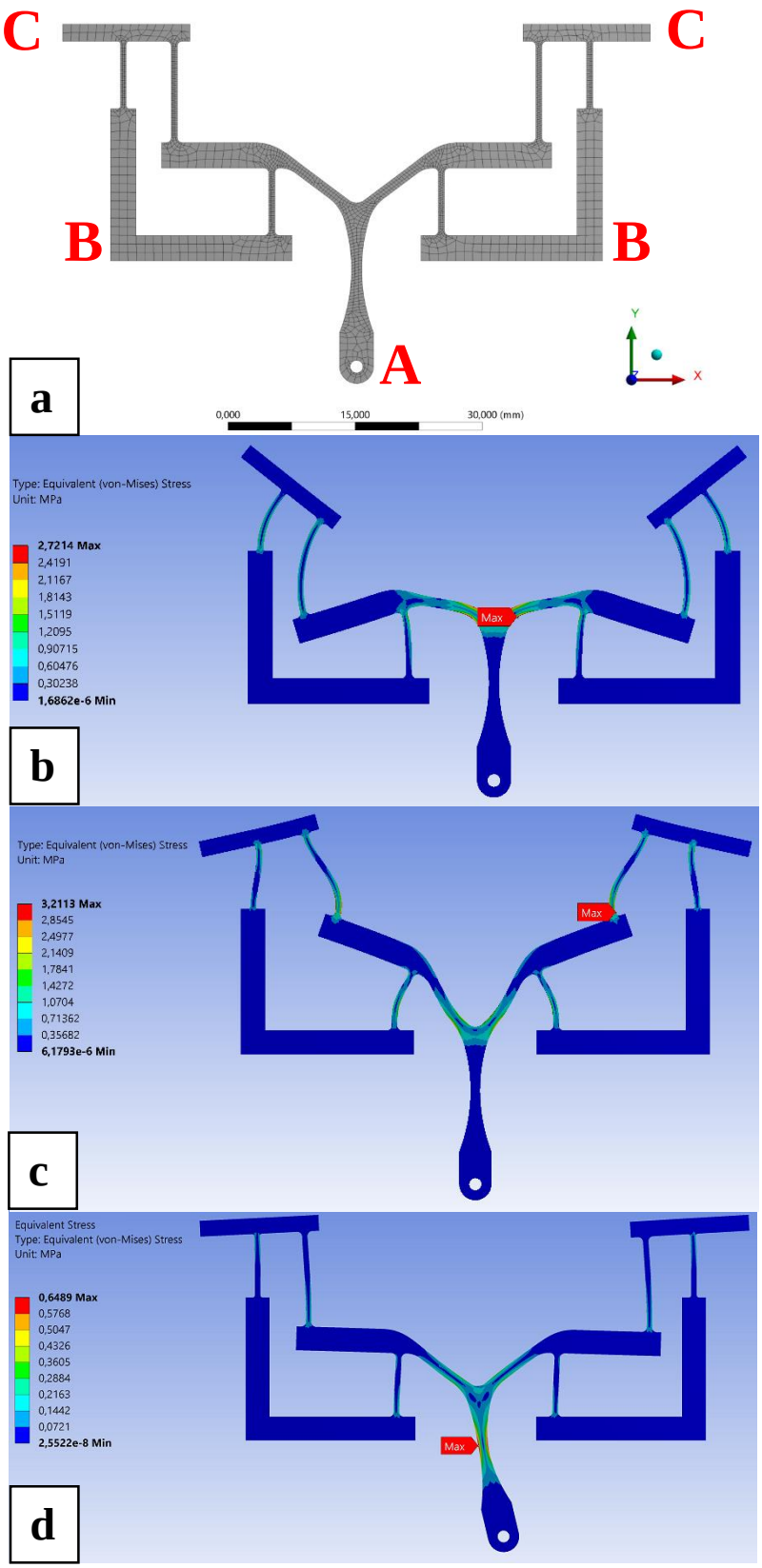

Figure 7.8. Layout 3: Meshed model of Bio-inspired Compliant Mechanism (a), CM configuration at the end of upstroke (b), central position of wings with an angle of 0° (c), end of downstroke (d)

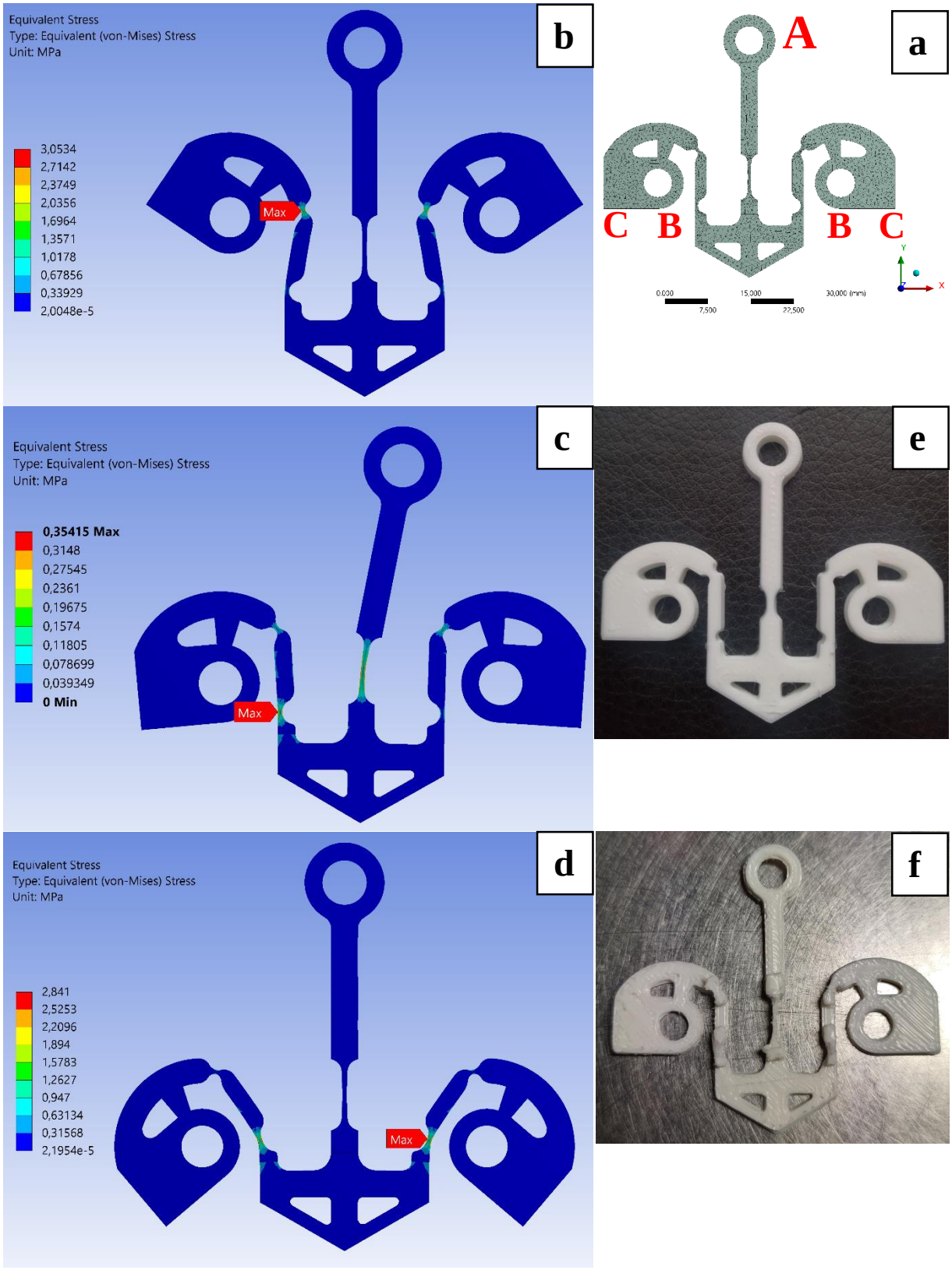

Figure 7.9. Layout 4: Meshed model of Bio-inspired Compliant Mechanism (a), CM configuration at the end of upstroke (b), central position of wings with an angle of 0° (c), end of downstroke (d) and two versions of FDM 3D printed model in Flexifil (e,f)

In contrast to the configuration previously outlined, a streamlined and more compact design has been modeled, aiming to mimic the shape and operational capabilities of the thoracic morphology in insects equipped with indirect asynchronous muscles. The roles performed by the distinct regions of the monolithic mechanism are similar to those depicted in Figure 7.6 for layout 1. However, in this different concept an attempt was made to more evenly allocate the deformations across the overall structure. Indeed, the oval shaped structure resembling the insects' thorax, has been specifically created with the purpose of more flexibly connect the area A where the input motion is applied (see Fig.7.7a) with the regions C related to the wings'motion. In all the layouts 2,3 and 4, (see Fig. 7.7a, 7.8a and 7.9a) the areas highlighted with the letter A are related to the areas of input motion, the areas indicated with B refers to the fixed parts of the mechanism while the areas C account for the regions where wings are connected.

For the sake of clarity, in Figure 7.10 is reported a simplified perspective view of layout 2, comprehensive of hypothetical wings and engine, positioned in relation to the CM, aiming to offer a more intuitive illustration of the CM arrangement. The orange dash-dot line highlights the rotational axis of the motor (illustrated by the cylindrical shape A). The CM is fixed to the frame through the areas marked as B, whereas areas C indicate the junction points where the two wings connect with the CM. The input displacement for all the layouts, as already explained in Figure 7.6a, is transferred to the mechanism in the area A through a crank with a radius of 5 mm (layout 1 and 2) or 4 mm (layout 3 and 4). Even if all the layouts have

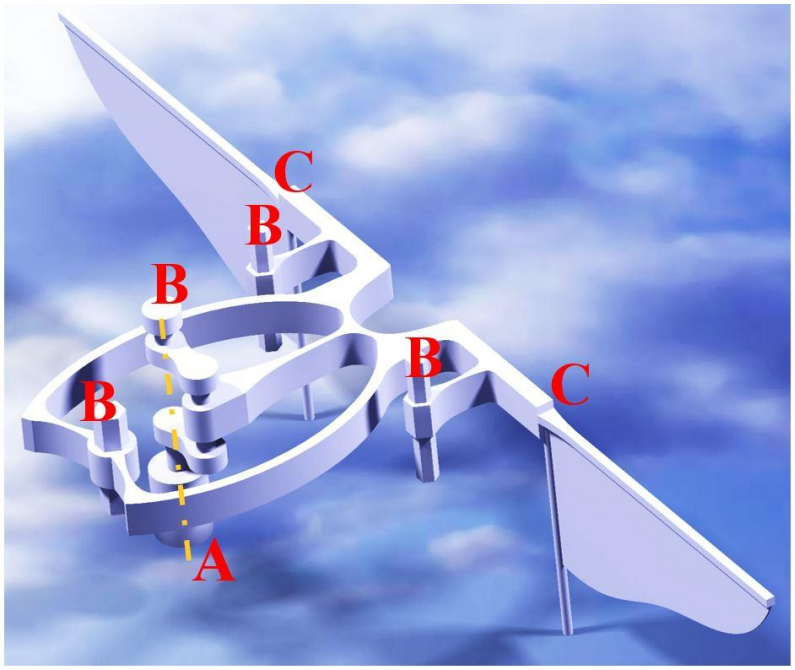

Figure 7.10. Simplified perspective view representing the Layout 2 of Bio-inspired Compliant Mechanism with relative positioning of engine and wings [64]

a uniform thickness of 5 mm along the z-axis and a minimum thickness of 1mm on the flexible regions, for layout 4 has been tried to analyze a model with a minimum thickness below 1mm, of approximately 0,5mm. Even if the model behaviour benefits from this thickness reduction, without showing relevant stress or deformation increase (Fig. 7.9) the 3D printing effectiveness in producing very thin cross-sections was negatively affected. An attempt was also made to print some thickness lower than 1mm by locally integrating the affected areas with a supplementary thickness in the z-axis (Fig.7.9f) in order to provide a better support for the thin material during printing, but this try reveals to be unsuccessful. Another 3D printing attempt modeling cross-sections with a minimum thickness of 1mm has instead brought back a better quality of the model (Figure 7.9e). The layout 3 is substantially a reinterpretation of layout 1, since the spiral shaped elements are roughly replaced by the beam shaped elements.

Considering the stress maps, the maximum values of the equivalent Von Mises stress observed in the different analyzed configurations are approximately between six and eight times lower than the tensile strength of FlexiFil. The stress distributions however show that a large part of the majorly stressed material is not evenly distributed overall the compliant mechanism, but it is mainly concentrated in the cross-section areas having lower thicknesses. Moreover, the thickest regions of the monolithic mechanisms (accounting for the largest mass of the CM) should likewise withstand the intertial effects due to the flapping motion, therefore apply an additional inertial force to the thinnest regions. In this perspective, the identification of a better material distribution, through topology optimization, results to be essential also in order to avoid both stress concentrations and the presence of too much heavy regions, trying instead to achieve a more even and efficient distribution of material.

8. Topology Optimization of CMs: Solid elements FEA modeling

A combined design approach, exploiting Topology Optimization, Compliant Mechanisms and low-cost 3D printing will be described following, applied to the development of Flapping Wing Micro Air Vehicle's wing actuation mechanisms. In order to investigate the capabilities of TO, a series of optimizations was implemented exploring four different design domains. Specific boundary conditions have been assigned to each one of them, in such a way as to observe the impact of distinct supports' positioning on mechanism performance. The reciprocal interaction between supports and wings, mutually assuming different placing within each design domain, has been investigated as well. At the same time, the optimization process was carried out also with the purpose of examining the influence of imposing several amounts of input and output displacements as TO constraints parameters. Subsequently to the optimization process, the topology resulting from the various design domains were examined and geometrically remodeled. This CAD remodeling phase is essential both to produce a well-defined CM's layout, suitable to be further analyzed by non-linear FEA, and to provide a 3D model properly tailored to comply with FDM 3D printing process parameters. The resulting monolithic compliant actuation mechanisms were at last compared taking into account transient FEA results in terms of stress distribution and range of motion provided to the FWMAV.

Among other structural optimization methods, the choice of Topology Optimization has been taken also considering its advantage to be applied in a generical design domain, which reveals to be a useful feature especially when facing complex design problems as in this instance. Indeed, setting out an effective flexible mechanism geometry, suitable to withstand high deformations at high frequencies within a restricted design space, turns out to be a non-trivial design problem, considering also the need to convert a continuous rotary input motion into an alternating symmetrical rotation required in output. Also for these layouts, the Fused Deposition Modeling (FDM) process was chosen due to its cost-effectiveness, extensive material choice, and its capacity to provide high-quality components. Considering the maximum overall dimensions (70 mm x 60 mm) of the design domains analyzed below, and also drawing from the previous experiences in FDM printing of flexible monolithic actuation mechanisms, a decision was made to set a minimum thickness of 1 mm during the geometrical remodeling of the flexible cross-sections. Flexifil, the thermoplastic co-polyester material whose propertied were described in the previous chapter, was used also in these designs, representing the appropriate balancing between flexibility and stiffness. Concerning the TO method specifically exploited for these analyses, the Solid Isotropi Material with Penalization (SIMP) method has been chosen (as described in paragraph 3.2) because of its straightforward conceptual simplicity and its computational efficiency [66]. To deal with the conversion of the continuous rotary input motion from an electric motor into an alternating symmetrical rotational output movement of the wings, a method was required to separate in some way these two motions, although

inevitably carrying out them within the same monolithic structure. Consequently, a potential solution was proposed, conceptualizing the division of the continuous rotary input motion into two distinct and alternating orthogonal linear motions. This partitioning served a dual purpose: firstly, to establish a suitable initial optimization domain, and secondly, to configure the preliminary Finite Element Method (FEM) analyses required for the topology optimization process. Drawing from comparable existing prototypes of FWMAVs and on the previously discussed layouts, the decision was made to design a mechanism capable of executing an entire flapping cycle at a frequency of 25 Hz. The meshed 3D models are reported below in Figure 8.1 along with some dimensional indications. For the mesh definition, quadratic solid elements have been used, each one having 20 nodes with 3 DOFs related to the displacements along the 3 axes. All the models have been discretized with approximately 36000 elements with 0,5 mm minimum dimensions. Each design domain has been modeled with a uniform thickness of 2,5 mm. Layouts a, b, and c have a maximum overall planar dimension of 60 mm x 60 mm (Fig.8.1a, b and c). Otherwise, layout d is slightly broader (70 mm x 60 mm) due to the placement of low-friction bearings in close proximity of the fastening areas of the two wings (Fig.8.1d). Together with the initial design domains of the CMs, two steel low-friction bearings are shown for each layout. These bearings feature internal and external diameters respectively of 2 mm and 5 mm, with a thickness measuring 2,5 mm. With the aim of addressing the optimization of a design domain suitable to split the continuous input motion from the alternating output motion, as previously stated, a rod-shaped

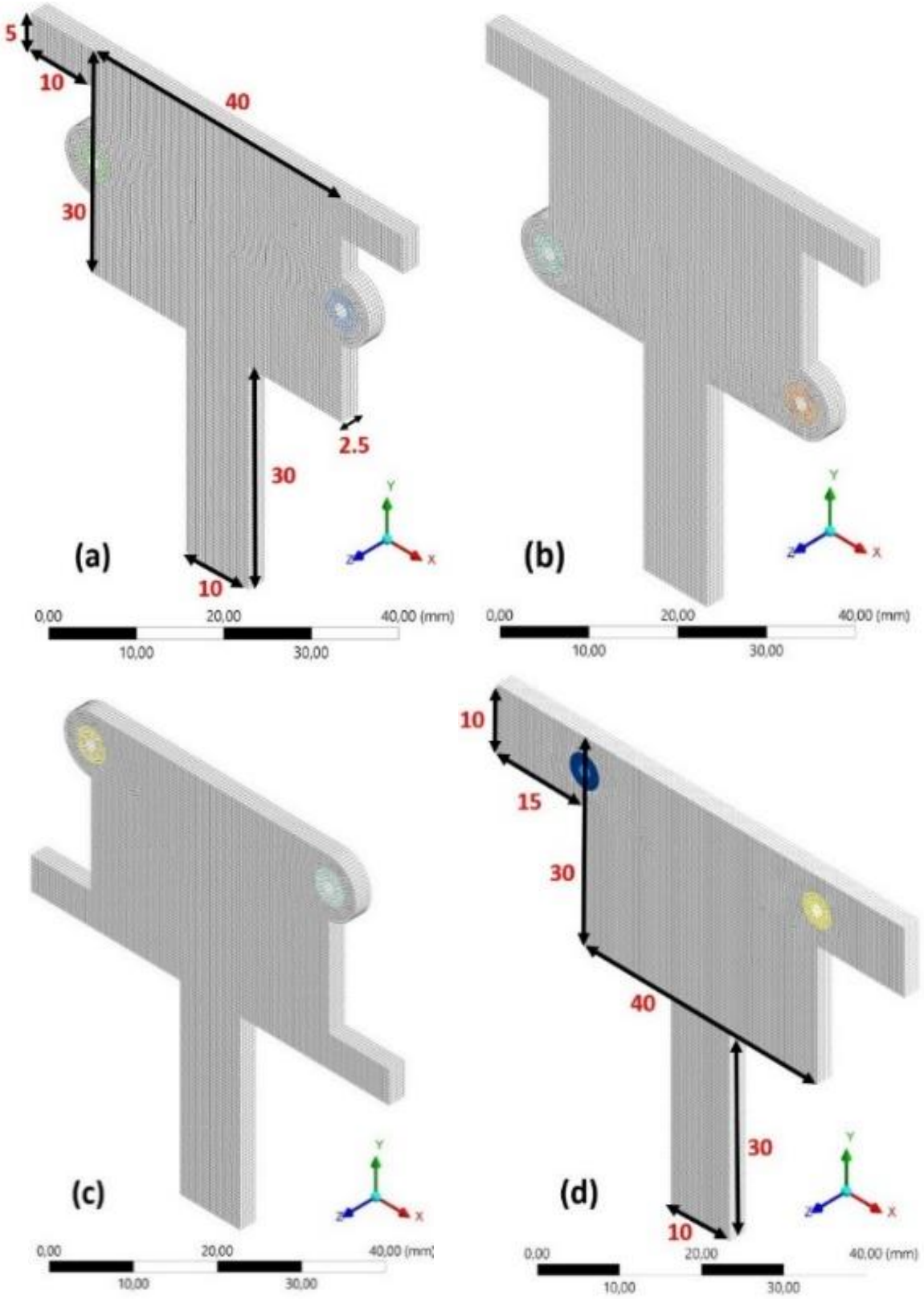

Figure 8.1. Meshed models of the four design domain analyzed with details of the main dimensions in mm [67]

rectangular area (measuring 10 x 30 mm) was incorporated into the lower regions of the models. Given the occurrence of large deformations, non-linear FEM analyses were conducted to correctly take into account the effects arising from changes in the structure's stiffness. Preliminarly to the topology optimization analysis, for each design domain three distinct FEA were carried out, each one with a different loading condition. The three load cases were indeed separately applied in order to simulate the rotary input motion of the electric motor: the first involved an upward-directed input displacement along the Y-axis, the second involved a downward-directed input displacement along the Y-axis, and the third involved a lateral displacement along the X-axis [67]. In Figure 8.2 are summarized the boundary conditions displaying the directions of input displacements of the three load cases. To simplify, only the design domain “a” was reported here for representative purpose, although the same boundary conditions were applied also to all other design domains.

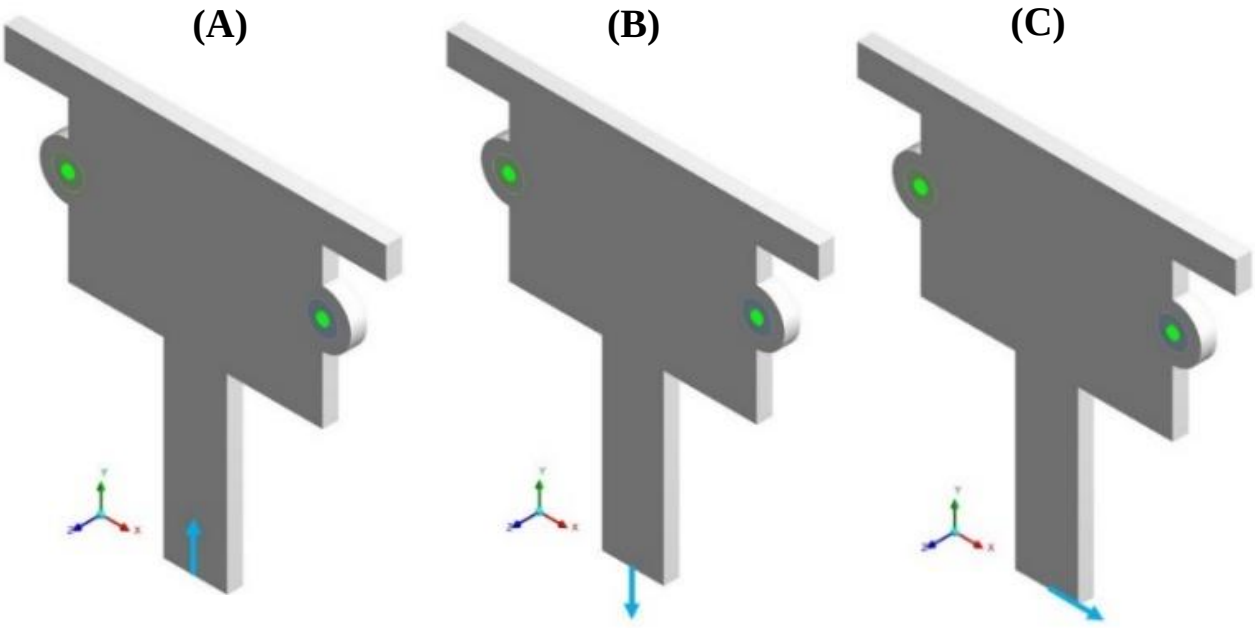

Figure 8.2. Boundary conditions separately applied three load cases: upward input displacement (A), downward input displacement (B), sideward input displacement (C)

Cylindrical supports were introduced correspondingly to the internal surfaces of the bearings (green coloured) to avoid the displacements along the X and Y directions and at the same time enabling the rotation around the Z-axis in these areas. As before mentioned, a flapping frequency of 25 Hz has been imposed as target for the compliant actuation mechanism. Therefore, considering that a full crank rotation spans a total duration of 0.04 seconds, each of the three load cases depicted in Figure 8.2 has a duration of 0.01 seconds. This duration is related to the conceptual splitting of the continuous rotary input motion into two distinct and alternating orthogonal linear input motions along the X and Y axes. A schematized representation of this conceptual splitting is reported in Fig.8.3. This subdivision strategy is implemented with the intention of separating the input motion specifically along the X direction, in such a way as to not influencing the output wing rotation. Indeed, the goal is to transmit to the CM solely the input motion coming from the DC motor into the Y direction, in order to drive the wing's flapping motions. Actually, since the rotation of the crank considered along the X axis is unsymmetrical regarding to the wing's required motion, this would likewise lead to an unsymmetrical rotation of the wings.

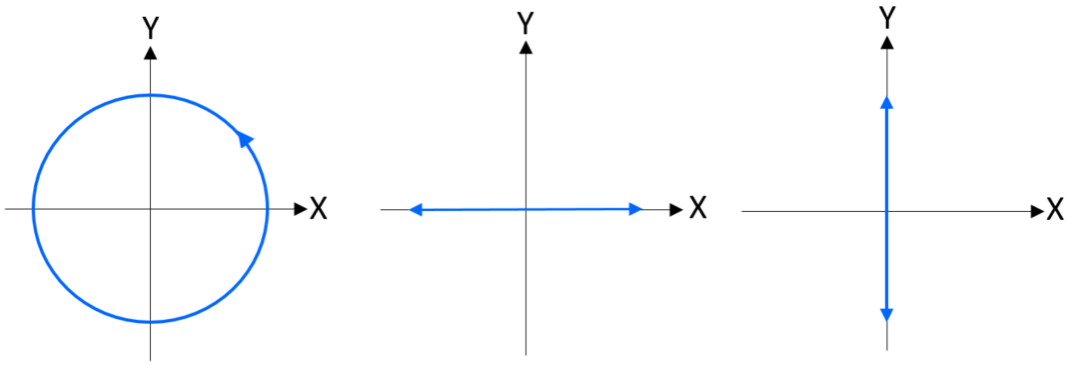

Figure 8.3. Conceptual splitting of the continuous rotary input motion coming from from DC motor in two separate and alternating orthogonal linear motions in X and Y

For the sake of clarity, in Figure 8.4 is reported a simplified graph showing an overview of the connections between the consecutive stages required to perform the optimization process, along with some details of each stage.

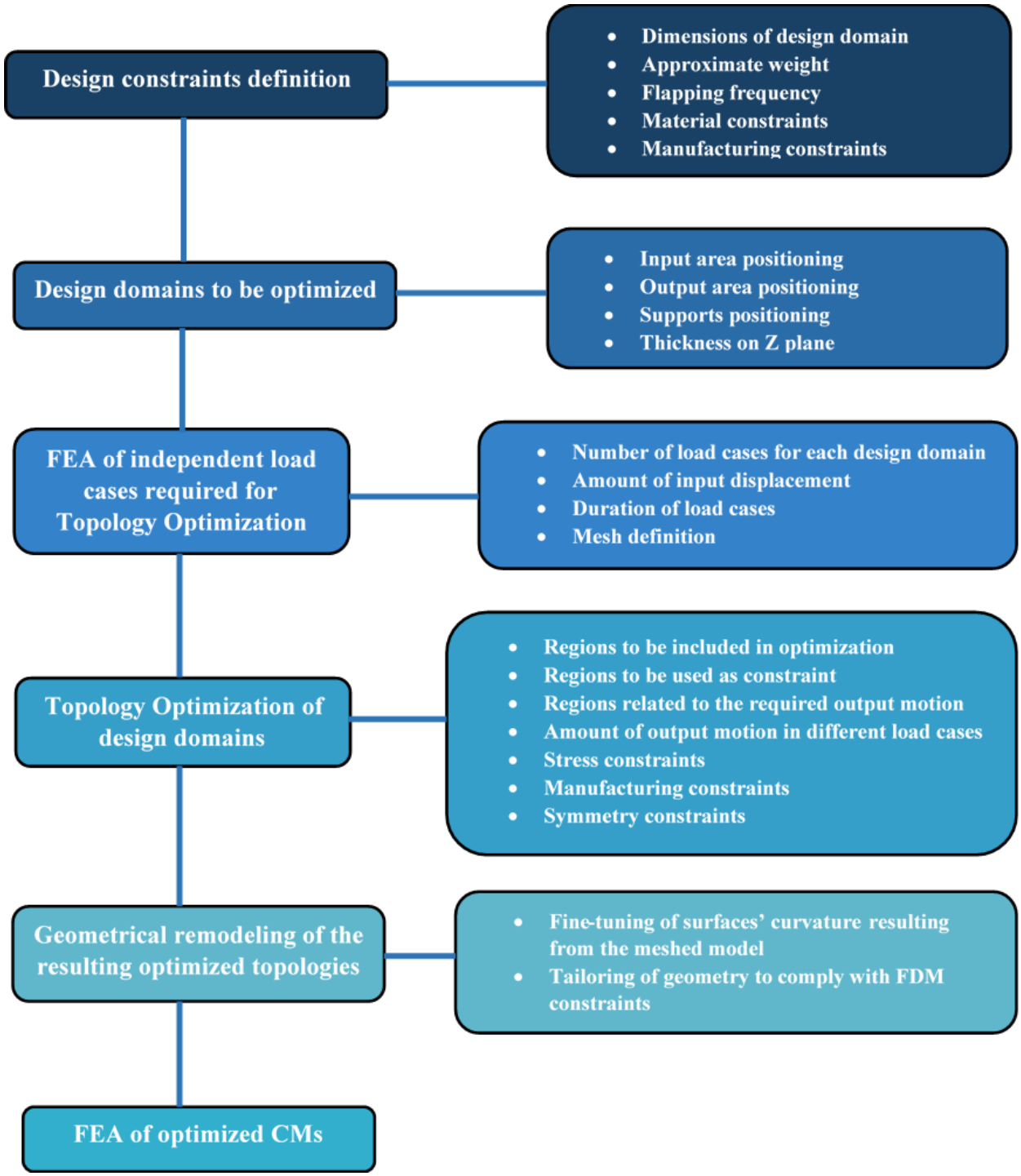

Figure 8.4. Schematic overview of the consecutive stages required to perform the optimization process.

As shown in Fig.8.4, before TO, when performing the FEA of the independent load cases (shown in Fig. 8.2), it's also necessary to define the amount of input displacement to be applied in each of the three load cases. With the aim to explore a broder range of CM's behaviour, several amounts of input displacements were applied for each load case shown in Fig.8.2, whose intensities in mm are reported below in Table 8.1.

Design domain	**a**				**b**			**c**			**d**		
Input displacement [mm]	2	3	4	5	2	4	5	4	6	8	4	6	8

Table 8.1. Overview of the different input displacements applied in each load case represented in Figure 8.2.

These displacement's values were therefore applied in the same direction shown in Figure 8.2. Once carried out the FEA of these three load cases, for each design domain and using the displacement values shown above, it was possible to proceed with the next phase related to the definition of topology optimization regions, which are described in Figure 8.5.

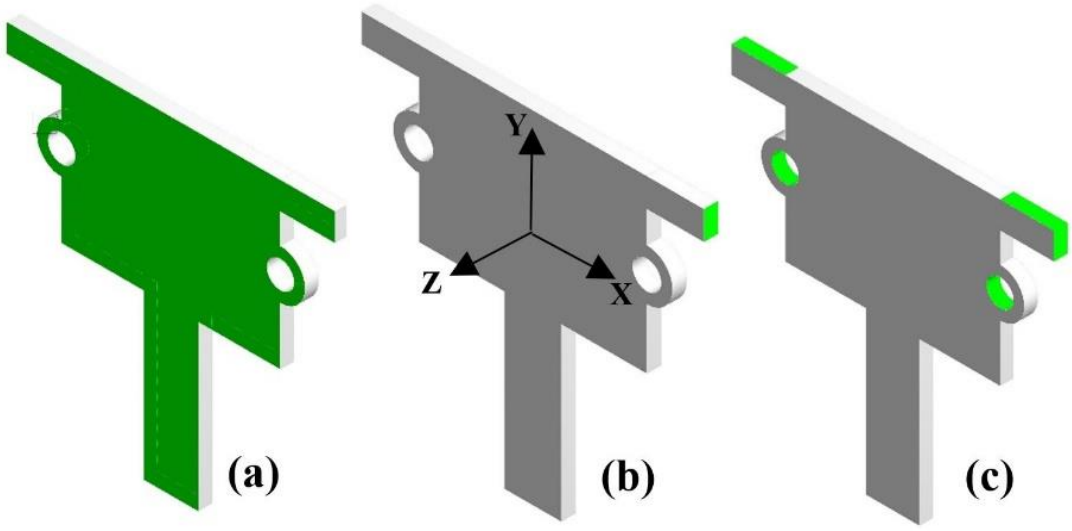

Figure 8.5. Topology regions regarding to: the Z displacement prevented (a), related to the wings' output displacement (b), excluded from optimization process (c).

Also in this case, for the sake of simplicity only the topology regions for the design domain “a” were represented, although the same conditions were considered likewise for all the design domains. Topology optimization analyses were implemented setting the mass minimization as the objective function for each design domain, considering the input displacements and the output displacement constraints described following. Aiming to prevent buckling effects, the maximum displacement permitted along the Z-axis was established equal to zero on two opposing faces of the model (as shown in Figure 8.5a), which are parallel to the XY plane. The output displacements constraints have been applied to the areas shown in Fig. 8.5b, where the motion of the two wings have to be executed. The displacement of these two specific areas was imposed to be equal to zero in correspondence of the load case C (Fig. 8.2c) with the purpose of decoupling the rotary input motion along the X-direction from the output rotation of the wings. Consequently, throughout the crank rotation, only the input displacement in the Y-direction can be transferred to the wings, resulting in the creation of the required alternating symmetrical rotational output movement. The significance of this motion decoupling lies in the necessity for symmetry in flapping angles between the two wings during FWMAVs' flight. This ensures that both rotating wings ideally maintain the same angle with respect to the X-axis at any given moment throughout a complete flapping cycle. On the other hand, the output displacements of the two wings have to be necessarily different from zero in correspondence of the load cases A and B (Fig. 8.2a, b) since in these load cases the input motion in the Y axis have to be completely transferred to the flapping motion. Indeed, the output displacements

imposed in the topology regions in Fig.8.5b, have been applied only in correspondence of the load cases A and B (Fig.8.2 a, b), while in load case C the output displacement was set equal to zero. In the following Table 8.2 is reported an overview of the correspondence of all the output displacements imposed, regarding to each load case and each design domain.

Design domain	**a**				**b**		
Input displacement [mm]	2	3	4	5	2	4	5
Output displacement constraint [mm] on Y axis, related to Load case A	-5	-7.5	-10	-12.5	-5	-10	-16
Output displacement constraint [mm] on Y axis, related to Load case B	5	7.5	10	+12.5	5	10	16
Output displacement constraint [mm] on X and Y axis, related to Load case C	0				0		

Design domain	**c**			**d**		
Input displacement [mm]	4	6	8	4	6	8
Output displacement constraint [mm] on Y axis, related to Load case A	-10	-15	-17.5	-10	-15	-17.5
Output displacement constraint [mm] on Y axis, related to Load case B	10	15	+17.5	10	15	+17.5
Output displacement constraint [mm] on X and Y axis, related to Load case C	0			0		

Table 8.2. Overview of the correspondence of all the output displacements imposed, regarding to each load case and each design domain

As the input displacement is increased, also the corresponding output displacement imposed becomes higher, in order to asses the behaviour of the CM in a range of various displacement conditions. Figure 8.5c illustrates the regions omitted from the topology optimization process since they are assigned to accommodate the connections of the CM with the wings and the low-friction bearings. Additionally, a stress constraint was also considered in the TO process, establishing the maximum allowable stress at 70% of the material's tensile strength. From some preliminary optimization analyses it was observed that setting lower values of allowable stress proves to be ineffective, since the optimization process exhibits convergence issues, therefore a balance value was chosen. Anyway, since a geometry remodeling of the optimized results is certainly required, the areas where high stress concentrations are expected have been consequently remodeled to avoid stress peaks. Finally, manufacturing constraints were also incorporated, including aspects such as ensuring symmetry of the optimized topologies about the YZ plane and complying with the additive manufacturing building direction along the Z-axis. The topology results obtained from the optimization of each domain are depicted in Figures 8.6 and 8.7. It can be seen that as the input displacement progressively increases, different geometric details become successively observable within each of the four design domains, defining in a more clear way the mechanism. In particular, it can be noted that, the less demanding operating conditions, that occur when imposing lower input and output displacements, lead to the generation of thinner cross-sections, suggesting that the material could withstand such a functioning also with this geometrical features.

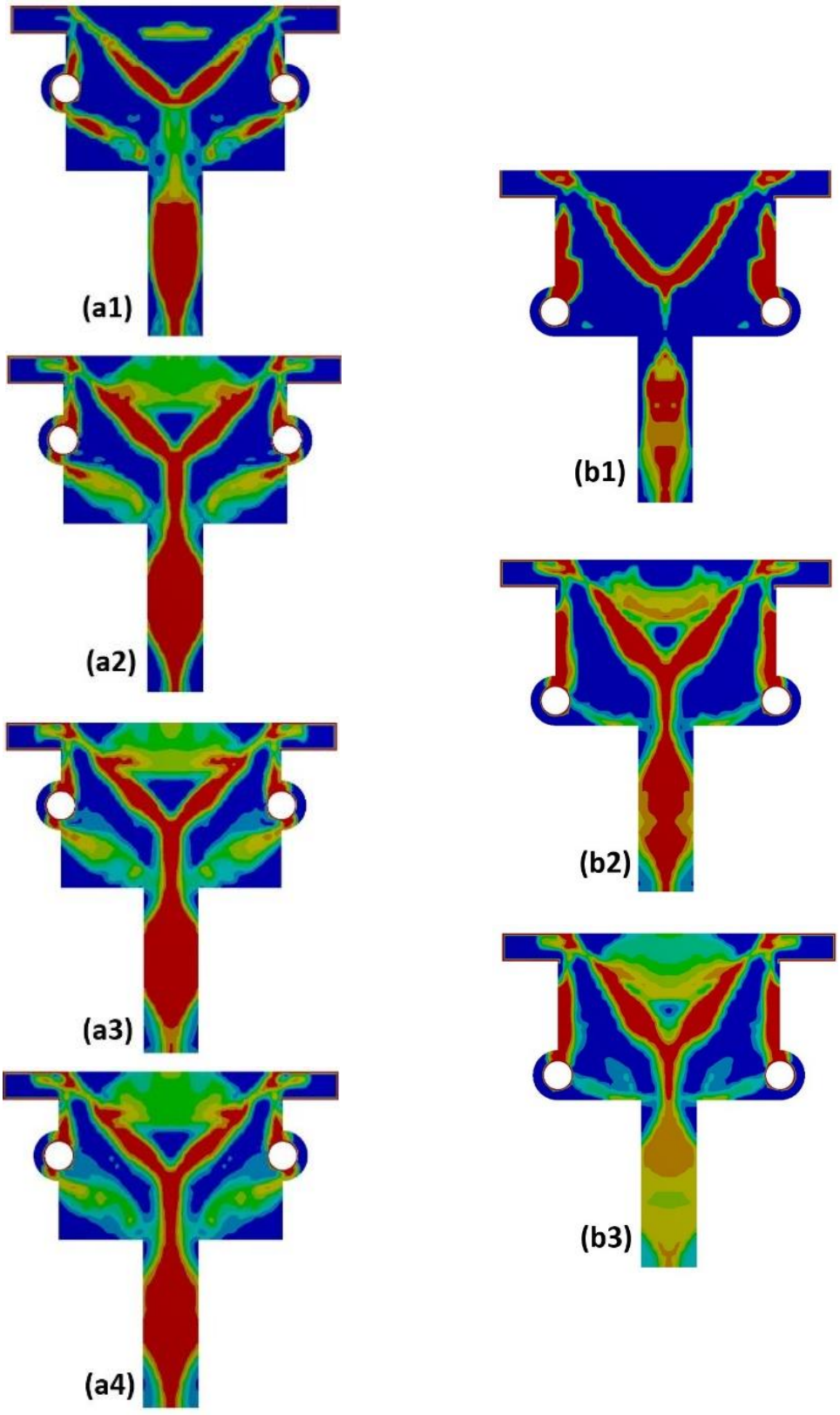

Figure 8.6. Topology optimization results for design domain a and b, each one reported with its specific input displacement in ascending order: Design domain a (2, 3, 4, 5 mm), Design domain b (2, 4, 5, mm).

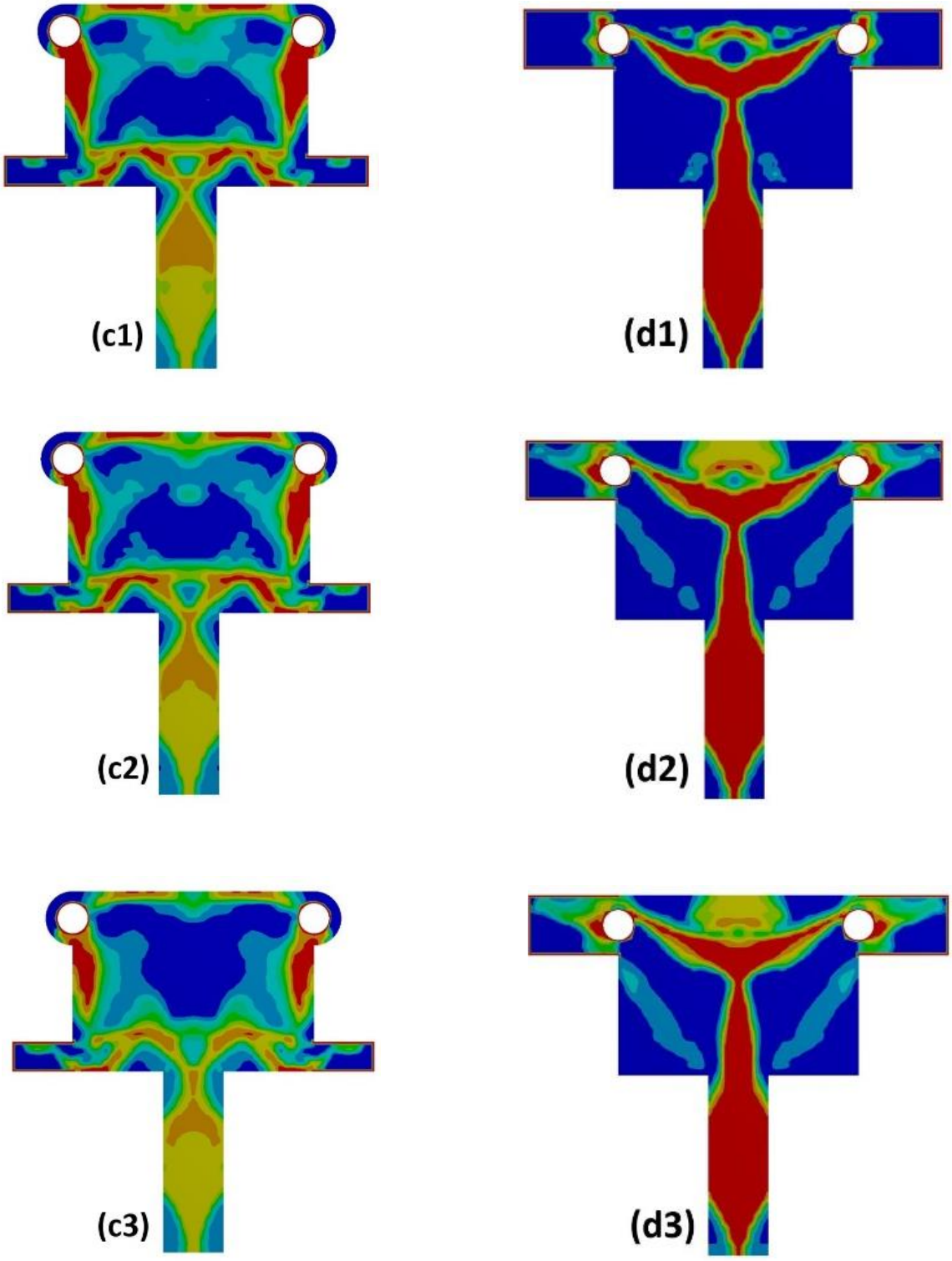

Figure 8.7. Topology optimization results for design domain c and d, each one reported with its specific input displacement in ascending order : Design domain c (4, 6, 8 mm), Design domain d (4, 6, 8 mm).

Instead, when more substantial input and output displacements are taken into account through the optimization process, the cross-sections' thickness become progressively thicker, recommending therefore the need of more material in order to endure the stress arising from a more challenging operating condition. Moreover, in some design domains it can be also observed the formation of new regions of material when greater displacements are imposed, as it happens in the case of domain a, b and d, where a new formation of material is observable in the upper area of the design domain. Taking into consideration the differences from the various results and appropriately combining the optimization outcomes, four Compliant Mechanism layouts were remodeled, one for each design domain. This process also supported the prerequisite of complying with the FDM manufacturing constraint concerning the limit of 1 mm of thickness for the flexible areas. The performances of the four remodeled layouts were investigated through non-linear transient Fem analysis in terms of stresses and wing rotation angles. Following are reported the geometries of the four remodeled layouts, together with the stress maps of CMs in their configuration of upstroke, downstroke and central position of the wings. The meshing of the model, also shown along with the geometries and FEA result of each design domain, was developed so as to provide a mininum number of three elements along the smallest cross-sections. The dimension of the crank connected to the DC motor has been differently defined in the four layouts, on the basis of the input and output displacements defined in Table 8.2. In particular, the crank assumes a length of 5 mm the layout "a", and 8 mm on layouts "b", "c", "d".

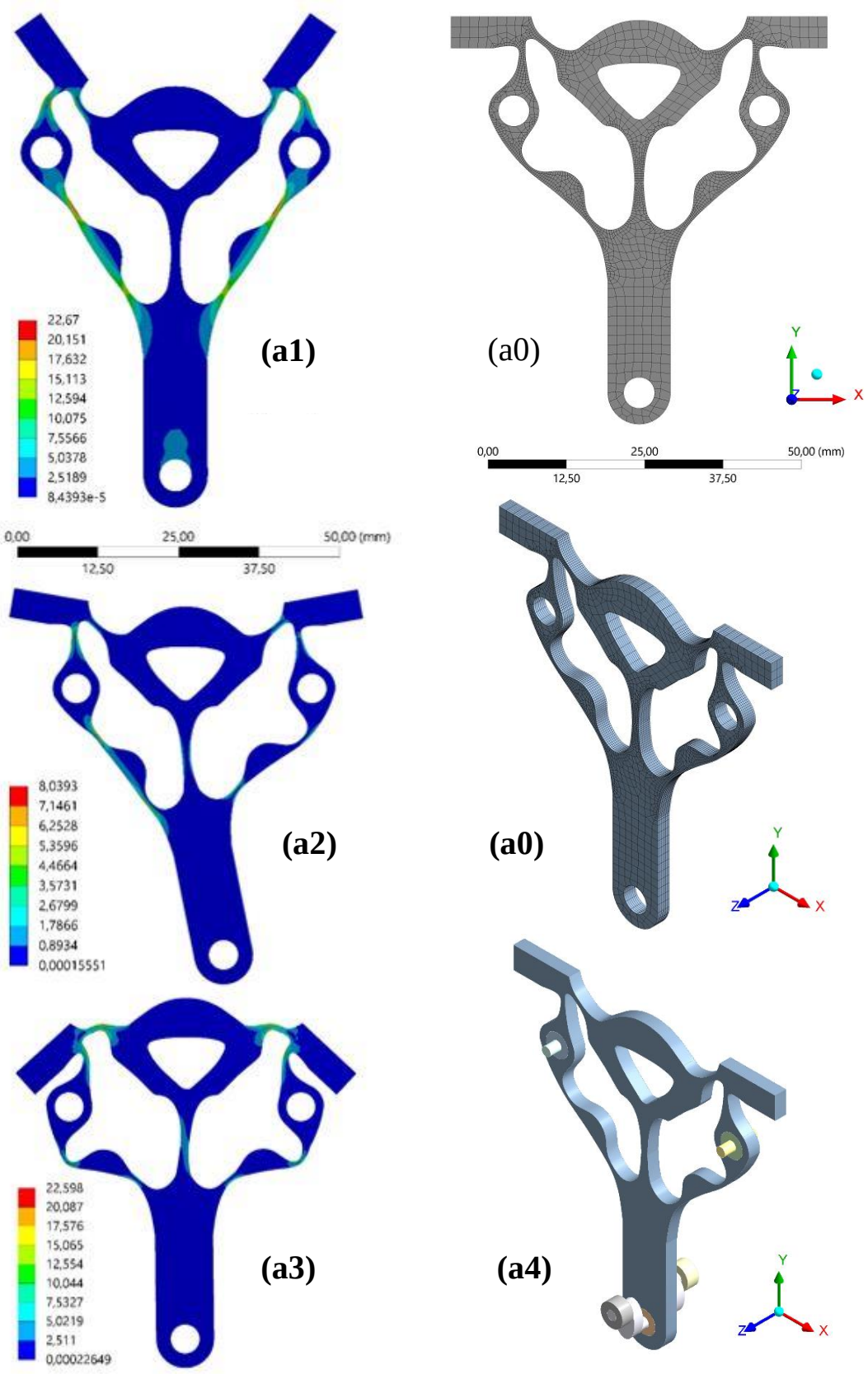

Figure 8.8. Layout 1, resulting from the remodeling of TO results for design domain "a": meshed model (a0), wings in upward configuration (a1), central position (a2) downward position (a3) and model with crank and supports (a4)

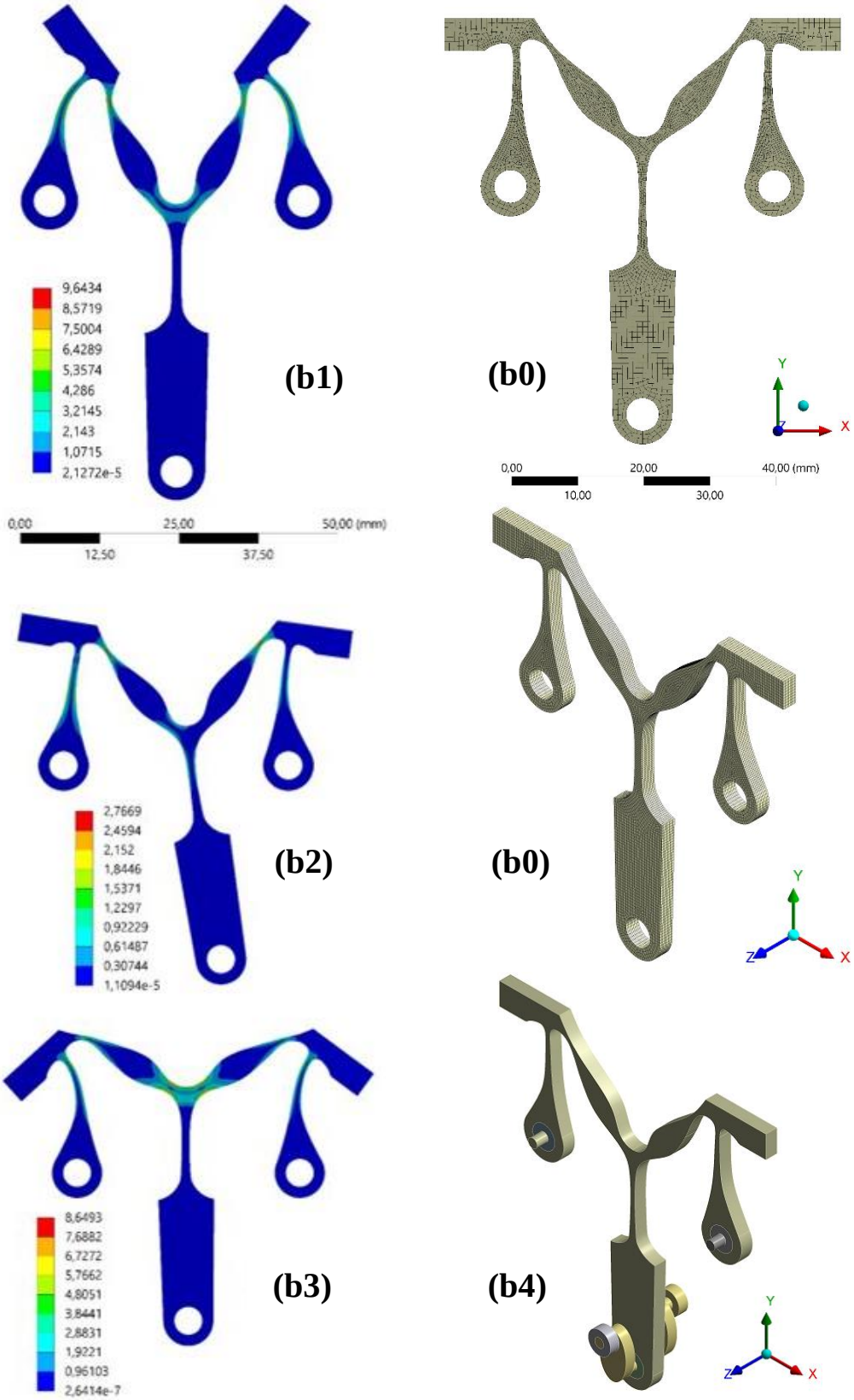

Figure 8.9. Layout 2, resulting from the remodeling of TO results for design domain "b": meshed model (b0), wings in upward configuration (b1), central position (b2) downward position (b3) and model with crank and supports (b4)

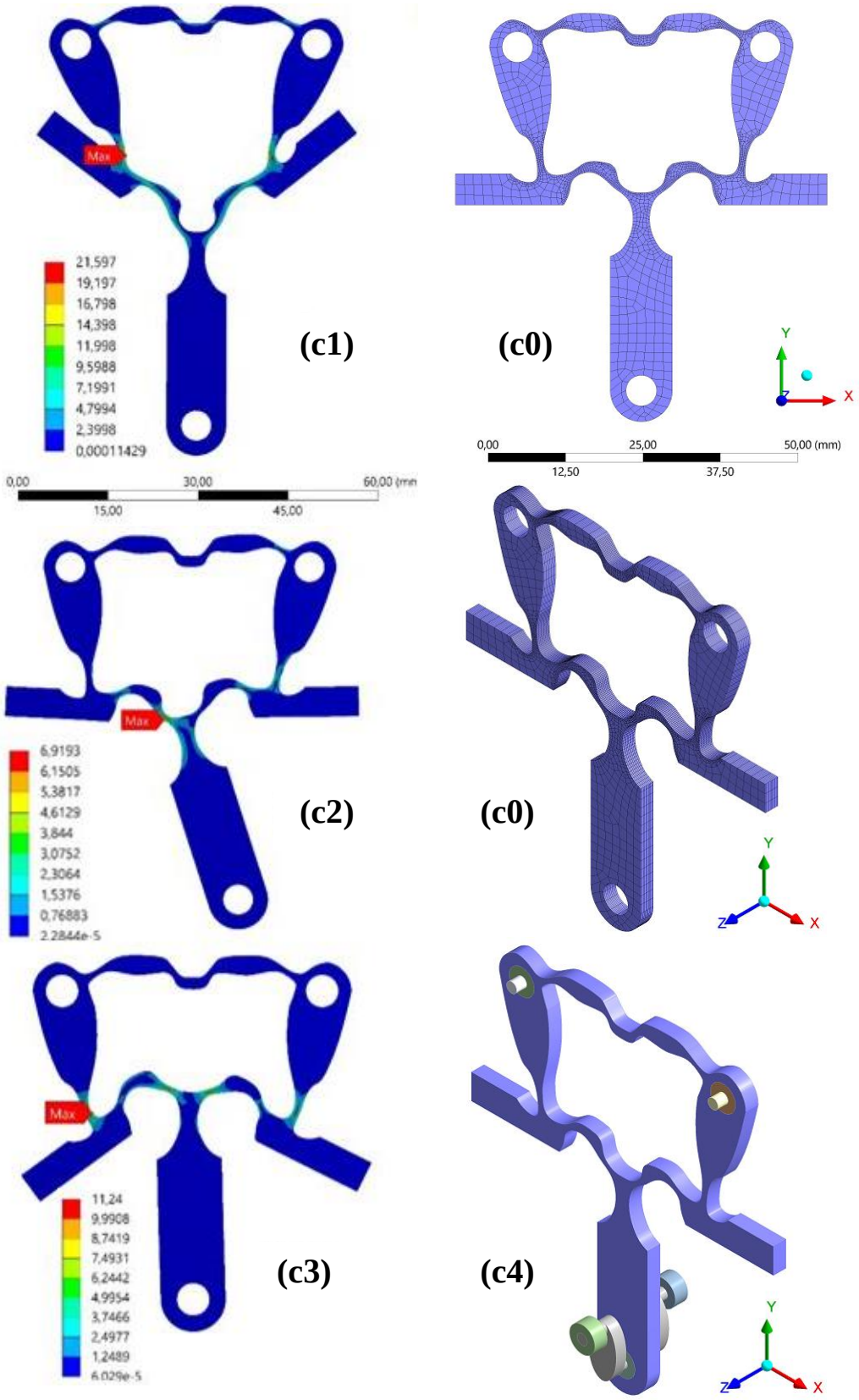

Figure 8.10. Layout 3, resulting from the remodeling of TO results for design domain "c": meshed model (c0), wings in upward configuration (c1), central position (c2) downward position (c3) and model with crank and supports (c4)

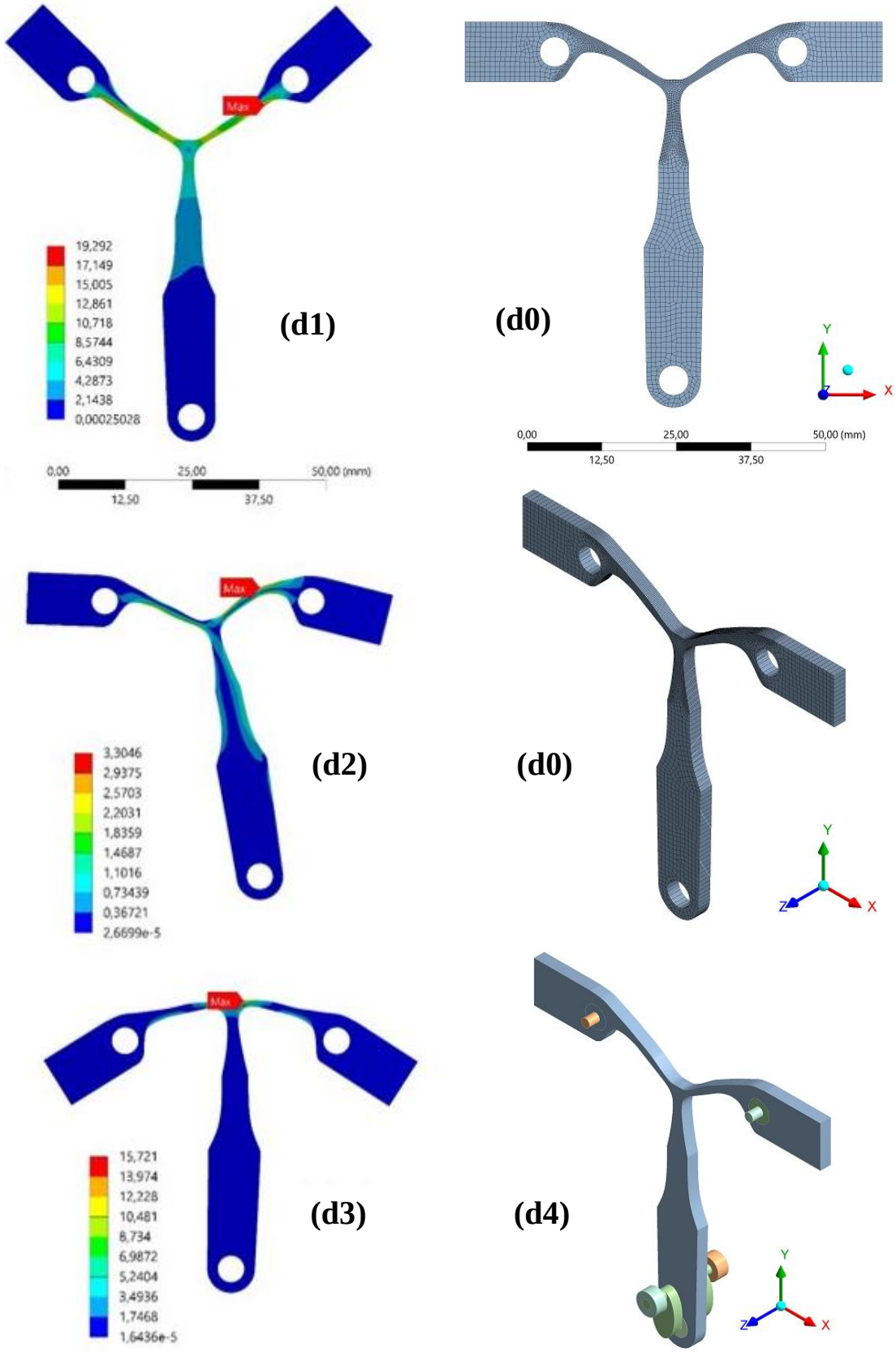

Figure 8.11. Layout 4, resulting from the remodeling of TO results for design domain "d": meshed model (d0), wings in upward configuration (d1), central position (d2) downward position (d3) and model with crank and supports (d4)

Since the non-linear FEA have to take into consideration both large displacements and high frequency motions occurring within thin flexible structures, the elements' mininum dimension (as reported below in Table 8.3) was refined and appropriately set so as to avoid non-convergence issues due to elements' excessive distortion or arising of stress concentration points.

CM layout	a	b	c	d
Minimum dimension of element	0,3	0,3	0,25	0,2
Total elements in meshed model	21000	46700	25000	45000

Table 8.3. Details on mesh minimum dimension and total amount of elements in each model

A geometry including crank and supports is also represented above for each model. When setting the transient analyses, the input displacement transmitted through the crank rotation was separated into five load steps (indicated by distinct colors in Figure 8.12), each lasting for 0.01 seconds.

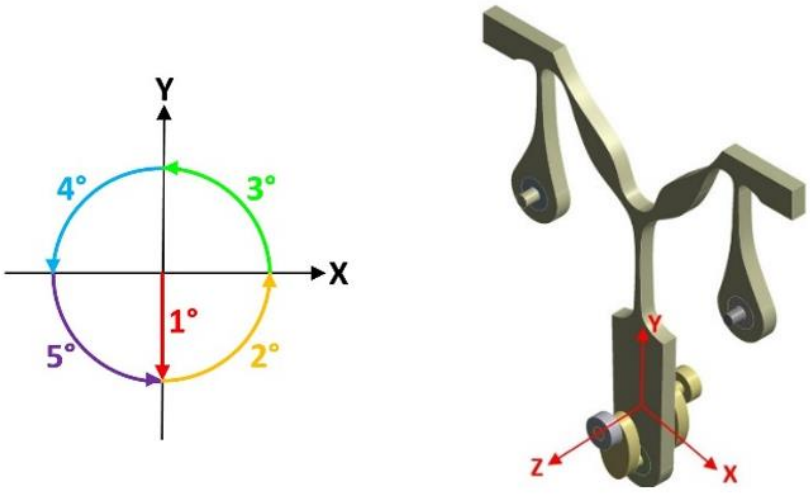

Figure 8.12. Schematization of input motion imposed for each load step and laterally the layout "b" represented for explanatory purpose with the global coordinate system.

The initial load step (highlighted with 1° on the left side of Fig. 8.12) takes place solely at the starting of the initial flapping sequence, which is composed of the load steps ranging from 2° to 5°. It was essential to introduce this initial load step in such a way as to start the rotation from the position where the wing angle is at its maximum (referred to the upward configuration a1, b1, c1 and d2, respectively represented in Fig 8.8, 8.9, 8.10 and 8.11). This specifically happens when the crank reaches the lowest point along the Y-axis, as illustrated in Figure 8.12. After carrying out transient FEA of the four layouts, several results were extracted regarding both the stress and the wing's rotations. To better examine results, a table is provided below containing a comprehensive comparison of the CMs' performances.

Layout	Weight [g]	Weight reduction %	Overall wing rotation angle [°]	Maximum wings'angle deviation [°]
a	2.56	44.7	103	13
b	1.95	57.8	106	21
c	2.32	49.9	83	28
d	2.10	58	85	23

Layout	Maximum Von Mises Stress [MPa]	Stress at maximum rotation angle [MPa]	Stress at minimum rotation angle [MPa]	Stress in central position [MPa]
a	23.4	22.7	22.6	8
b	10.3	9.6	8.6	2.7
c	21	21.6	11.2	6.9
d	18.6	19.3	15.7	3.3

Table 8.4. Comparison of the FEA results of the four CMs layouts.

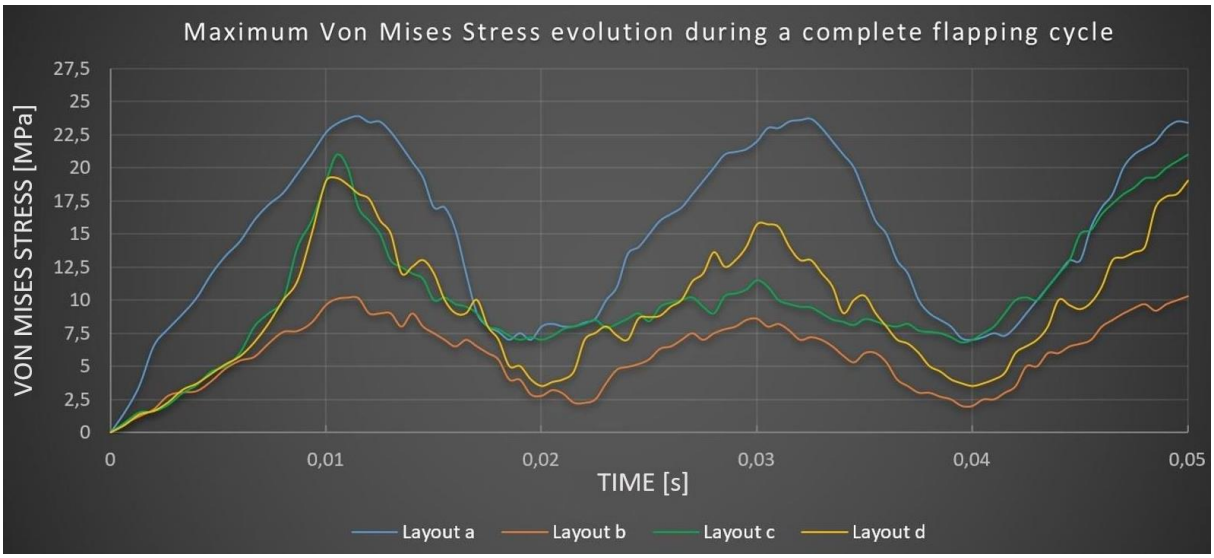

Figure 8.13. Overview of the evoultion of Maximum Von Mises stress throughout a complete flapping cycle, compared for the four CMs layouts [67]

A graph representing the stress trends of the CMs is also reported in Figure 8.13, displaying the fluctuation of stress throughout a complete flapping cycle. The influence of inertial effects resulting from the high frequency displacements is observable above for all the layouts, where a distinct wave-like pattern in stress trends becomes apparent. The highest stress peaks emerge close to the positions where the rotation angle is at its maximum. This behaviour could have been expected actually considering that the worst load conditions are experienced from the CMs during the motion inversion. Indeed the inertial effects due to the masses become more evident especially a few moments after that the wings reach the maximum upward and downward configurations. Instead, when the wings are in central position (images a2, b2, c2 and d2 depicted above) altough the masses in motion achieve the highest speed, they are not subjected to the highest acceleration, which is reached in the conditions of motion inversion.

The mininum stresses are therefore reached when the area of input motion (i.e. the crank connection with the CM) is located in the maximum and minimum points along the x axis. Since the maximum angular difference of the two wings throughout the entire flapping cycle ranges between 13° and 28°, is fairly reached the intention of decoupling the continuous rotary input motion of an electric motor from the alternating symmetrical rotational output movement. Moreover, the symmetry of flapping motion has been produced during the major part of flapping cycle, as shown from the previous FEA results, suggesting the potentiality of applying such design process to the development of 3D printable monolithic actuation CMs for FWMAVs. The presented outcomes hold significance as all four planar CMs designed achieve overall wing rotation angles greather than 80° without experiencing buckling phenomena, despite maintaining a uniform thickness of 2.5 mm. Even if the stress trend remains below the material's tensile strength, further analyses are required to investigate the fatigue behaviour of the material, since no fatigue data are currently available. Nevertheless, since a uniform thickness of 2.5 mm has been only investigated in the present case, it can be hypotesized that exploiting a thicker layout, the stresses could be consequently deployed across a larger cross-section, so that a greater amount of material could withstand the operating conditions. Otherwise, as usually happens after a topology optimization process, a subsequent shape or parametric optimization process could be implemented after TO, so as to perform a more effective geometrical remodeling, progressively adjusting the shape of the mechanism and tailoring it to various operating or boundary conditions.

Moreover, a notable weight reduction could be observed, ranging from a minimum of 44% to a maximum of 58%, considering the weight of remodeled layouts compared to the corresponding initial design domains. In particular, the performance of layout b is remarkable, especially due to its consistently low stress trend throughout an entire flapping cycle and for achieving the highest overall wing rotation angle of 106°, besided of achieving almost a 58% of weight reduction. These promising outcomes aim to pave the way for future advancements in enhancing the TO of compliant actuation mechanisms of FWMAVs, allowing also an easing of their manufacturing using cost-effective 3D printing technologies. This involves delving further into fatigue concerns, integrating modal analyses with the topology optimization design aspects, and implementing size and shape optimization, also in order to foresee an adjustable geometry capable of performing flapping maneuvers. This design process, involving the optimization of several configurations of design domains, requires a certain amount of time and computational resources to be carried out. Since each design domain needs to be discretized using a meshed model, in this case exploiting a large number of solid elements (as show in Table 8.3), the identification of a more efficient process could be considered interesting. Indeed, the possibility of using shell elements has been considered as an opportunity both to implementing a less onerous design process from the computational point of view, and to enable the exploration of more design alternatives, affecting for instance various geometrical parameters of the initial design domains.

9. Topology Optimization of CMs: Shell elements FEA modeling and multistep optimization

With the purpose of further exploring the capabilities of the design approach described in the previous chapter, an alternative method was developed, whose main differences from before concern the phases dealing with FEA of independent load cases prior to TO and the optimization phase itself. Since the previous design process necessitates a considerable amount of time and computational resources, the following approach is addressed to simplify the overall design process, trying to achieve final layouts' performance at least comparable to the ones previously obtained. In particular, two main variations have been introduced from before:

- FEA models discretized using shell elements for all design domains;
- Multistep optimization approach for optimizing one design domain;

The choice of using shell elements is related to their property to be computationally lighter to be implemented in FEA than solid elements, therefore leading to a less time-consuming analysis. Instead, the conceiving of a multistep approach arises from some observations involving the optimization phase. Basically, since these CMs are intended to withstand large displacements performed at high frequencies within a monolithic structure, the final layout achievable is strictly correlated both to the initial design domain and to the boundary conditions imposed. The latter include

the input displacement, the supports' positioning and likewise the output displacements required. Considering for instance the use of an initial meshed design domain, with a certain amount of elements defined with the appropriate material properties and a series of boundary conditions. Since the optimization process determines a specific topology related to an initial compact design domain with generic geometrical features, imposing all at once high demanding operating conditions, such as large displacements at high frequencies, could negatively affect the potential performances of the final layout. Indeed, since the meshed model and the boundary conditions remain the same throughout the entire optimization process, the highly flexible areas of the mechanism affected by inertial effects and stress concentrations could potentially benefit from an intermediate geometrical remodeling of the design domain, during the TO process. Taking advantage of a TO separated in different optimization steps, using therefore different design domains, could be helpful not only to locally improve the mesh quality in the most flexible regions, but especially to effectively address the optimization in these regions. Indeed by remodeling these areas so as to more evenly distribute the deformations could result in a more accurately detailed topology of the monolithic CM. The four design domains considered for the optimization are depicted below in Figure 9.1 and Figure 9.2. As noted above, only one design domain has been optimized using a multistep approach (layout d1 in Fig. 9.2) in order to assess the capabilities of this approach comparing the final performance of its layout with the other ones, since a shell meshed model has been defined for all the design domains.

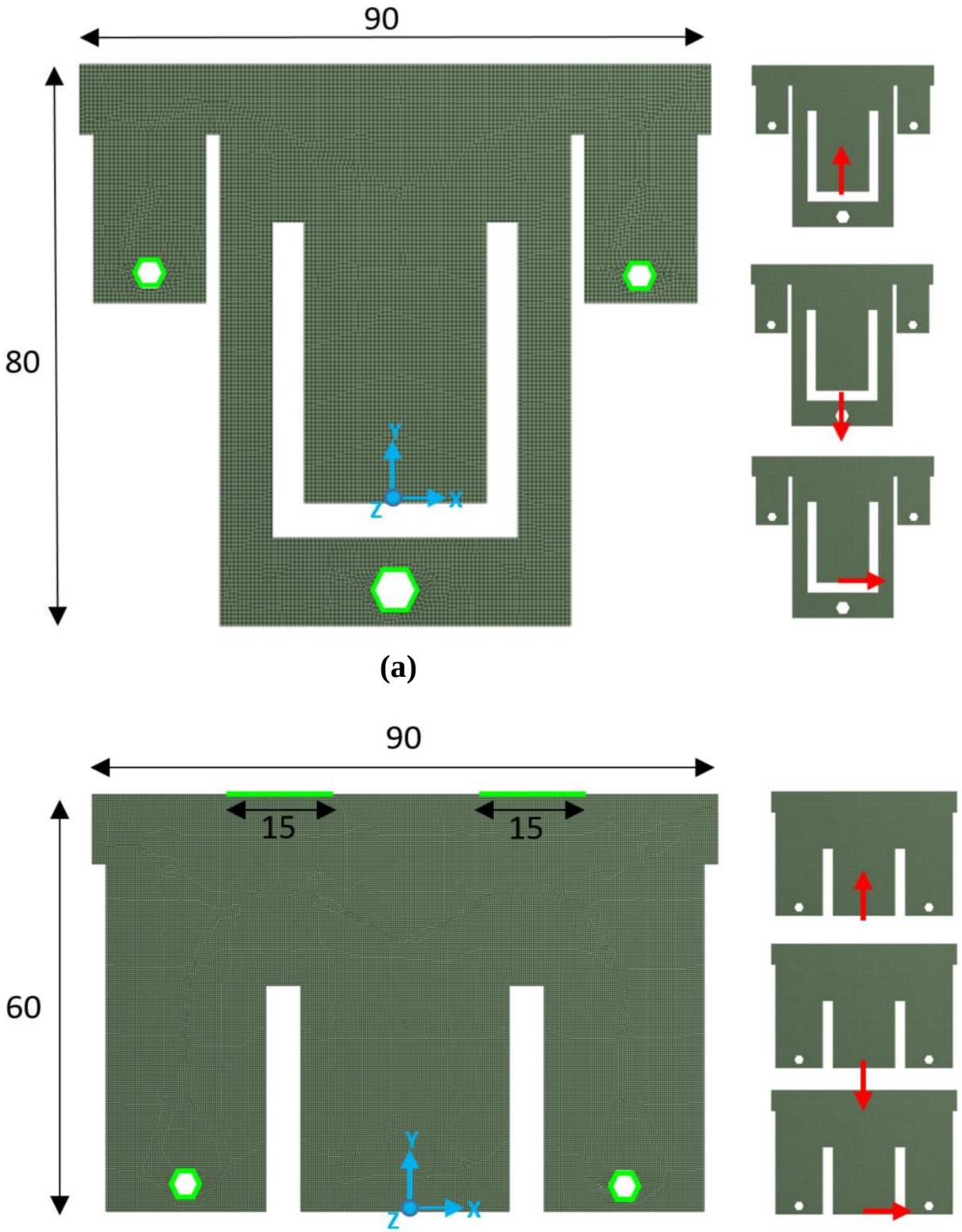

Figure 9.1. Meshed models of the design domain a and b, with details of the main dimensions in mm

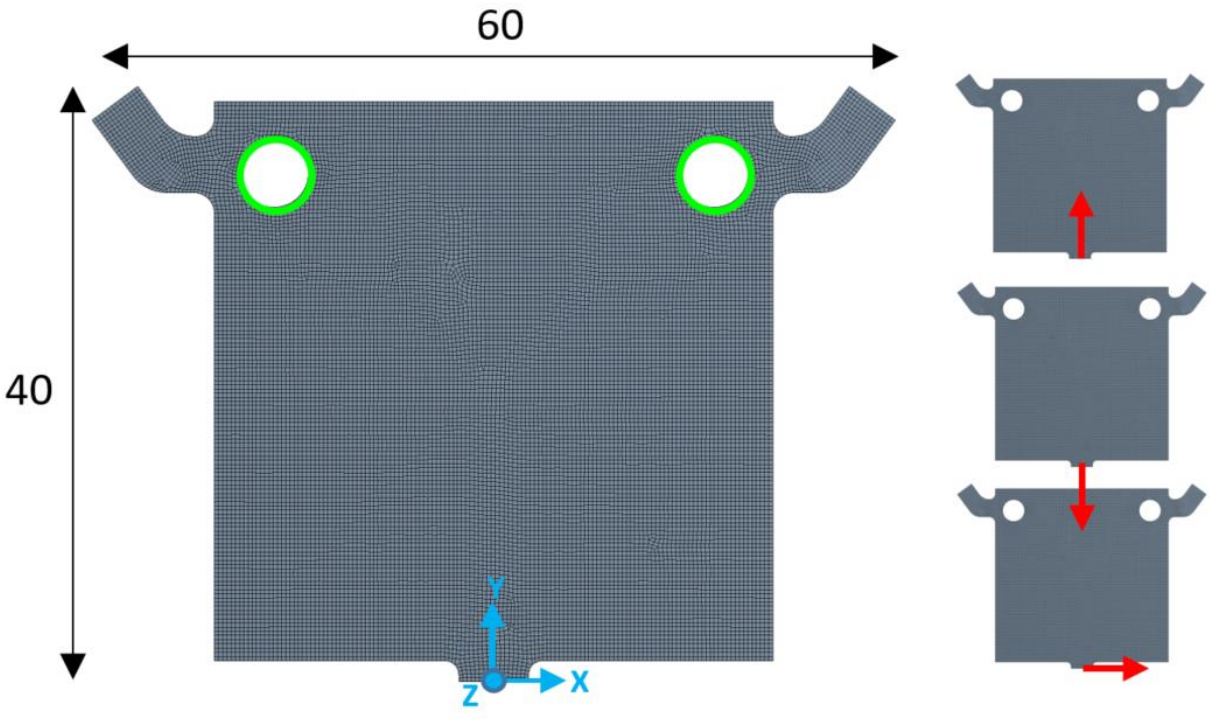

(c)

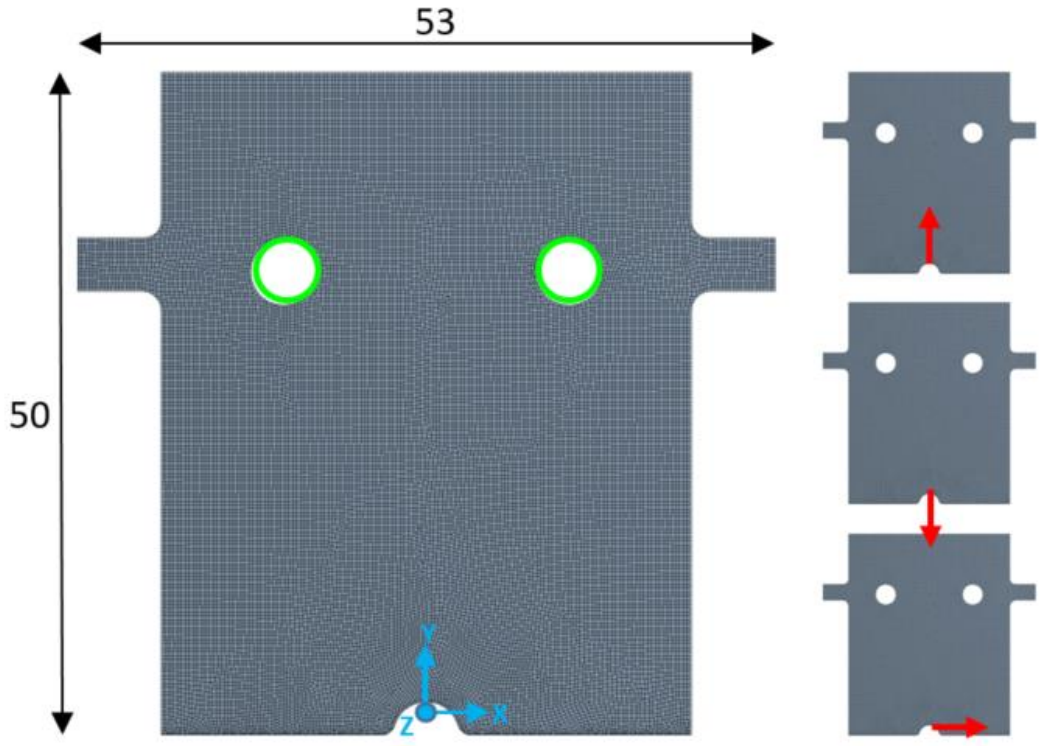

(d1)

Figure 9.2. Meshed models of the design domain c and d1, with details of the main dimensions in mm

The schematic overview explaining the design process is the same shown in Figure 8.4. Also in these optimizations, considering existing FWMAVs and similarly to the previous developed mechanisms, a flapping frequency of 25 Hz was considered for the CMs' design. The meshed 3D models reported above have been all defined with quadratic shell elements, each one having eight nodes with six degrees of freedom at each node, i.e. the translations and the rotations in x,y,z axes. A minimum dimension of 0,2 mm has been used for the elements. In Fig.9.1 the fixed supports have been highlighed in green, while for design domains c and d1 the green regions in Fig 9.2 are related to the introduction of low-friction bearing near to the wings. Laterally to the design domains are reported the three FEA independent load cases carried out prior to TO (equivalent to the load cases previously represented in Fig.8.2), where the red arrows represent the input displacement applied. Differently from the previous designs, in this approach have been also explored the optimization of design domains to which have been assigned different thicknesses. Indeed, the design domains a and b have been analyzed with two thicknesses, respectively of 4 or 6 and 3 or 6 mm. Also in this case, with the purpose to investigate a wider spectrum of CM's behaviours, various amounts of input displacements were employed for each depicted load case in Fig.9.1 and 9.2. The magnitudes of these displacements, measured in millimeters, are detailed below in Table 9.1. Considering the conceptual splitting of continuous rotary input motion into two distinct and alternating orthogonal linear input motions along the X and Y axes, as explained in Chapter 8 (Fig.8.3), a duration of 0,01 seconds has

Design Domain	a						b				
Thickness [mm]	4			6			3		6		
Input displacement [mm]	1,5	3	6	1,5	3	6	1,5	3	1,5	3	6

Design Domain	c		d1
Thickness [mm]	4		6
Input displacement [mm]	3	6	3

Table 9.1. Overview of the different input displacements applied for each thickness in each load case represented in Figure 9.1 and 9.2

been assigned to each FEA independent load case (Fig.9.1 and 9.2), also taking into account that a full crank rotation covers a total duration of 0.04 seconds. After carrying out the FEA for each design domain, with each thickness and input displacement, it was possible to focus on the subsequent phase involving the definition of topology optimization regions. In order to avoid buckling effects, a constraint was adopted where the maximum displacement allowed along the Z-axis was set to zero on two opposing faces of the model, as depicted in Figure 9.3 (a1, b1, c1 and d1.1), parallel to the XY plane. Constraints on output displacements were applied in the regions illustrated in Fig. 9.3 (a2, b2, c2 and d1.2), specifically where the motion of the two wings is intended to occur. Considering the load case where the input displacement is directed along the X axis, the corresponding boundary conditions in TO process has been imposed so as to have an output displacement of these specified areas equal to zero in this load case.

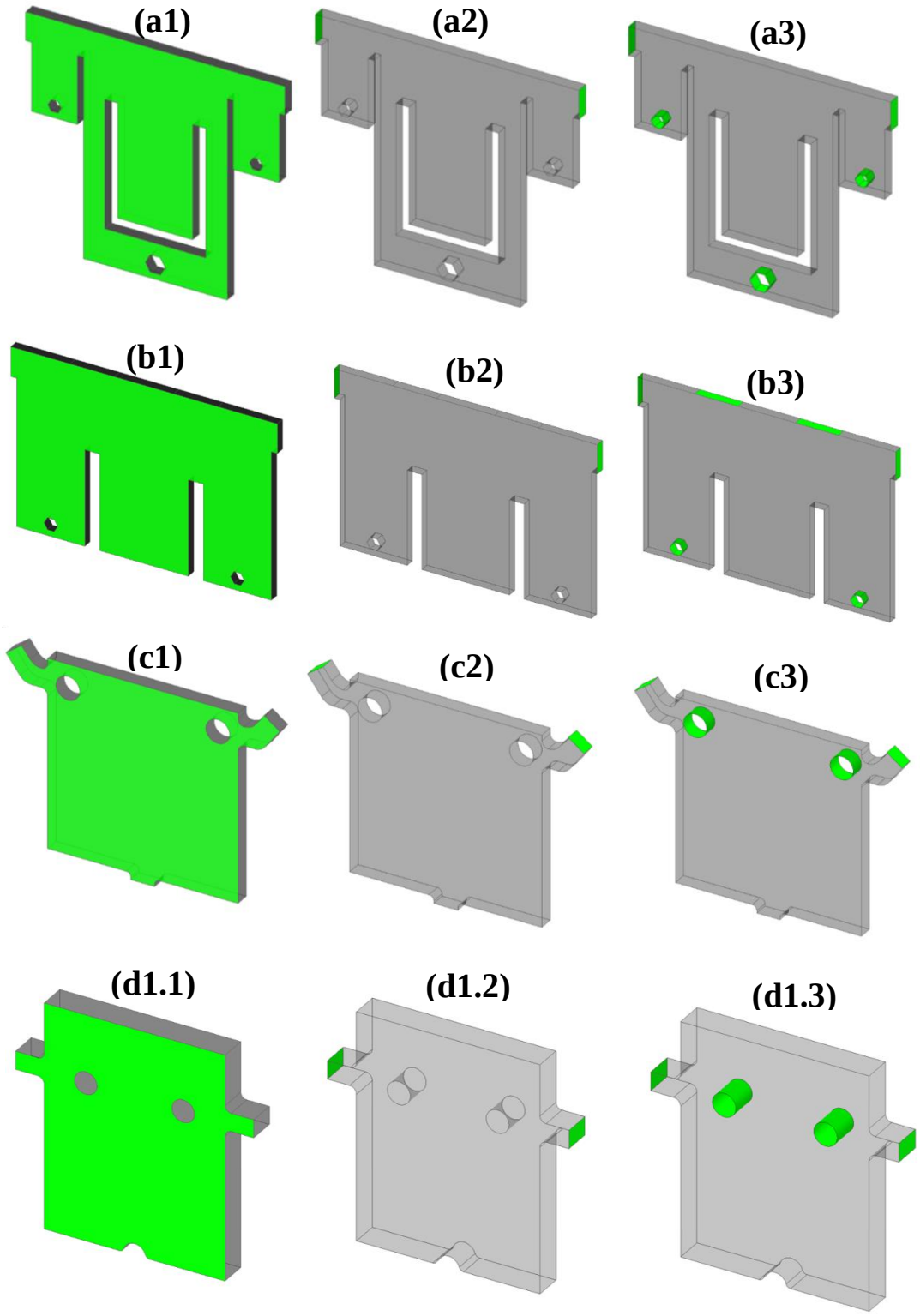

Figure 9.3. Topology regions regarding to: the Z displacement prevented (left figures), related to the wings' output displacement (central figures), excluded from optimization process (right figures).

This was implemented, as explained in chapter 8, in order to detach the rotary input motion along the X-direction from the output rotation of the wings. Therefore, only the input displacement in the Y-direction is transferred to the wings during crank's rotation, facilitating the creation of the required alternating symmetrical rotational output movement. Conversely, the output displacements of the two wings must inevitably differ from zero during the two load cases where the input displacement is directed along the Y axis. Indeed this input motion has to be entirely transferred to the flapping motion.

Design domain	a						b				
Thickness [mm]	4			6			3		6		
Input displacement [mm]	1,5	3	6	1,5	3	6	1,5	3	1,5	3	6
Output displacement constraint [mm] on Y axis, related to Load case A	-5	-10	-15	-5	-10	-15	-5	-10	-5	-10	-15
Output displacement constraint [mm] on Y axis, related to Load case B	5	10	15	5	10	15	5	10	5	10	15
Output displacement constraint [mm] on X and Y axis, related to Load case C	0						0		0		

Design domain	c		d1
Thickness [mm]	4		6
Input displacement [mm]	3	6	1,5
Output displacement constraint [mm] on Y axis, related to Load case A	-10	-15	-3
Output displacement constraint [mm] on Y axis, related to Load case B	10	15	3
Output displacement constraint [mm] on X and Y axis, related to Load case C	0		0

Table 9.2. Overview of the correspondence of all the displacements imposed, regarding to each load case for each design domain with all the analyzed thicknesses.

An overview of all the input displacements, along with the corresponding output displacements applied for each design domain and thickness, is reported above in Table 9.2. The images on the right in Fig.9.3 represent instead the topology regions excluded from the optimization procedure, as they are used for integrating the connections between the wings and the CM, for the fixed supports and the low-friction bearings. Also in this case, a stress constraint was taken into account setting the maximum admissible stress to 70% of material's tensile strenght, for the reasons previously explained in the optimization process in chapter 8. Ultimately, manufacturing constraints were also integrated, so as to foresee the symmetry of the optimized topologies concerning the YZ plane and considering the additive manufacturing build direction on the Z-axis. The topologies obtained from the TO process on the four design domain are reported below in Figures 9.4, 9.5 and 9.6. In particular it's possible to observ how the change of the thickness on the same design domain could affect the resulting distribution of material on the topology result. Indeed, considering design domain "a" and "b" with the same input displacement and different thicknesses, both the position and the shape of flexible regions turn out to be changed, as well as takes place also for the most rigid parts of the mechanism. As happened also before using solid elements within the design domains, under less demanding operational circumstances where lower input and output displacements are imposed, thinner cross-sections are generated, implying that also with thinner geometrical characteristics the material could endure such boundary conditions.

(a, Thickness 4mm, Input 1,5mm)

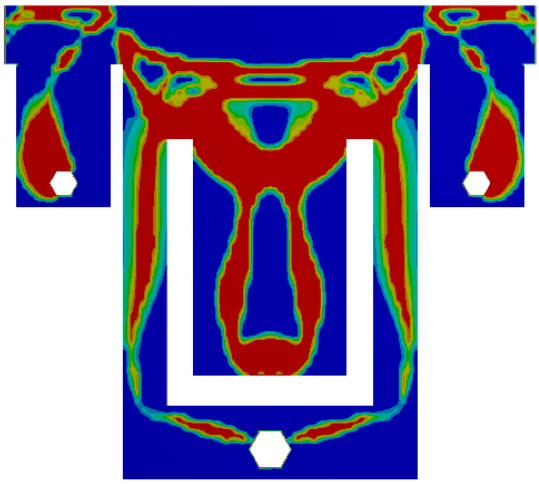

(a, Thickness 6mm, Input 1,5mm)

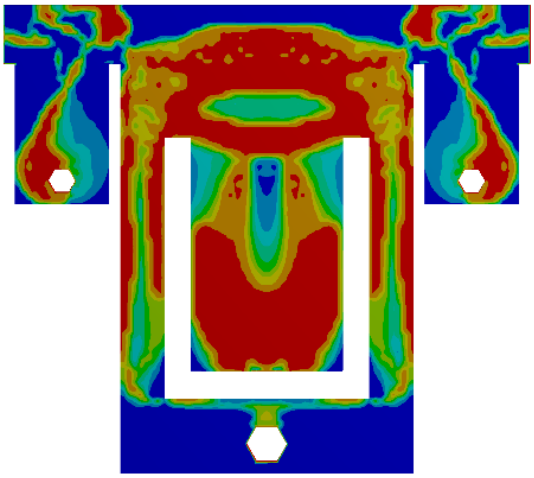

(a, Thickness 4mm, Input 3mm)

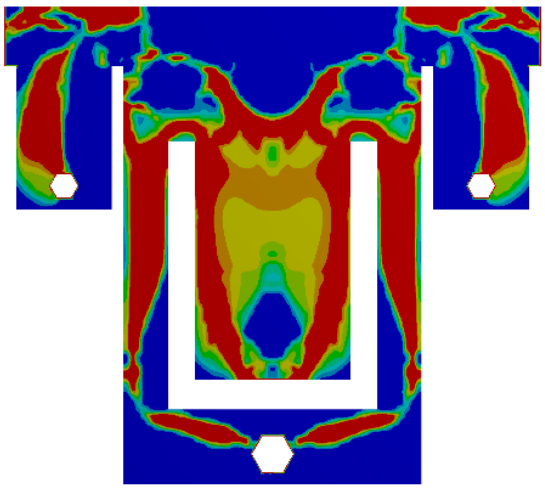

(a, Thickness 6mm, Input 3mm)

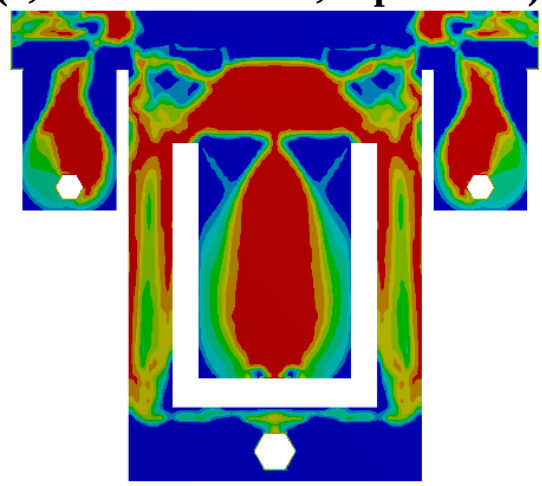

(a, Thickness 4mm, Input 6mm)

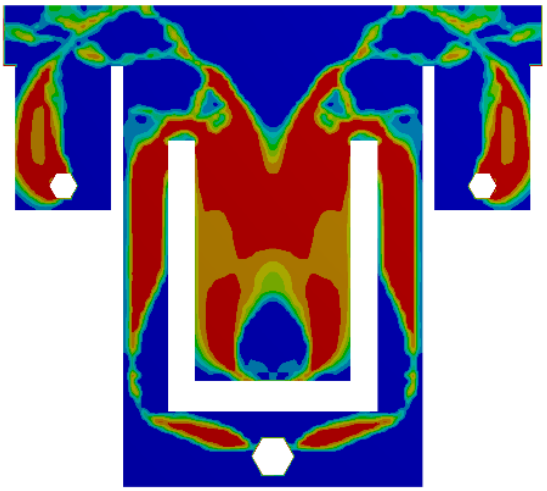

(a, Thickness 6mm, Input 6mm)

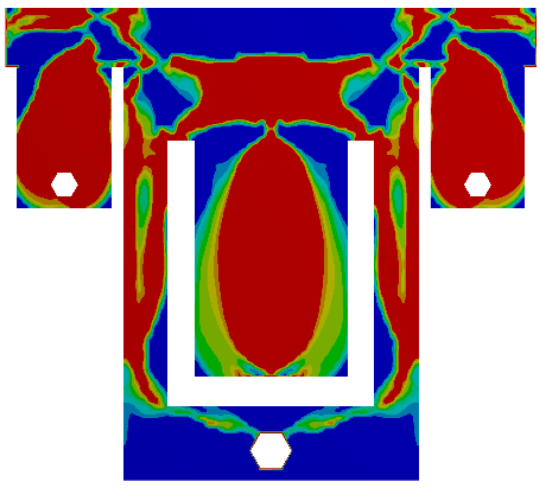

Figure 9.4. Topology optimization results for design domain a with its different thicknesses and input displacements.

(b, Thickness 6mm, Input 1,5mm)

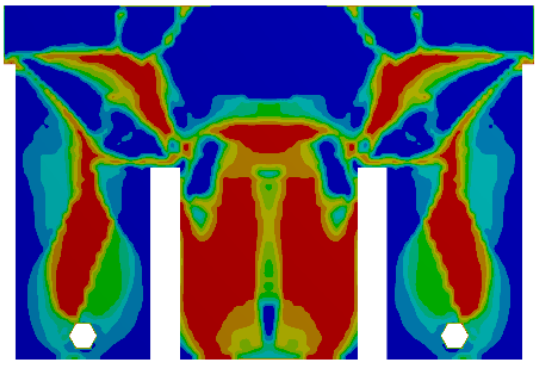

(b, Thickness 3mm, Input 1,5mm)

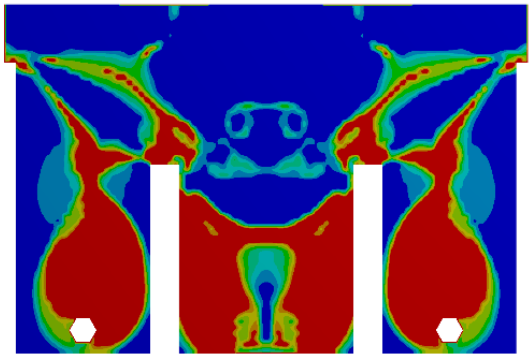

(b, Thickness 6mm, Input 3mm)

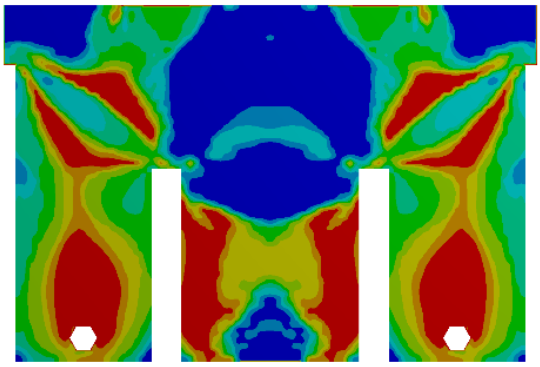

(b, Thickness 3mm, Input 3mm)

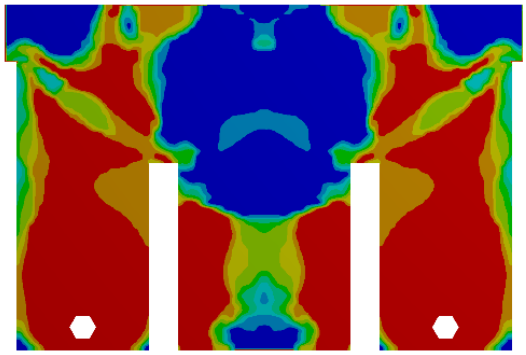

(b, Thickness 6mm, Input 6mm)

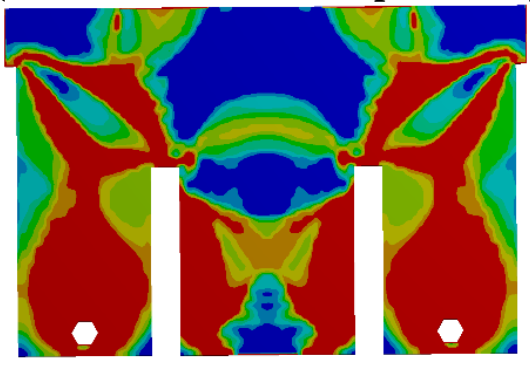

Figure 9.5. Topology optimization results for design domain b with its different thicknesses and input displacements.

(c, Thickness 4mm, Input 3mm) **(c, Thickness 4mm, Input 6mm)**

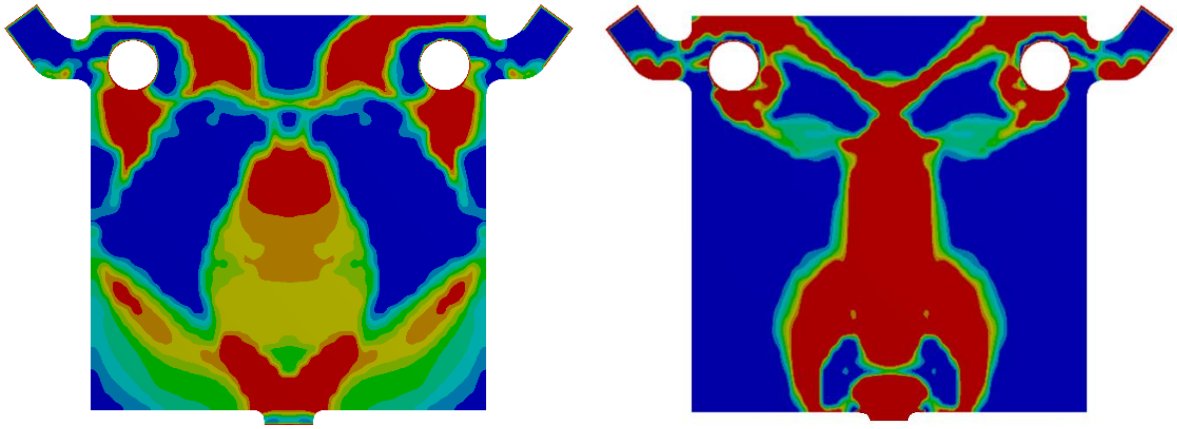

(d1, Thickness 6mm, Input 1,5 mm)

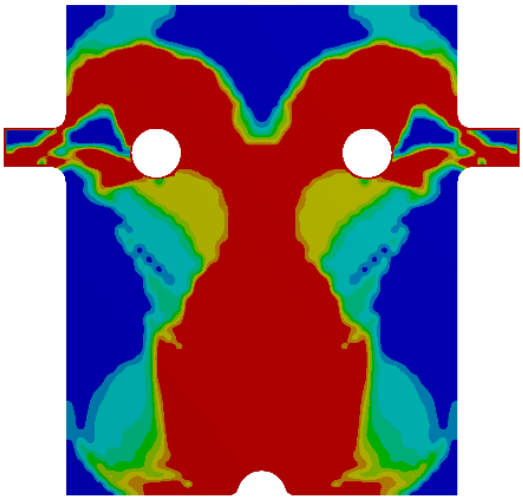

Figure 9.6. Topology optimization results for design domain c with its different thicknesses and input displacements, and for the first optimization step of design domain d1.

From the design domain “c” it also turns out that imposing larger input and output displacements, a topology with more distributed flexible areas is generated, instead of concentrating the deformations on small hinge-like shaped areas, which are undesirable since they lead to high stress concentrations. Considering instead the design domain “d”, the first step of optimization provided the topology displayed in Figure 9.6, which is obtained imposing the displacements and the constraints in Table 9.2.

For this layout in particular, there was applied the multistep optimization approach, in order to examine the capabilities of such method. Indeed, the topology resulting from design domain d1 was remodeled and used to generate another design domain d2, which is represented below in Figure 9.7.

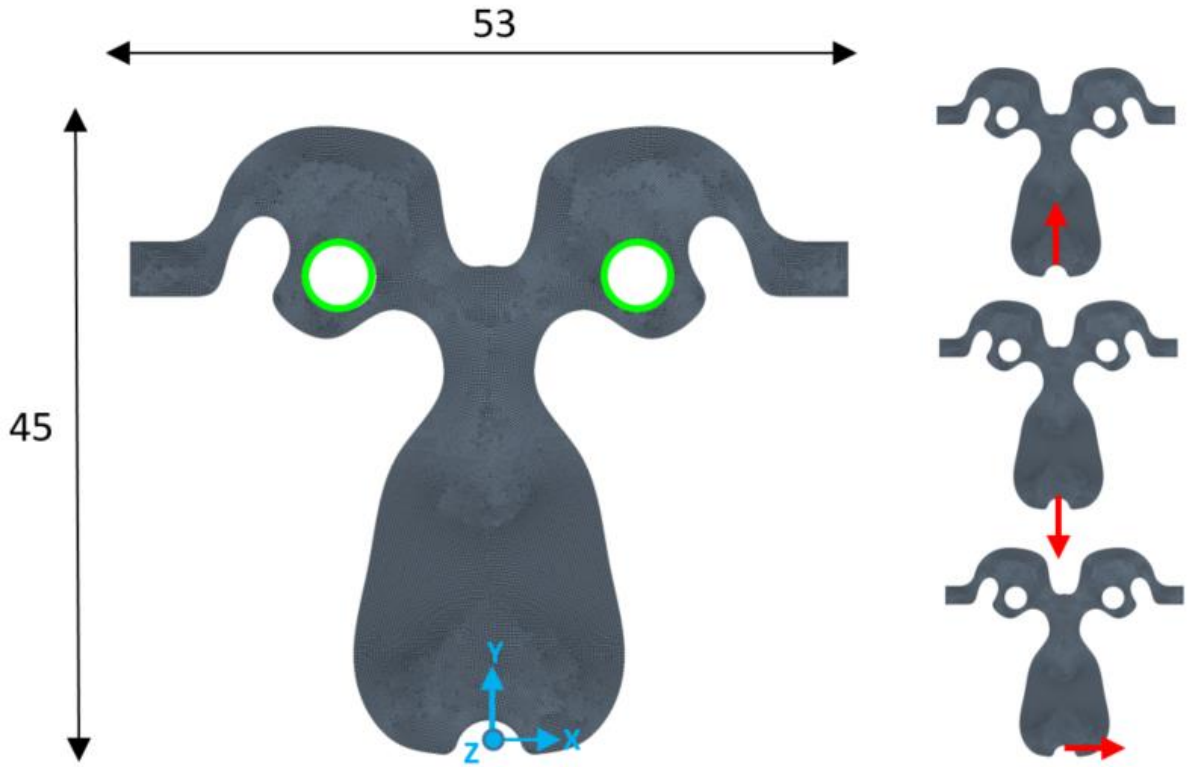

(d2)

Figure 9.7 Meshed model of the design domain d2, with details of the main dimensions in mm

On the right are displayed the three independent FEA load cases carried out as explained before, using the following parameters reported in Table 9.3. As can be observed comparing these values with the displacement values of design domain d1 from table 9.2, only a quarter of the displacements imposed in layout d2 were initially imposed on the first step of TO, consequently conducting a more gradual optimization process, beginning from design domains that become progressively more defined.

Design domain	d2
Thickness [mm]	6
Input displacement [mm]	6
Output displacement constraint [mm] on Y axis, related to Load case A	-12
Output displacement constraint [mm] on Y axis, related to Load case B	12
Output displacement constraint [mm] on X and Y axis, related to Load case C	0

Table 9.3. Overview of the correspondence of displacements imposed, regarding to each load case for design domain d2.

Also for this design domain, after perfoming the non-linear FEA of the load cases specified in Fig.9.7, the topology regions were defined before proceeding with the optimization phase. Hence, the three design domains were defined in a similar way as discussed above, and are represented below in Fig. 9.8. The second optimization phase was therefore carried out using the same admissible stress constraints and manufacturing constraints specified before.

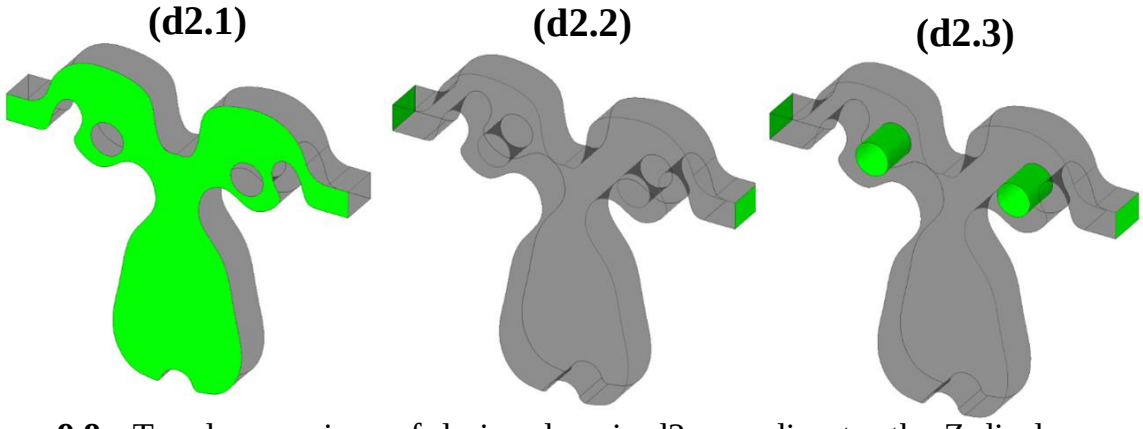

Figure 9.8. Topology regions of design domain d2 regarding to: the Z displacement prevented (left figure), related to the wings' output displacement (central figure), excluded from optimization process (right figure).

(d2, Thickness 6mm, Input 6mm)

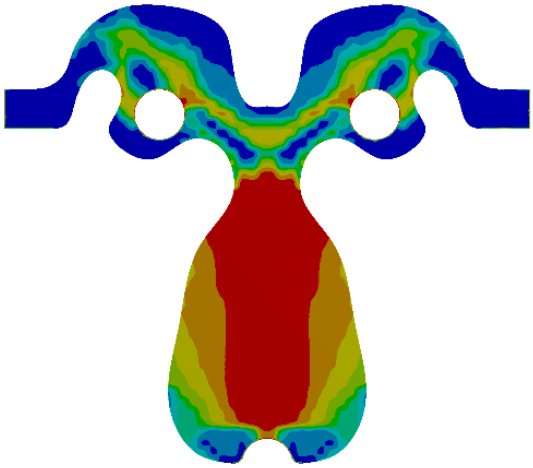

Figure 9.9. Topology optimization result for the second optimization step of design domain d2.

The result of TO for design domain d2 is reported above in Fig.9.9. In comparison with the first topology, in this second geometry it's possible to notice the development of internal features within the regions that previously resulted full of material. This aspect could be attributed to the more detailed definition of the initial design domain but also to the higher amount of displacements imposed within the boundary conditions. Considering the different features of each design domain resulting from TO, four final layouts were remodeled. The geometrical remodeling takes into account both the FDM manufacturing constraint of having a mininum thickness of 1mm in the cross-sections, and it is also aimed to avoid the regions of mechanisms where stress concentration could particularly occurr. Indeed all the contour of the topologies were refined so as to reach general smooth profiles, essential to more evenly distributing the deformations throughout the entire monolithic mechanism. The performances of these four redesigned layouts were then examined thruough non-linear transient FEA, evaluating stress distribution and wing rotation angles.

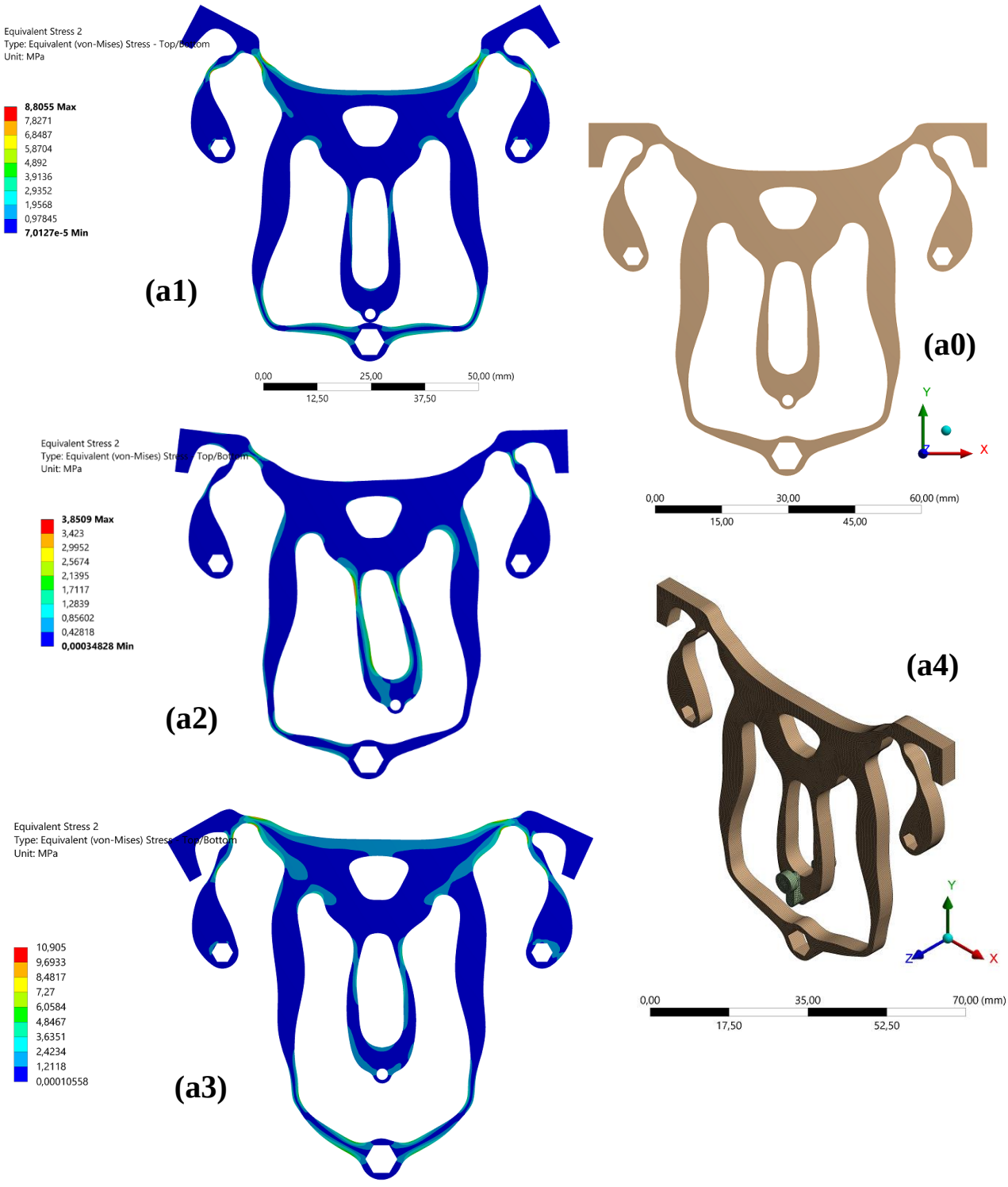

(a, Thickness 4mm, Input 6mm)

Figure 9.10. Layout 1, resulting from the remodeling of TO results for design domain "a": meshed model (a0), wings in upward configuration (a1), central position (a2) downward position (a3) and model with crank and supports (a4)

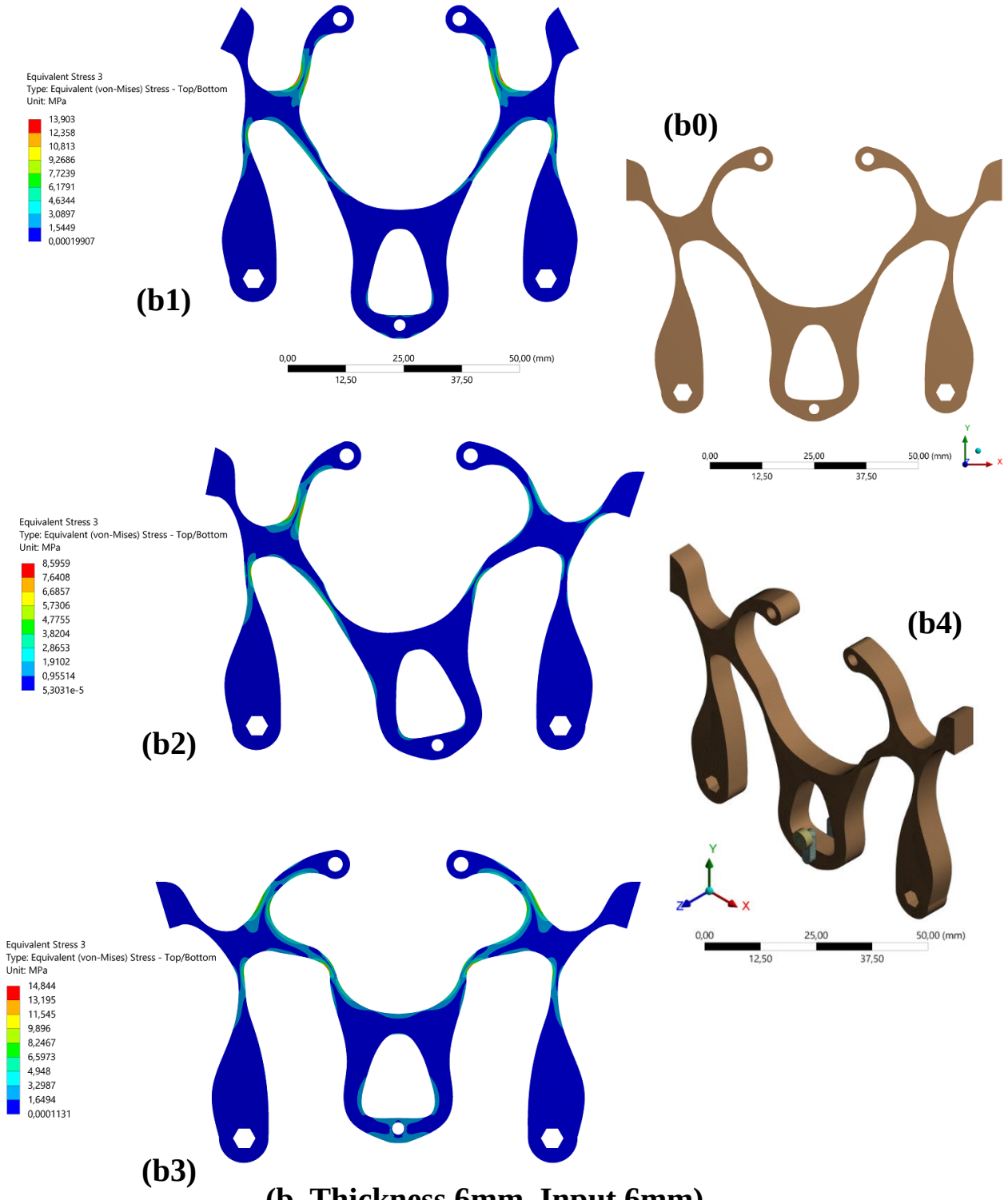

Figure 9.11. Layout 2, resulting from the remodeling of TO results for design domain "b": meshed model (b0), wings in upward configuration (b1), central position (b2) downward position (b3) and model with crank and supports (b4)

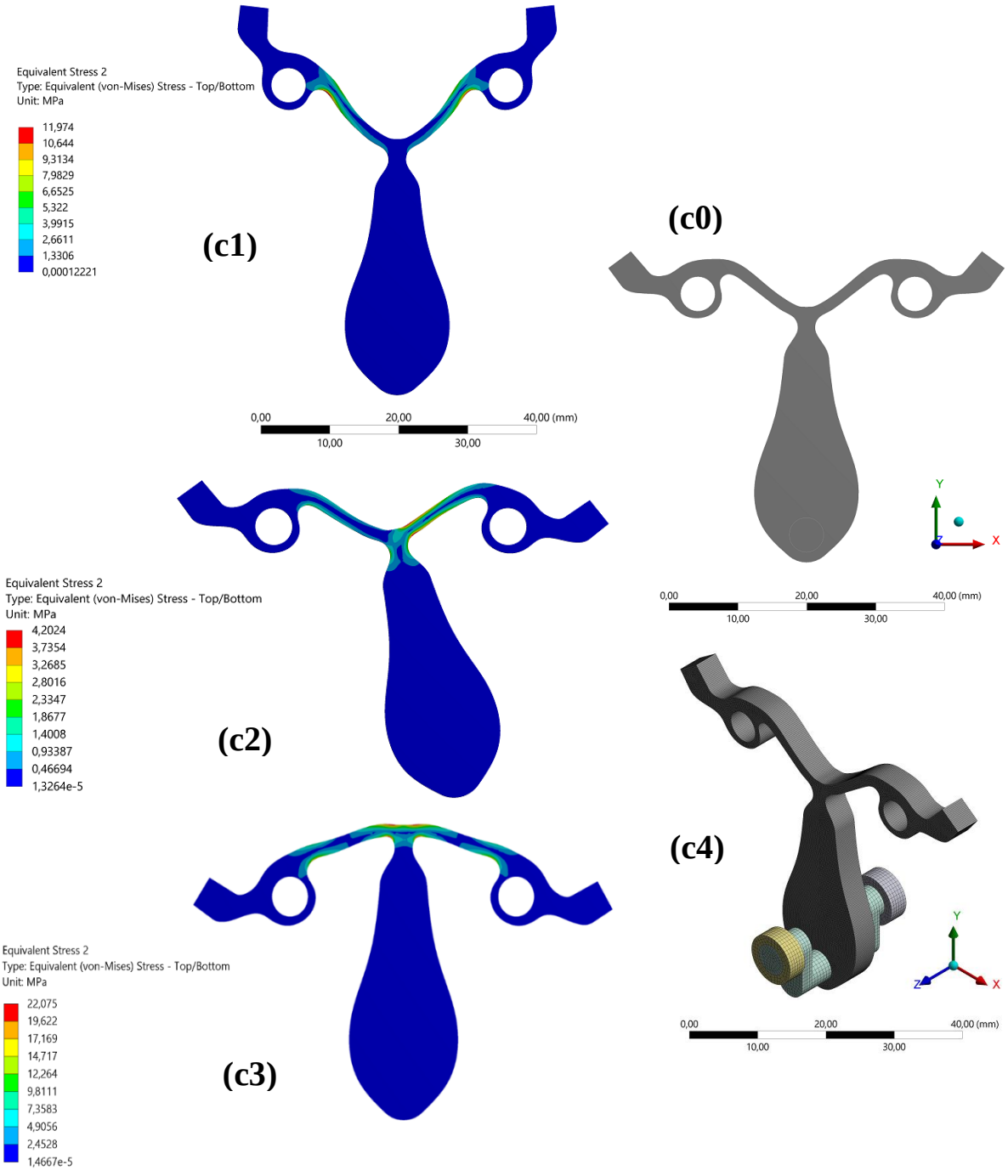

(c, Thickness 4mm, Input 6mm)

Figure 9.12. Layout 3, resulting from the remodeling of TO results for design domain "c": meshed model (c0), wings in upward configuration (c1), central position (c2) downward position (c3) and model with crank and supports (c4)

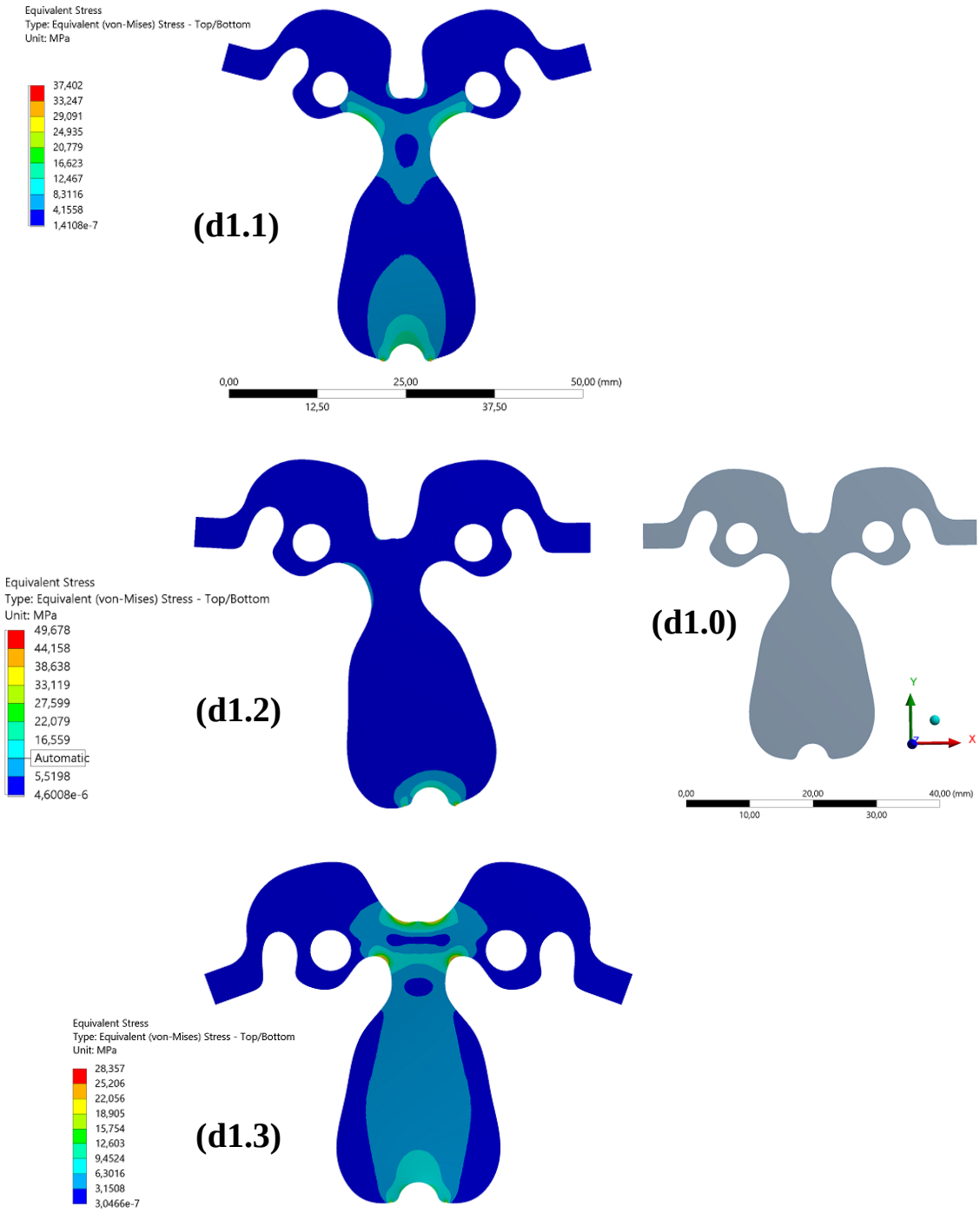

(d1, Thickness 6mm, Input 1.5 mm)

Figure 9.13. Layout d1, resulting from the remodeling of TO results for design domain "d1": meshed model (d1.0), wings in upward configuration (d1.1), central position (d1.2) downward position (d1.3)

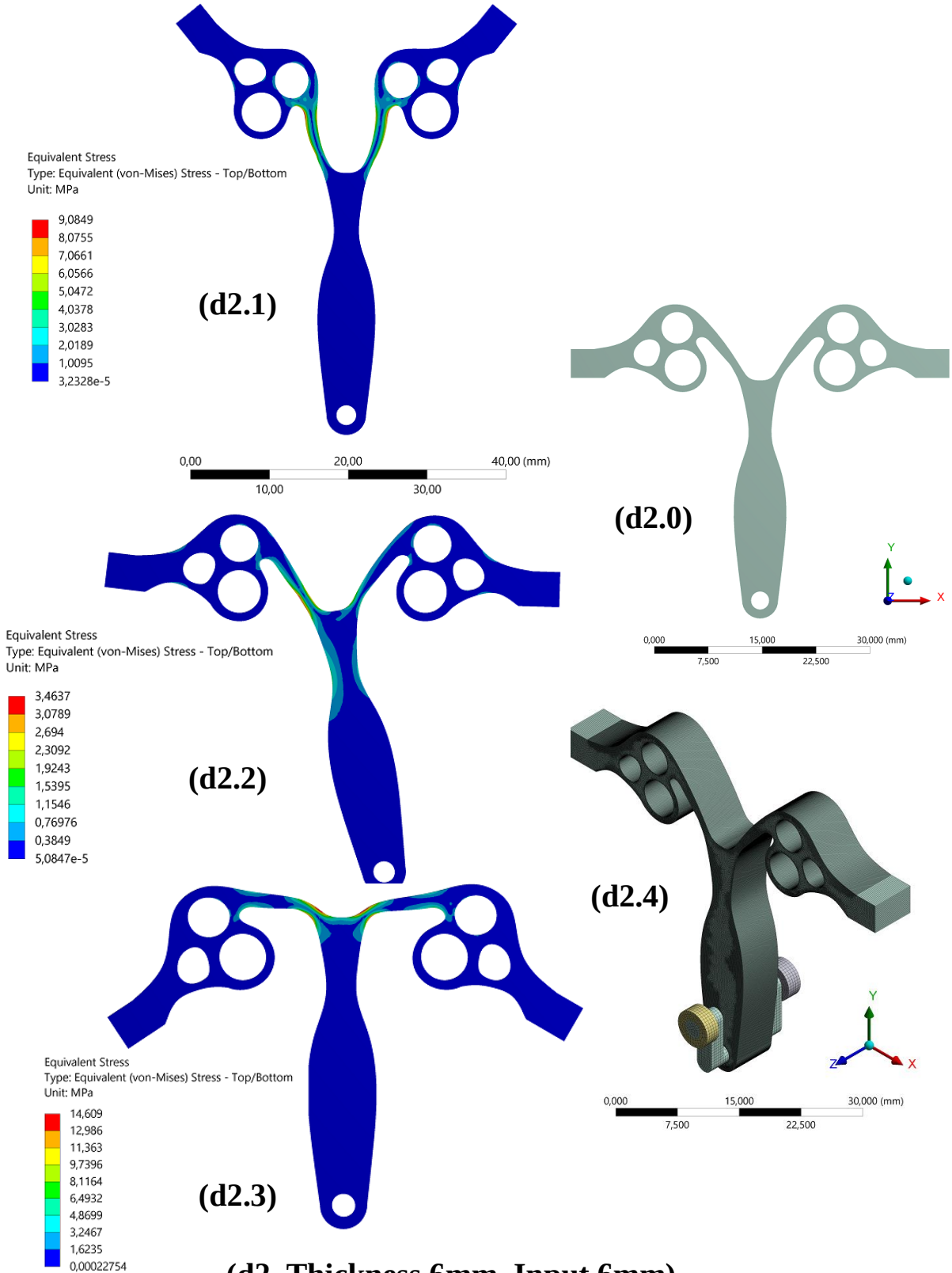

(d2, Thickness 6mm, Input 6mm)

Figure 9.14. Layout d2, resulting from the remodeling of TO results for design domain "d2": meshed model (d2.0), wings in upward configuration (d2.1), central position (d2.2) downward position (d2.3) and model with crank and supports (d2.4)

For the sake of completeness, the FEA results of the intermediate design domain d1 have been also reported in Figure 9.13, although they are not taken into account into the comprehensive comparison of the final remodeled layouts. The geometries of the four redesigned layouts are presented in Fig 9.10, 9.11, 9.12 and 9.13 along with their corresponding stress maps depicting the monolithic CMs in their upstroke, downstroke, and central wing positions. Additionally the meshed model of each layout has been also represented, whose dimensions were determined so as to ensure a minimum of four elements along the thinnest cross-section. Particular attention was paid towards this aspect since the non-linear FEA is addressed to take into account significant displacements at high frequencies, therefore it was necessary to prevent non-convergence issues arising from excessive distortion of elements or high stress concentration points. A table with the minimum dimensions of used elements for each layout is reported below, describing also the total elements exploited for discretizing the models. Aiming to provide a more clear representation of the CMs, above is reported also a perspective view of the geometry comprising the crank attached to the DC motor

CM layout	a	b	c	d1	d2
Minimum dimension of element	0,2	0,25	0,2	0,25	0,2
Total elements in meshed model	53590	49700	45620	51340	44380

Table 9.4. Details on mesh minimum dimension and total amount of elements in each model

Subsequently completing all the transient FEA for the layouts, various outcomes pertaining to stress distribution and wing rotations were derived. In order to facilitate the examination of these FEA results, a comprehensive comparison of the Compliant Mechanisms' performances is presented below in Table 9.5. In particular in the first table are provided details regarding the final CM's weight and its weight reduction, the overall wing rotation angles and the deviations of the angles between the two wings throughout the entire flapping cycle. The second table instead focuses on the stress conditions of the CMs considered in three different configurations of maximum, minimum and central angular position of the wings.

Layout	Weight [g]	Weight reduction %	Overall wing rotation angle [°]	Maximum wings'angle deviation [°]
a	8,26	60,4	63	9,5
b	9,64	70,9	47	22
c	2,47	66,7	72	14
d2	2,51	81,7	86	12

Layout	Maximum Von Mises Stress [MPa]	Stress at maximum rotation angle [MPa]	Stress at minimum rotation angle [MPa]	Stress in central position [MPa]
a	10,9	8,8	10,9	3,8
b	14,8	13,9	14,8	8,6
c	22	11,9	22	4,2
d2	14,6	9	14,6	3,4

Table 9.5. Comparison of the FEA results of the four CMs remodeled layouts.

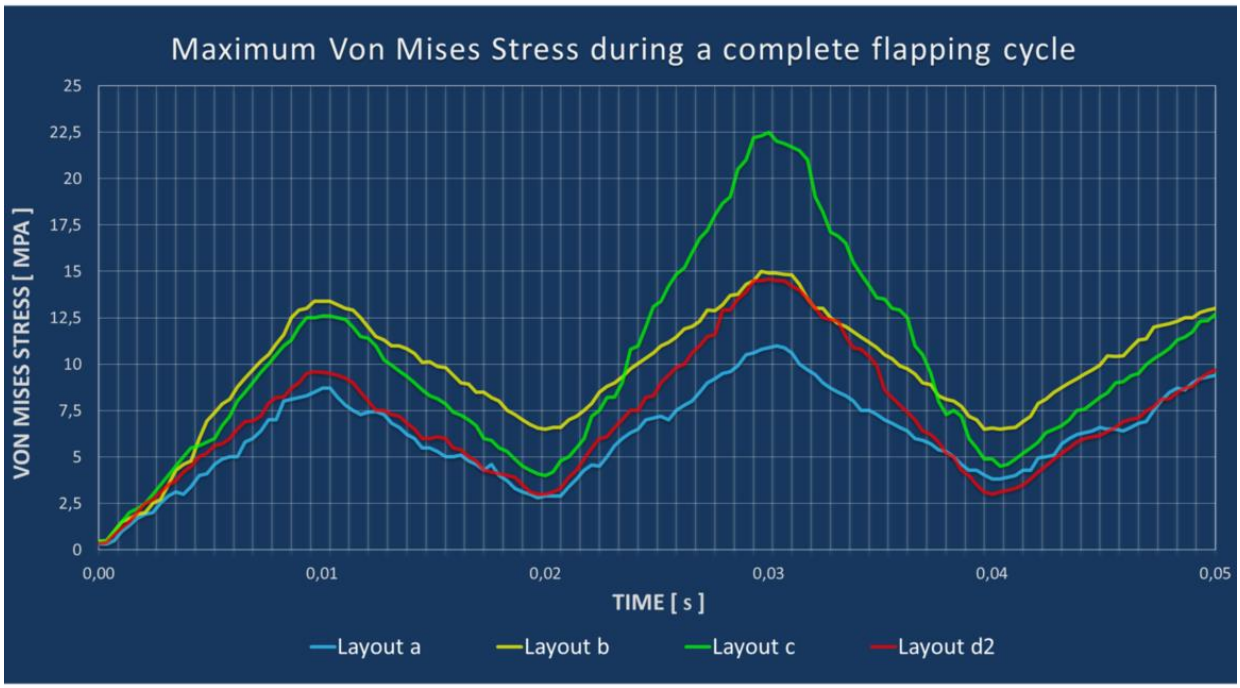

Figure 9.15. Overview of the evolution of Maximum Von Mises stress throughout a complete flapping cycle, compared for the four CMs layouts.

Above in Figure 9.15 is illustrated a graph depicting the stress maximum Von Mises stress trends within the monolithic CMs, showing the variations in stress levels throughout a complete flapping cycle. Similarly as previously observed in chapter 8, the impact of inertial effects coming from the high-frequency displacements is evident across all layouts, noticeable in the distinct wave-like pattern within the stress trends. Particularly, the highest stress peaks manifest near positions where the rotation angle reaches its maximum value. Otherwise, the minimum stresses are observable when the region undergoing input motion (such as the crank connection with the CM) is positioned at the maximum and minimum position along the x-axis. Considering the maximum angular differences of the two wings throughout the flapping cycle, the values are between 9,5° and 22°, resulting to be generally lower than the previous optimized designs. Also in this series of

designs, the objective of decoupling the continuous rotary input motion generated by an electric motor from the alternating symmetrical rotational output movement has been reasonably achieved. Additionally, also a sufficient symmetry in the flapping motion is observed throughout a the flapping cycle, suggesting the feasibility of employing this design approach in conceiving 3D printable monolithic actuation CMs for Fixed-Wing Micro Air Vehicles. Even if this second approach which exploits shell elements broadly shows slightly lower wing rotation angles than previously obtained using solid elements in FEA modeling, it equally represents an effective method suitable to design 3D printable CMs experiencing large deflections at high frequencies. Moreover, compared to the previous FEA modeling, this approach results less time-consuming, also requiring less fewer computational resources. This latter aspect is particularly interesting to be applied for instance during a preliminary design phase, where a larger amount of design variables, design domains and boundary conditions could be therefore taken into account. Furthermore, a significant reduction in weight is obtained, included between 60% and 80% when comparing the weight of the redesigned layouts to their corresponding initial design domains. This percentual reduction results to be higher than the previous solid FEA modeled designs. Especially the multistep optimization approach allows the maximum weight reduction, while maintaining a suitable mechanical behaviour for this kind of CMs' applications. The potentiality of employing shell elements has been assessed, being an advantageous opportunity to facilitate a less computationally intensive design process, opening also chances for analyzing more complex design domains.

10. Conclusions: Outlook and future developments

In this dissertation, the capabilities of a combined design approach involving bio-inspired FWMAV's actuation systems, Compliant Mechanisms, FEA, Topology Optimization and 3D printing technologies have been investigated under various circumstances. Considering the challenging operating conditions to which the monolithic actuation CMs are subjected, a progressively more complex modeling was carried out, so as to provide a comprehensive insight on Compliant Mechanisms behaviour. Beginning from the design of CMs deformed within a small displacement range at low frequencies, the research went through the design of bio-inspired actuation mechanisms for FWMAVs and than focuses on the Topology Optimization design of monolithic compliant actuation mechanisms, exploring different designs and methods. The demanding conditions required to this specific applications arise mainly from these aspects:

- Large deformations required.
- High motion frequencies.
- Need of concentrate a complex motion within a small design domain.
- Complying with material constraints.
- Adhere to manufacturing constraints.
- Transform a continuous input motion into an alternating output motion within the same flexible monolithic mechanism.

Summing up, the following general conclusions can be outlined from the obtained results:

- The study of living organisms' morphology could be a profitable source for conceiving new technological applications or better addressing the redesign of existing products. In particular the living organisms' exploitation of flexibility is suitable to face with an innovative perspective the engineering of flexible structures.
- FDM low-cost additive manufacturing technology can be used for the manufacturing of flexible monolithic CMs applicable as actuation mechanisms for FWMAVs.
- The motion functionalities of flapping insects could be replicated using monolithic CMs actuation systems in FWMAVs. Indeed, comparing with equivalent rigid body actuation mechanisms, less energy waste involving friction, weight, wear and lubrication could be reached using CMs.
- The ability of CMs actuation systems to cyclically store and release energy in form of elastic deformation energy could improve the the flight authonomy of FWMAVs.
- Topology optimization process can be effectively exploited to design CMs actuation systems for FWMAVs. Moreover it allows to explore a wide range of geometric and TO constraints variables, so as to appropriately customize the mechanism to a specific application or operating condition. Geometrical features can be likewise tailored to properly take into account the manufacturing constraints or the supports positioning.

- The maximum angular differences of the two wings throughout the entire flapping cycle reaches a maximum of 28° and a minimum of 9°, therefore is fairly reached the purpose of decoupling the continuous rotary input motion of an electric motor from the alternating symmetrical rotational output movement required to the wings. Indeed, the symmetry of flapping motion has been produced during most of the entire flapping cycle.
- The overall wing rotation angles comprise values between 47° and 106°, representing the suitability of this combined design approach to produce monolithic CMs able to withstand large displacements at high motion frequencies.
- A weight reduction is achievable through TO process, starting from the optimization of a compact design domain with generic geometrical features.
- Stress concentrations could be avoided from the final layouts combining both TO process and an effective geometrical remodeling.
- Compared to the solid element FEA modeling, using shell elements in FEA leads to a less time-consuming design process through Topology Optimization, also requiring less fewer computational resources. This aspect is particularly valuable to be applied during a preliminary design phase, where a larger amount of design variables, design domains and boundary conditions could be therefore taken into account.

- A multistep approach during TO results to be an interesting opportunity especially when it’s desired a more detailed final topology before the geometrical remodeling. It’s also worth to notice its capability of allowing a higher weigth reduction compared with a TO process where displacements are applied all at once.

The results obtained through the combined design approach described in this dissertation allowed to achieve a better insight on the potentialities of CMs and TO for designing actuation mechanisms for FWMAVs. Nevertheless, this research is also intended to suggest the possibility of using such design approach to devise different applications using CMs capable of large displacements at high frequencies. Considering the great variety of design domains and TO constraints applicable, a more accurate analysis could be beneficial in order to assess the influence of the different TO parameters on the final resulting topology. Further explore the potentialities of a multistep TO approach could be also potentially profitable in order to reach geometrically more defined layouts and capable of larger displacements. Moreover, the fatigue stress of flexible 3D printable materials should be further investigated so as to better refine the design process, including also this aspect within the TO. Considering instead the geometrical remodeling phase, exploiting a CM with a parameterized design based on TO results could be advantageous, since a shape optimization process subsequently to the Topology Optimization could be developed, carrying out a more detailed and performing CM actuation system.

References

[1] Ghafarian, M., Shirinzadeh, B., Al-Jodah, A., Das, T. K., Wei, W., Tian, Y., & Zhang, D. (2020). An XYZ micromanipulator for precise positioning applications. *Journal of Micro-Bio Robotics*, *16*(1), 53–63. https://doi.org/10.1007/s12213-020-00124-5

[2] Buzzin, A., Cupo, S., Giovine, E., Cesare, G. de, & Belfiore, N. P. (2020). Compliant nano-pliers as a biomedical tool at the nanoscale: Design, simulation and fabrication. *Micromachines*, *11*(12), 1–13. https://doi.org/10.3390/mi11121087

[3] Wegner, J., Frey, M., Busch, R., & Kleszczynski, S. (2021). Additive manufacturing of a compliant mechanism using Zr-based bulk metallic glass. *Additive Manufacturing Letters*, *1*(October), 100019. https://doi.org/10.1016/j.addlet.2021.100019

[4] Zhu, J., & Hao, G. (2023). Modelling of a general lumped-compliance beam for compliant mechanisms. *International Journal of Mechanical Sciences*, *August*, 108779. https://doi.org/10.1016/j.ijmecsci.2023.108779

[5] Stojiljković, D., Milošević, M., Ristić-Durrant, D., Nikolić, V., Pavlović, N. T., Ćirić, I., & Ivačko, N. (2023). Simulation, Analysis, and Experimentation of the Compliant Finger as a Part of Hand-Compliant Mechanism Development. *Applied Sciences (Switzerland)*, *13*(4). https://doi.org/10.3390/app13042490

[6] Mathew, B. C., Bharatpatil, V., Anilchamoli, Raikwar, M., Negi, M. S., & Singh, H. (2021). Compliant Mechanism and Origami usage in Aerospace and Space Application. *IOP Conference Series: Earth and Environmental Science*, *775*(1). https://doi.org/10.1088/1755-1315/775/1/012008

[7] Fowler, R. M., Maselli, A., Pluimers, P., Magleby, S. P., & Howell, L. L. (2014). Flex-16: A large-displacement monolithic compliant rotational hinge. *Mechanism and Machine Theory*, *82*, 203–217. https://doi.org/10.1016/j.mechmachtheory.2014.08.008

[8] Shan, X., & Birglen, L. (2020). Modeling and analysis of soft robotic fingers using the fin ray effect. *International Journal of Robotics Research*, *39*(14), 1686–1705. https://doi.org/10.1177/0278364920913926

[9] Sun, Y., Zhang, D., Liu, Y., & Lueth, T. C. (2020). FEM-Based Mechanics Modeling of Bio-Inspired Compliant Mechanisms for Medical Applications. *IEEE Transactions*

on Medical Robotics and Bionics, *2*(3), 364–373. https://doi.org/10.1109/TMRB.2020.3011291

[10] Emerson, J., & Elgeneidy, K. (2020). Optimising Soft Fin Ray Robotic Fingers using Finite Element Analysis to Reduce Object Slippage. *UKRAS20 Conference: "Robots into the Real World" Proceedings*, *3*(April), 43–45. https://doi.org/10.31256/dy2bn4p

[11] Dietrich, F., Müller, A., Dietrich, F., Stief, P., Dantan, J., Etienne, A., & Siadat, A. (2020). Design Approach for Heavy-Duty A new methodology to analyze functional physical architecture of existing products for an assembly oriented product family identification. *Procedia CIRP*, *91*, 301–305. https://doi.org/10.1016/j.procir.2020.02.180

[12] Baek, S., Yim, S., Chae, S., Lee, D., & Cho, K. (2020). *Ladybird beetle – inspired compliant origami*. *6262*(April).

[13] Zirbel, S. A., Lang, R. J., Thomson, M. W., Sigel, D. A., Walkemeyer, P. E., Trease, B. P., & Howell, L. L. (2016). *Accommodating Thickness in Origami-Based Deployable*. *135*(November 2013), 1–11. https://doi.org/10.1115/1.4025372

[14] Hu, Y., Zhang, L., Li, W., & Yang, G. (2019). Design and Fabrication of a 3-D Printed Metallic Flexible Joint for Snake-Like Surgical Robot. *IEEE Robotics and Automation Letters*, *4*(2), 1557–1563. https://doi.org/10.1109/LRA.2019.2896475

[15] Sun, Y., Zong, C., Pancheri, F., Chen, T., & Lueth, T. C. (2023). Design of topology optimized compliant legs for bio - inspired quadruped robots. *Scientific Reports*, 1–10. https://doi.org/10.1038/s41598-023-32106-5

[16] Howell, L. L., Magleby, S. P., & Olsen, B. M. (2013.). *Handbook of Compliant Mechanisms*. John Wiley & Sons Ltd, DOI: 10.1002/9781118516485

[17] Wilcox, D. L., & Howell, L. L. (2005). Double-Tensural Bistable Mechanism (DTBM) with on-chip actuation and spring-like post-bistable behavior, *DETC2005-84697*. 1–10.

[18] 18 Lobontiu, N., Compliant Mechanisms Design of Flexures, CRC Press, New York, NY, 2003.

[19] www.all3dp.com

[20] Kiener, L., Saudan, H., Cosandier, F., Perruchoud, G., Ummel, A., & Pejchal, V. (2023). Compliant mechanism based on additive manufacturing. *CEAS Space Journal*, *15*(1), 37–53. https://doi.org/10.1007/s12567-021-00394-0

[21] Zhao, H., & Bi, S. (2010). Stiffness and stress characteristics of the generalized cross-spring pivot. Mechanism and Machine Theory, 45(3), 378–391. https://doi.org/10.1016/j.mechmachtheory.2009.10.001

[22] Lusk, C. P. (2011). Quantifying uncertainty for planar Pseudo-Rigid Body Models. Proceedings of the ASME Design Engineering Technical Conference, 6(PARTS A AND B), 67–73. https://doi.org/10.1115/DETC2011-47456

[23] McCarthy, B., Nail, E., Nagarajan, A., McCullough, J., & Hopkins, J. B. (2023). Design of configuration indifferent compliant building blocks. Precision Engineering, 81(November 2022), 60–67. https://doi.org/10.1016/j.precisioneng.2023.02.002

[24] Shaw, L. A., Sun, F., Portela, C. M., Barranco, R. I., Greer, J. R., & Hopkins, J. B. (2019). Computationally efficient design of directionally compliant metamaterials. Nature Communications, 10(1), 1–13. https://doi.org/10.1038/s41467-018-08049-1

[25] Mattson, C. A., Howell, L. L., & Magleby, S. P. (2004). Development of Commercially Viable Compliant Mechanisms Using the Pseudo-Rigid-Body Model: Case Studies of Parallel Mechanisms. Journal of Intelligent Material Systems and Structures, 15(3), 195–202. https://doi.org/10.1177/1045389X04033256

[26] Gebisa, A. W., & Lemu, H. G. (2017). A case study on topology optimized design for additive manufacturing. IOP Conference Series: Materials Science and Engineering, 276(1). https://doi.org/10.1088/1757-899X/276/1/012026

[27] Wu Q., Yao Z., Wu T., Hou Y., Zhang H., Xu Q., Wang N. Back Frame Section Size Optimization of Large Aperture Telescope, (2023) Journal of Harbin Institute of Technology (New Series), 30 (4), pp. 76 - 84, DOI: 10.11916/j.issn.1005-9113.22012

[28] Yu, Y., Wei, M., Yu, J., Cui, Y., Gao, R., Dong, Z., & Wang, X. (2023). Reliability-based design method for marine structures combining topology, shape, and size optimization. Ocean Engineering, 286(P1), 115490. https://doi.org/10.1016/j.oceaneng.2023.115490

[29] Zhang, X., & Zhu, B. (2018). Topology optimization of compliant mechanisms. In Topology Optimization of Compliant Mechanisms. https://doi.org/10.1007/978-981-13-0432-3

[30] Bendsoe, M.P. and N. Kikuchi, Generating optimal topologies in structural design using a homogenization method. Computer Methods in Applied Mechanics and Engineering, 1988. p. 197–224.

[31] Zhu, B., Zhang, X., Zhang, H., Liang, J., Zang, H., Li, H., & Wang, R. (2020). Design of compliant mechanisms using continuum topology optimization: A review. *Mechanism and Machine Theory*, *143*. https://doi.org/10.1016/j.mechmachtheory.2019.103622

[32] Zhou, M., & Rozvany, G. I. N. (1993). DCOC: An optimality criteria method for large systems Part II: Algorithm. *Structural Optimization*, *6*(4), 250–262. https://doi.org/10.1007/BF01743384

[33] Barthelemy, J. F. M., & Haftka, R. T. (1993). Approximation concepts for optimum structural design - a review. *Structural Optimization*, *5*(3), 129–144. https://doi.org/10.1007/BF01743349

[34] Sigmund, O. (2001). Design of multiphysics actuators using topology optimization - Part II: Two-material structures. *Computer Methods in Applied Mechanics and Engineering*, *190*(49–50), 6605–6627. https://doi.org/10.1016/S0045-7825(01)00252-3

[35] K., S. (1987). The method of moving asymptotes - a new method for structural optimization. *International Journal for Numerical Methods in Engineering.*, *24*(October 1985), 359–373.

[36] Sigmund, O., & Petersson, J. (1998). Numerical instabilities in topology optimization: A survey on procedures dealing with checkerboards, mesh-dependencies and local minima. *Structural Optimization*, *16*(1), 68–75. https://doi.org/10.1007/BF01214002

[37] Sigmund, O. (2007). Morphology-based black and white filters for topology optimization. *Structural and Multidisciplinary Optimization*, *33*(4–5), 401–424. https://doi.org/10.1007/s00158-006-0087-x

[38] Schevenels, M., Lazarov, B. S., & Sigmund, O. (2011). Robust topology optimization accounting for spatially varying manufacturing errors. Computer Methods in Applied Mechanics and Engineering, 200(49–52), 3613–3627. https://doi.org/10.1016/j.cma.2011.08.006

[39] Xie, Y.M., Steven, G.P. (1997). Basic Evolutionary Structural Optimization. In: Evolutionary Structural Optimization. Springer, London. https://doi.org/10.1007/978-1-4471-0985-3_2

[40] Velivela, P. T., & Zhao, Y. F. (2023). Supporting Multifunctional Bio-Inspired Design Concept Generation through Case-Based Expandable Domain Integrated Design (xDID) Model. *Designs*, *7*(4). https://doi.org/10.3390/designs7040086

[41] Ashraf, Y., Rahman, A., Hajibeigy, M. T., & Mahdi, A. S. (2018). Design and Fabrication of Small Vertical-Take- Off-Landing Unmanned Aerial Vehicle. *MATEC Web of Conferences*, *02023*, 1–15.

[42] Serrenho, F. G., Apolinário, J. A., Ramos, A. L. L., & Fernandes, R. P. (2019). Gunshot airborne surveillance with rotary wing UAV-embedded microphone array. *Sensors (Switzerland)*, *19*(19), 1–26. https://doi.org/10.3390/s19194271

[43] Ramasamy, M., Lee, T. E., & Leishman, J. G. (2007). Flowfield of a rotating-wing micro air vehicle. *Journal of Aircraft*, *44*(4), 1236–1244. https://doi.org/10.2514/1.26415

[44] Phan, H. V., & Park, H. C. (2020). Mimicking nature's flyers: a review of insect-inspired flying robots. *Current Opinion in Insect Science*, *42*(Figure 1), 70–75. https://doi.org/10.1016/j.cois.2020.09.008

[45] Phan, H. V., & Park, H. C. (2019). Insect-inspired, tailless, hover-capable flapping-wing robots: Recent progress, challenges, and future directions. *Progress in Aerospace Sciences*, *111*(August), 100573. https://doi.org/10.1016/j.paerosci.2019.100573

[46] Chin, D. D., & Lentink, D. (2016). Flapping wing aerodynamics: From insects to vertebrates. *Journal of Experimental Biology*, *219*(7), 920–932. https://doi.org/10.1242/jeb.042317

[47] Nguyen, Q. V., & Chan, W. L. (2019). Development and flight performance of a biologically-inspired tailless flapping-wing micro air vehicle with wing stroke plane modulation. *Bioinspiration and Biomimetics*, *14*(1). https://doi.org/10.1088/1748-3190/aaefa0

[48] Song, F., Yan, Y., & Sun, J. (2023). Review of insect-inspired wing micro air vehicle. Arthropod Structure and Development, 72, 101225. https://doi.org/10.1016/j.asd.2022.101225

[49] Phan, H. V., & Park, H. C. (2016). Generation of Control Moments in an Insect-like Tailless Flapping-wing Micro Air Vehicle by Changing the Stroke-plane Angle. *Journal of Bionic Engineering*, *13*(3), 449–457. https://doi.org/10.1016/S1672-6529(16)60318-9

[50] Ngo, T. D., Kashani, A., Imbalzano, G., Nguyen, K. T. Q., & Hui, D. (2018). Additive manufacturing (3D printing): A review of materials, methods, applications and challenges. Composites Part B: Engineering, 143(February), 172–196. https://doi.org/10.1016/j.compositesb.2018.02.012

[51] M. Achraf El Youbi, L. Laaouina, A. Jeghal, H. Tairi, M. Zaki, Application of Machine Learning in Fused Deposition Modeling: A Review. Springer Nature Switzerland AG 2023, S. Motahhir and B. Bossoufi (Eds.): ICDTA 2023, LNNS 668, pp. 114–124, 2023. https://doi.org/10.1007/978-3-031-29857-8_12

[52] Cui, M., Shang, E., Jiang, S., Liu, Y., & Zhang, Z. (2021). Design, fabrication and implementation of a high-performance compliant nanopositioner via 3D printing with continuous fiber-reinforced composite. *Journal of Micromechanics and Microengineering*, *31*(12). https://doi.org/10.1088/1361-6439/ac331b

[53] Zolfagharian, A., Lakhi, M., Ranjbar, S., Tadesse, Y., & Bodaghi, M. (2022). 3D printing non-assembly compliant joints for soft robotics. *Results in Engineering*, *15*(August), 100558. https://doi.org/10.1016/j.rineng.2022.100558

[54] Pantano, A., Minore, G., & Carollo, G. (2020). Design of a wiper as compliant mechanisms with a monolithic layout. *SAE International Journal of Passenger Cars - Mechanical Systems*, *13*(3), 173–188. https://doi.org/10.4271/06-13-03-0014

[55] Cadirci, S., Ak, S.E., Selenbas, B., and Gunes, H., "Numerical and Experimental Investigation of Wiper System Performance at High Speeds," Journal of Applied Fluid Mechanics 10:861-870, 2017, https://doi.org/10.18869/acadpub.jafm.73.240.26527.

[56] Bódai, G., and Goda, T.J., "Sliding Friction of Wiper Blade: Measurement, FE Modeling and Mixed Friction Simulation," Tribology International 70:63-74, 2014, https://doi.org/10.1016/j.triboint.2013.07.013.

[57] Zolfagharian, A., Noshadi, A., Zain, M.Z.M., and Bakar, A.R.A., "Practical Multi objective Controller for Preventing Noise and Vibration in an Automobile Wiper System," Swarm Evolution Computing 8:54-68, 2013, https://doi.org/10.1016/j.swevo.2012.08.004.

[58] Nan, Y., Peng, B., Chen, Y., & McGlinchey, D. (2019). From Studying Real Hummingbirds to Designing Hummingbird-Like Robots - A Literature Review. *IEEE Access*, *7*(October), 131785–131804. https://doi.org/10.1109/ACCESS.2019.2939491

[59] Elliston, E. P. P. (2020). Hummingbirds. *Hand-Rearing Birds*, *16*(11), 521–537. https://doi.org/10.1002/9781119167792.ch34

[60] Dickinson, M. H., & Lighton, J. R. B. (1995). Muscle efficiency and elastic storage in the flight motor of Drosophila. *Science*, *268*(5207), 87–90. https://doi.org/10.1126/science.7701346

[61] Bejgerowski, W., Ananthanarayanan, A., Mueller, D., & Gupta, S. K. (2009). Integrated product and process design for a flapping wing drive mechanism. *Journal of Mechanical Design*, *131*(6), 0610061–0610069. https://doi.org/10.1115/1.3116258

[62] Wood, R. J., Avadhanula, S., Sahai, R., Steltz, E., & Fearing, R. S. (2008). Microrobot design using fiber reinforced composites. Journal of Mechanical Design, 130(5), 1–11. https://doi.org/10.1115/1.2885509

[63] www.formfutura.com

[64] Carollo, G., Ingrassia, T., & Pantano, A. (2022). Design of a Low Cost 3D Printable Single-Component Compliant Mechanism for FWMAV's Wing Actuation. *Lecture Notes in Mechanical Engineering*, 39–49. https://doi.org/10.1007/978-3-030-91234-5_4

[65] Pitaru, A. A., Lacombe, J. G., Cooke, M. E., Beckman, L., Steffen, T., Weber, M. H., Martineau, P. A., & Rosenzweig, D. H. (2020). Investigating commercial filaments for 3D printing of stiff and elastic constructs with ligament-like mechanics. Micromachines, 11(9), 1–15. https://doi.org/10.3390/MI11090846

[66] Bendsøe, M. P., & Sigmund, O. (2004). Topology Optimization: Theory, Methods and Applications, Springer Berlin, Heidelberg, https://doi.org/10.1007/978-3-662-05086-6

[67] Carollo, G., Ingrassia, T., Pantano, A., Nigrelli, V., & Tripoli, M. C. (2023). A Topology Optimization Approach to Design of a Low Cost 3D Printable Monolithic Compliant Mechanism for FWMAV's Wing Actuation. *Lecture Notes in Mechanical Engineering*, 652–663. https://doi.org/10.1007/978-3-031-15928-2_57

[68] https://www.astm.org/Standards/ISOASTM52900.htm

[69] A. Kulkarni and C. Saraf, "Learning from Nature: Applications of Biomimicry in Technology," *2019 IEEE Pune Section International Conference (PuneCon)*, Pune, India, 2019, pp. 1-6, doi: 10.1109/PuneCon46936.2019.9105797.

[70] https://www.microphotonics.com/biomimicry-burr-invention-velcro/

[71] https://www.3mitalia.it/3M/it_IT/p/d/b40068905/

[72] https://news.brown.edu/articles/2014/08/sonar

[73] Schnitzler et.al., "From spatial orientation to food acquisition in echolocating bats", *Trends in Ecology &Evolution*, Volume 18, Issue 8, 2003, Pages 386-394, ISSN 0169-5347, https://doi.org/10.1016/S0169-5347(03)00185-X